Control of Electronic and Optical Properties of Two-Dimensional Materials by Functionalization

Inaugural-Dissertation

to obtain the academic degree
Doctor rerum naturalium (Dr. rer. nat.)

submitted to
The Department of Biology, Chemistry, Pharmacy
of Freie Universität Berlin

By
Kangli Wang
from Shandong, China

2022

This work was conducted under the supervision of
Prof. Dr. Beate Paulus (Freie Universität Berlin)
from October 2017 until January 2022

First reviewer:	Prof. Dr. Beate Paulus
Second reviewer:	Dr. Elena Voloshina
Date of defense:	March 10, 2022

I hereby declare that this dissertation was written independently by me. I used no other sources than the ones marked and acknowledged as such. This work has not yet been submitted or published as a dissertation to any other university.

Abstract

Since the exfoliation of graphene in 2005, two-dimensional (2D) materials have become the subject of exploiting interest. In particular, graphene is regarded as a serious alternative to many conventional materials in various applications. The rapid and prosperous development of graphene stimulates numerous research interests on other 2D materials, such as transition metal dichalcogenides (TMDCs). Although the 2D materials have been continuously refreshing and enriching their family, a pure material may not meet the demands for versatile applications. Therefore, this thesis focuses on the modulation of the properties of 2D materials by means of different methods.

In this thesis, three approaches are presented to control the properties of 2D systems involving stacking, covalent functionalization and defect engineering in combination with molecule adsorption. To fully understand the effect of these methods on the 2D materials, we explore the structural, electronic and optical properties of the monolayered graphene and MoS_2 (a traditional representative of TMDCs) by state-of-the-art *ab-initio* computational methods. Specifically, we study (a) the intercalation of surface and subsurface Co-Ir alloy between graphene/Ir(111); (b) the covalent functionalization of 2H-MoS_2, 1T'-MoS_2 and graphene by various chemical groups such as -F, -CH_3, -C_6H_5 and so on; (c) the physisorption and chemisorption of small molecules on the pristine and defective 2H-MoS_2 monolayer. Our results reveal that stacking is an effective method to tune the moiré superstructure and electronic properties of graphene and the interaction strength between graphene and substrate is strongly influenced by the composition and nature of an alloy; covalent functionalization results in dramatic changes to the electronic and optical properties of MoS_2 and graphene, achieving semiconductor-to-metal or metal-to-semiconductor transition; the band gap and optical absorption display a strong dependence on the covalent functionalization coverage, suggesting that the ability to accurately select the coverage of groups attached to the monolayer surfaces, may be an effective way to engineer the optoelectronic properties of graphene and MoS_2 for selected device applications; defects in the MoS_2 are active centers for the molecule adsorption and chemical functionalization; the chemisorption and dissociation of O_2 on the defective surface tend to passivate S defect states, while the physisorption of O_2 and NO molecules on the defective and pristine MoS_2 could enhance the optical absorption peak and the excitonic binding energy.

Our work confirms the tunability of properties of the considered systems and further indicates the possibility of artificially controlling the properties of 2D materials. The deep insights into the functionalized graphene and MoS_2 from this thesis are expected to provide a useful guide for the design of 2D-based devices.

Kurzzusammenfassung

Seit der Exfoliation von Graphen im Jahr 2005 sind zweidimensionale (2D) Materialien Gegenstand von wissenschaftlichem Interesse geworden. Insbesondere Graphen wird in verschiedenen Anwendungen als ernsthafte Alternative zu vielen herkömmlichen Materialien diskutiert. Die schnelle und florierende Entwicklung von Graphen stimuliert das groß Forschungsinteresse an anderen 2D-Materialien, wie z.B. den Übergangsmetalldichalkogeniden (TMDCs). Obwohl die Familie der 2D-Materialien kontinuierlich wächst, erfüllt ein pure Material möglicherweise nicht die Anforderungen für vielseitige Anwendungen. Daher konzentriert sich diese Arbeit auf die Modulation der Eigenschaften von 2D-Materialien mit Hilfe verschiedener Methoden.

In dieser Dissertation werden drei Ansätze vorgestellt um die Eigenschaften von 2D-Systemen zu steuern: Stapelung, kovalente Funktionalisierung und Defekt-Engineering in Kombination mit Moleküladsorption. Um die Auswirkungen dieser Methoden auf die 2D-Materialien vollständig zu verstehen, untersuchen wir die strukturellen, elektronischen und optischen Eigenschaften des einschichtigen Graphens und MoS_2 (eines traditionellen Vertreters von TMDCs) mit modernsten *ab-initio* Berechnungsmethoden. Insbesondere untersuchen wir (a) die Interkalation von Oberflächen- und Suboberflächen von Co-Ir-Legierungen zwischen Graphen/Ir(111); (b) die kovalente Funktionalisierung von 2H-MoS_2, 1T'-MoS_2 und Graphen durch verschiedene chemische Gruppen wie -F, -CH_3, -C_6H_5 und ähnliche; (c) die Physisorption und Chemisorption kleiner Moleküle auf der idealen und defekten 2H-MoS_2-Monoschicht. Unsere Ergebnisse zeigen, dass das Stapeln eine effektive Methode ist, um die Moiré-Überstruktur und die elektronischen Eigenschaften von Graphen abzustimmen, und dass die Wechselwirkungsstärke zwischen Graphen und Substrat stark von der Zusammensetzung und Art einer Legierung beeinflusst wird; kovalente Funktionalisierung führt zu dramatischen Änderungen der elektronischen und optischen Eigenschaften von MoS_2 und Graphen, wodurch ein Halbleiter-zu-Metall- oder Metall-zu-Halbleiter-Übergang erreicht wird; die Bandlücke und die optische Absorption zeigen eine starke Abhängigkeit von dem ausmaß an kovalenter Funktionalisierung; dies deutet darauf hin, dass die Fähigkeit die Konzentration der Funktionalisierung auf den Monoschichtoberflächen genau zu bestimmen ein effektiver Weg sein könnte, um die optoelektronischen Eigenschaften von Graphen und MoS_2 für gezielt Anwendungen zu optimieren; Defekte in MoS_2 sind aktive Zentren für Moleküladsorption und chemische Funktionalisierung; die Chemisorption und Dissoziation von O_2 auf der defekten Oberfläche tendiert dazu, S-Defektzustände zu passivieren, während die Physisorption von O_2 und NO-Molekülen auf dem defekten und idealen MoS_2 den optischen Absorptionspeak und die exzitonische Bindung verstärken können.

Unsere Arbeit bestätigt die Einstellbarkeit der Eigenschaften der betrachteten Systeme und weist ferner auf Möglichkeiten hin die Eigenschaften von 2D-Materialien künstlich zu steuern. Die tiefen Einblicke in funktionalisiertes Graphen und MoS_2 aus dieser Dissertation sollen einen nützlichen Leitfaden für das Design von 2D-Material-basierten Bauelementen darstellen.

List of Publications

Main Publications

[M1] **Influence of surface and subsurface Co–Ir alloy on the electronic properties of graphene.**
K. Wang, T. Vincent, J. Bouhiron, J. B. Bouhiron, S. Pons, D. Roditchev, S. Simon, M. Fonin, B. Paulus, Y. Dedkov, S. Vlaic and E. Voloshina, *Carbon.* **2021**, *183*, 251–258.
DOI: doi.org/10.1016/j.carbon.2021.06.082

[M2] **Electronic and optical properties of fluorinated graphene within many-body Green's function framework.**
K. Wang, J. Shao and B. Paulus, *J. Chem. Phys.* **2021**, *154*, 104705.
DOI: 10.1063/5.0042302

[M3] **Modulating electronic and optical properties of monolayered MoS_2 by covalent mono- and bisfunctionalization.**
K. Wang, M. Kapitzke, L. Green and B. Paulus, *submitted to J. Mater. Chem. C.*

[M4] **Toward a Comprehensive Understanding of Oxygen on MoS_2: From Reaction to Optical Properties.**
K. Wang and B. Paulus, *J. Phys. Chem. C.* **2021**, *125*, 19544–19550.
DOI: 10.1021/acs.jpcc.1c05473

[M5] **Tuning the binding energy of excitons in the MoS_2 monolayer by molecular functionalization and defective engineering.**
K. Wang and B. Paulus, *Phys. Chem. Chem. Phys.* **2020**, *22*, 11936–11942.
DOI: 10.1039/D0CP01239D

Other Publications

[O1] **Quantum Well States for Graphene Spin-Texture Engineering.**
T. Vincent, E. Voloshina, Elena, S. Pons, S. Simon, M. Fonin, K. Wang, B. Paulus, D. Roditchev, Y. Dedkov, and S. Vlaic, *J. Phys. Chem. Lett.* **2020**, *11*, 1594–1600.
DOI: 10.1021/acs.jpclett.0c00069

Contents

1 Introduction

Two-dimensional (2D) materials are atomically thin crystalline solids with very large lateral dimensions as compared to their thickness.[1] The family of these materials contains a wide selection of compositions including most elements of the periodic table.[2, 3] The ongoing revolution of 2D materials begins with experiments on graphene, the first 2D material to be isolated.[4] Its rapid and prosperous development stimulates numerous research interests on other 2D materials, such as hexagonal boron nitride (h-BN), transition metal dichalcogenides (TMDCs), and MXenes.[5–7] Up to now, dozens of 2D material family have been successfully synthesized or exfoliated experimentally.[8] What's more, the low-dimensional materials with a wide range of electronic properties like metals, semimetals, semiconductors, insulators and superconductors, have been a hot topic in recent years.[4, 9–11] Due to their excellent physical and optical properties, 2D materials exhibit great potential for many applications including thermoelectric, electronic and optoelectronic devices.[12–18] The origin of these properties is ascribed to the reduction in the dimensionality (quantum size effect) and consequently, 2D materials have greater advantages and competitiveness in comparison to bulk materials. For example, the large lateral size and atomic thickness endow 2D materials with a high surface-to-volume ratio and full exposure of surface atoms, rendering them ideal for supercapacitors, catalysis and surface-related devices.[19, 20] Different 2D material families are summarized in Figure 1.1(a).

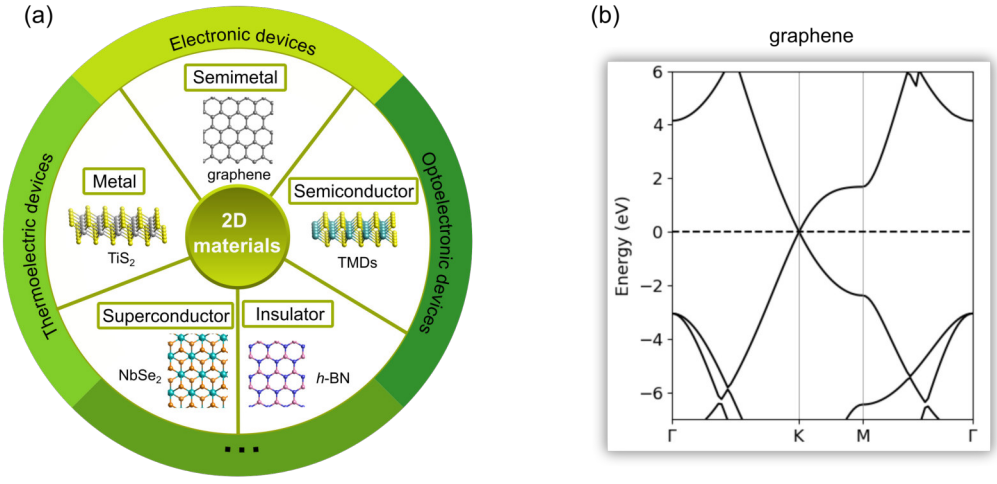

Figure 1.1: (a) A brief summarization of different kinds of typical 2D materials; (b) The band structure of the single-layered graphene calculated with DFT using the PBE exchange-correlation functional.

The study of 2D materials get a booster with the quite easy experimental way in 2005 when the free-standing graphene is isolated from graphite by Geim and his co-workers.[4] Graphene is composed of the arranged sp^2 hybridized atoms in a planar honeycomb network. These sp^2 orbitals hybridized by 2s, $2p_x$ and $2p_y$ form covalent σ bonds with neighbouring carbon atoms with C−C bond length of about 1.42 Å.[21] The remaining p_z orbitals of carbon atoms overlap with each other to construct π orbitals (known as valence bands) and π^* orbitals (known as conduction bands). The conduction and valence bands meet at Dirac point as shown in Figure 1.1(b). The dispersion around the Dirac point is approximately linear, which means that the charge carriers in graphene can be considered as the massless Dirac fermions. As a result, graphene possesses high electrical conductivity and carrier rate.[22] Additionally, graphene also exhibits a high thermal conductivity of 4000 $Wm^{-1}K^{-1}$[23–25], a large specific surface area of 2630 m^2/g,[26] a high Young's modulus of 1.0 TPa[27] and an excellent optical transmittance of 97.7%[28]. The experimental realization of graphene and subsequent exploration of its properties open "the world of graphene", which is worthy of the award of the Nobel Prize for Physics in 2010. Despite the above-mentioned excellent properties of graphene, the lack of inherent band gap limits its use in electronic devices. To address this issue, various methods to functionalize the graphene monolayer have been developed over the past years. More details concerning the functionalization will be discussed later.

In addition to graphene, other 2D materials, like h-BN, TMDCs, and MXenes, have aroused tremendous research interest. 2D h-BN, commonly known as the "white graphene", is a structural analogue of graphene with sublattices being alternately arranged into a honeycomb with equal amounts of boron and nitrogen atoms as seen in Figure 1.1(a). Due to the structural analogy with graphene, h-BN shares similar properties, such as excellent mechanical strength and high thermal conductivity.[5, 29] But unlike graphene, h-BN is an insulator with a wide band gap of 5~6 eV, which is not useful for most electronic applications.[30]

Another important subclass among 2D materials is the family of TMDCs with the chemical formula MX_2, where M is a transition metal and X a chalcogen atom (like MoS_2, $MoSe_2$, WS_2, WSe_2, etc.). Each TMDC monolayer is composed of three atomic layers, in which a transition metal layer is sandwiched between two chalcogen layers. Up to now, 40 different TMDCs with diverse combinations of transition metal and chalcogen atoms have been manufactured.[6] Depending on the coordination between the M and X atoms, two common structural phases of TMDCs are characterized: a trigonal prismatic (2H) phase and an octahedral (1T) phase (Figure 1.2(a)). Normally, the 2H phase is thermodynamically stable with semiconductor properties, whereas the 1T phase is thermodynamically unstable with metallic behavior. Interestingly, experimental studies have demonstrated that each phase can be transformed to the other via the atomic gliding of the layers by experiment.[31] Therefore, the phase transition in TMDCs also attracts widespread attention due to the existence of different electronic properties in the same

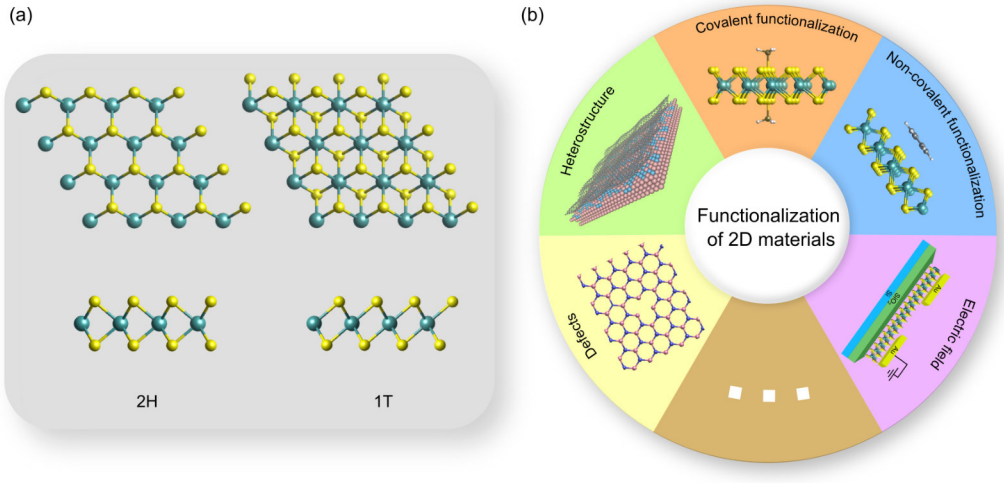

Figure 1.2: (a) The atomic structures of 2H and 1T phases of TMDCs; (b) Schematic representation of different approaches to tailor the properties of 2D materials. The transition metal atoms and chalcogen atoms are in color turquoise and yellow, respectively.

material. In general, bulk TMDCs with a 2H phase possess an indirect band gap, but when the systems are scaled down to monolayers, they exhibit direct electronic band gaps.[32, 33] Such transition in the band gap results in a drastically enhanced photoluminescence (PL).[32, 34] Taking MoS_2 as an example, the freestanding 2H-MoS_2 monolayer shows a strong PL at 1.84 eV, while for bilayer and thicker MoS_2 the PL is quenched.[32, 33] In addition, another interesting feature of 2D-TMDCs is the presence of strongly bound electron-hole pairs (excitons) upon optical excitation. The binding energy of excitons in monolayer TMDCs is relatively large, making them more stable at a relatively high temperature. For example, the binding energy of excitons is determined experimentally to be 0.57 eV for MoS_2,[35] 0.69~0.72 eV for WS_2,[36, 37] 0.37 eV for WSe_2.[38] The large excitonic binding energy is attributed to the reduced dielectric screening in 2D materials, making the effective Coulomb interaction between an electron and a hole much stronger in 2D than that of bulk materials. Furthermore, the excitons in TMDCs are delocalized, known as Wannier-Mott type, and the electron-hole separation extends over several tens of unit cells.[37, 39] The excitons can turn into positive or negative trions by binding an additional electron or hole which are analogous to H^- or H_2^+ respectively.[40] Therefore, the excitons and trions of TMDCs are definitely an interesting question for fundamental physics, and the tunable band gap also makes TMDCs interesting for the replacement of graphene in electronic devices.

To overcome the inherent limitations and further enhance the applicability of 2D materials in diverse fields, a variety of strategies is developed to tune the mechanical, thermal, electronic and optical properties of 2D materials. As displayed in Figure 1.2(b), common approaches such as defect engineering, stacking, covalent functionalization, and non-covalent functionalization, an application of an external electric field, etc. have been

proposed in recent years. These approaches enable not only to tailor the properties of 2D materials but also to impart their novel functionalities. Several effective methods are introduced here to control the properties of 2D materials:

- **Defects.** Owing to the imperfection of the preparation techniques, it is inevitable that the structure of 2D materials always contains abundant defects. According to the dimensions, defects can be mainly divided into two categories: point defects, such as vacancy, antisite, and adatoms; and line defects, such as grain boundaries, and edges.[41, 42] Taking the 2H-MoS_2 as an example, the defects includes monosulfur vacancy, disulfur vacancy, a Mo vacancy with the absence of three sulfur atoms, a Mo vacancy losing all its surrounding sulfur columns, grain boundaries with different angles, and edge reconstruction, which can be characterized by scanning transmission electron microscopy;[43] theoretical work shows that among all structural defects, the monosulfur vacancy is the predominant defect due to its lowest formation energy (~2 eV).[44–46]
  The presence of defects has a great influence on the properties of 2D materials. In thermodynamics, it has been proved that defects can greatly reduce the thermal conductivity of suspended graphene.[47] In mechanics, the strength of graphene can be enhanced or weakened by both the coverage and arrangement of defects, particularly grain boundary.[48, 49] In electronics, the defects will introduce localized states inside the band gap of 2D MoS_2, resulting in hopping transport at room temperature. [50] In addition, the defects may promote the presence of exceptional properties in 2D materials. For example, the defects in 2D materials introduce more active sites to improve the performance of electrocatalyst;[51, 52] chalcogen vacancy in 2D-TMDCs can act as grafting sites for functional groups to create biological and chemical sensors;[53, 54] the substitutional dopants like Mn in TMDCs would couple ferromagnetically via a double-exchange mechanism which induces ferromagnetism while preserving the semiconductor behavior.[55, 56] Importantly, structural defects can be generated intentionally by numerous techniques, such as plasma irradiation, ozone exposure, laser illumination and chemical treatment.[57] This indicates that defect engineering can be achieved by using proper experimental methods.
- **Stacking/Heterostructure arrangement.** A recent noteworthy advance recently in 2D materials is the heterostructure, which consists of at least two different materials. 2D materials can be stacked vertically or stitched laterally to form vertical or lateral heterostructures. Generally, these two types of heterostructures are stabilized by van der Waals (VDW) interaction or covalent bonding of two different 2D materials, respectively. 2D materials behave similarly to flexible films, which are expected to be covered on different structures. Including but not limited to 2D-2D stacked heterostructures, many materials have been used to fabricate heterostruc-

tures, such as 2D-3D heterojunctions with common bulk semiconductors,[58, 59] 0D-2D heterostructure,[60, 61] and 1D-2D heterostructure.[60, 62] Depending on the architecture of the heterostructures, the experimental fabrication methods can be mainly categorized into two approaches: top-down approach, which associated with mechanical transfer process; and bottom-up approach, which is direct growth of 2D materials on other 2D layers, like chemical vapor deposition (CVD).[63, 64] The construction of heterostructures can not only compensate for the disadvantages of the counterpart monolayers, but may also induce new functionality absent in their moieties. The most typical vertical heterostructure is gaphene/h-BN system.[65] Although the atomically thin graphene is predicted to have high electrical conductivity and carrier rate, the carrier mobility of graphene on SiO_2 substrates is limited by the scattering effect from charge impurities, substrate surface roughness and optical phonons of SiO_2.[66–68] h-BN monolayer is an excellent substrate for graphene owing to its atomically smooth surface and nearly free charge trapping. Thus, the carrier mobility of graphene on h-BN substrates is almost one order higher than that on SiO_2 substrates.[65, 69] In addition to graphene/h-BN, the 2D-3D heterostructure of graphene/metal is also widely utilized to control the structural, electronic and magnetic properties of graphene. Moreover, the growth of graphene on metals via CVD is considered as the most promising approach for the preparation of large high-quality graphene film at low cost.[70, 71] From the point of view of electronic structure, the graphene/metal system can be subdivided into two categories: weakly and strongly bonded graphene on the metal. In the case of weakly bonded, graphene is either n- or p-doped and the electronic structure characters of graphene are similar to that of free-standing graphene attributed to the weak VDW interaction between graphene and substrates, examples including graphene/Ir(111),[72] graphene/Cu(111)[73], and graphene/Pt(111)[74] ; concerning the strongly bonded case, the graphene-derived electronic states are significantly modified and the Dirac cone is destroyed due to the strong overlap of the graphene states and valence band states of the underlying metal, examples including graphene/Co(0001)[75], graphene/Ni(111),[76] and graphene/Ru(0001).[77] Another research interest about stacking is focused on TMD. Vertical TMDCs heterostructure presents a powerful platform for band structure and exciton engineering. For instance, in WS_2/MoS_2 heterostructure, the interlayer exciton, transferring from the conduction band maximum of WS_2 to the valence band minimum of the MoS_2 monolayer, can be observed from PL spectra.[78, 79] In practical implementation, the assembly strategy and physical properties of these stacked structures strongly depend on the factors in the stacking process, including the surface quality, angle control, and sample size.

- **Covalent functionalization.** Benefiting from the atomically thin nature of 2D materials, surface engineering provides a promising approach to tune the properties

of 2D materials. Surface engineering could be carried out via the chemisorption and physisorption of the molecule on the 2D materials. In comparison with the physisorption of the molecule on the basal plane, the chemisorption, known as covalent functionalization, has advantages in terms of the robustness of the process and stability of the molecule-2D material interactions. As far as the experiment is concerned, a number of methods of covalent functionalization have been developed. Functionalization of graphene is achieved through: (i) the formation of graphene oxide via the selective oxidation of graphene,[80] which can be further functionalized with various molecules;[81, 82] (ii) directly bonding with reactive intermediates, such as diazonium salts,[83, 84] nitrenes,[85, 86] and carbene-generating diazirines.[87] TMDCs monolayer can be covalently functionalized via (i) repairing the chalcogen vacancy with small organic molecules carrying thiol headgroups;[88–91] (ii) directly reacting with intermediates, such as maleimide derivatives,[92] and diazonium salts.[93, 94]; (iii) phase transition to obtain metallic 1T phase, which is easily functionalized.[95]

By introducing a new guest species onto the 2D materials, covalent functionalization is emerging as a powerful and versatile way to alter the properties of 2D materials. For example, the covalent modification of graphene leads to the transformation of sp^2 hybridized carbons to sp^3 carbons via forming bonds with functional groups, thereby destroying the Dirac cone and opening up a band gap;[96] the functionalized 2H-MoS_2 monolayer using thiolated ligands exhibits highly enhanced antibacterial efficiency and hemocompatibility, highlighting the importance of functionalized TMDCs toward biological applications;[97] the metallic 1T phase of MoS_2, WS_2 and $MoSe_2$ monolayer can be turned into semiconducting phase by the covalent functionalization with organic molecules of iodomethane (HC_3I) or 2-iodoacetamide (C_2H_4INO), leading to strong and tunable PL.[95]

- **Non-covalent functionalization.** Covalent functionalization may largely alter the intrinsic properties of 2D materials. In order to preserve their intrinsic properties, non-covalent functionalization is widely adopted to tune the electronic properties of 2D materials without disrupting crystal structure. Another advantage of non-covalent functionalization is the complete freedom in choosing molecules to physically adsorb on the surface of the 2D material.[53] 2D materials mainly interact with physisorbed molecules through VDW interactions or electrostatic forces, which can be used to controllably adjust the doping level. Generally, planar molecules, such as 3,4,9,10-tetracarboxylic-3,4,9,10-dianhydride (PTCDA),[98, 99] metal phthalocyanine (MPc),[100] and cobalt phthalocyanine (CoPc)[101], have a strong non-covalent interaction with 2D materials. In particular, the planar aromatic molecules can interact efficiently with graphene via π-π interaction, thereby enhancing the adsorbent–adsorbate interaction and forming a stable structure.[98] The non-covalent molecule could produce two types of doping, n-type and p-type,

depending on the electron affinity (EA) or ionization potential (IP) of the molecule. Apart from the gas-phase adsorption, the functionalization from solution also attracts a considerable interest which mainly occurs by self-assembly and introduces highly-ordered monolayers.[99, 101, 102]

The non-covalent interaction between the 2D materials and the physisorbed molecule may improve the performance of the device by combining the excellent properties of the two components. The zero-band gap of graphene can be opened up by the physisorbed aromatic molecules via π-π interaction.[103–105] Moreover, theoretical work shows that the band structure of graphene modified by perylene-3,4,9,10-tetracarboxylic-3,4,9,10-diimide (PTCDI) molecule could be controlled by the molecular configuration, the molecular coverage, and the chemical modification of the active molecules.[104] This also indicates the potential of a tailor-made band gap engineering of graphene by physisorbed molecules. The non-covalent molecular doping changes the properties of TMDCs through two major mechanisms, which are (i) charge transfer and (ii) dipole effects of the dopant molecules.[106] For example, the molecular decoration via self-assembly could control the carrier density and work function with different dipole moments,[107, 108] and modulate the doping level by adjusting the concentration of molecules.[109]

- **Electric field and others.** In addition to the approaches discussed above, other techniques, such as external electric field, strain and alloying are also exploited to modulate the properties of 2D materials. Here we briefly introduce the external electric field and strain effects. A quintessential example of external electric field should be cited that the band gap of the MoS_2 monolayer is non-sensitive to the applied electric field, whereas the band gap of bilayer MoS_2 shows a linear relationship with the gate voltage.[110] Theoretical work shows that as the values of applied electric field increases, the band gap of the TMDCs bilayer decreases, and finally the band gap closes, rendering it metallic.[111] What's more, the external electric field can convert the excitons in TMDCs monolayer into trions.[40, 112] Consequently, the peak corresponding to the exciton decreases with the increase of gate voltages, while that of the trion gradually widens. Accordingly, the use of an external electric field will lead to the realization of electronic and optical properties engineering of 2D materials.

  Strain engineering is a straightforward method to change the properties of 2D materials since it directly affects the lattice structure of materials. 2D materials have stronger deformation capability and can sustain much larger mechanical strain, compared with their bulk counterparts.[113] Diverse methods have been developed to introduce strains to 2D materials, including deforming the substrate, creating wrinkles on the substrate, using pre-patterned substrates, deforming a suspended membrane, and lattice mismatch.[114] As far as the electronic properties are concerned, the application of mechanical deformation gives rise to a reduction

in the band gap of TMDCs, resulting in more electrons thermally excited into the conduction band. Therefore, the electrical conductivity increases with the applied in-plane strain and manifests itself as the piezoresistive effect.[115] As for the optical properties of 2D materials, the enhancement in the PL intensity is observed in the strained region for MoS_2 monolayer.[116] This behavior can be understood in terms of the built-in electric field induced by strain, which leads to the excitons transfer to the strained area and further recombination there. For the thermal properties, tensile strain tends to reduce the thermal conductivity of the graphene monolayer, while multilayer graphene and graphite display the opposite trend.[117]

As aforementioned, there are many approaches to achieve the functionalization of 2D materials. However, there is still a lack of deep theoretical understanding of the effect of functionalization on the electronic structure and optical absorption. For example, the intercalation of alloy in between graphene and substrate, which may bring new properties to graphene, is still largely unexplored (**paper M1**); determining the exact structures of fluorinated graphene in relation with experimental observables (e.g., optical properties) remains a great challenge (**paper M2**); the effect of different functional groups on the properties of MoS_2 is sill unclear (**paper M3**); the atomic configuration of O_2 on the MoS_2 causing the optical enhancement is still controversial (**paper M4**); the combining effect of molecular functionalization (such as NO, $C_3H_3N_3$) and defective engineering on the excitonic properties of MoS_2 is still not well understood (**paper M5**). Therefore, the aim of this thesis is to get a detailed insight into the structural, electronic and optical properties of functionalized graphene and MoS_2 monolayer by *ab-initio* computational methods. It is well known that Density Functional Theory (DFT) has been successful at determining structural properties of 2D materials. However, it is ill-equipped when it comes to predicting the band gap and energy levels of excited states. To solve this problem, the GW approximation is employed in this thesis for accurate calculations of electronic excitations in 2D materials by exploiting exact limits of the screened Coulomb potential. Furthermore, Bethe-Salpeter equation is used to capture the excitonic effect, which could give an accurate prediction of the excitonic state and optical absorption spectrum. Our final goal is to offer insightful guides for improving the performance and the design of 2D-based devices.

The structure of the thesis is summarized the following: in Chapter 2, we present the necessary background knowledge needed to understand the papers of the thesis; Chapter 3 lists the papers, where the reader can find details regarding computational details, structural models, calculated properties as well as discussion of the results; Chapter 4 gives a brief summary and discussion of the results of the thesis as a whole.

2 Theory and Methods

"Give me a fulcrum and a lever and I will move the earth."

-Archimedes

"Give me a professor and a computer and I will finish my Ph.D."

-Kangli Wang

2.1 Hartree-Fock theory

2.1.1 Schrödinger equation

The Schrödinger equation is the foundation of quantum mechanics, which is proposed by Schrödinger in 1926.[118] It is a first-order partial differential equation with respect to time (one particle with position vector $\boldsymbol{r}$):

$$\hat{H}\Phi(\boldsymbol{r},t) = i\hbar\frac{\partial\Phi(\boldsymbol{r},t)}{\partial t}, \tag{2.1}$$

where Φ is the wavefunction and $\hat{H}$ the single-particle Hamiltonian operator which is a function of time:

$$\hat{H} = -\frac{1}{2}\nabla^2 + V(\boldsymbol{r},t), \tag{2.2}$$

where ∇^2 is the Laplace operator of a particle and $V(\boldsymbol{r},t)$ is time-dependent potential. In general, many systems in physics are subjected to time-independent potentials, i.e. $V(\boldsymbol{r},t) = V(\boldsymbol{r})$. Therefore, in the case of a time-independent potential and with the use of the separation of variables, the wavefunction can be written as a product of a function of spatial coordinates $\Psi(\boldsymbol{r})$ and a function of time $\chi(t)$,

$$\Phi(\boldsymbol{r},t) = \Psi(\boldsymbol{r})\chi(t). \tag{2.3}$$

Inserting Eq. (2.3) into Eq. (2.1), we can get

$$i\hbar\frac{1}{\chi(t)}\frac{d\chi(t)}{dt} = \frac{1}{\Psi(\boldsymbol{r})}\left[\frac{1}{2}\nabla^2 + V(\boldsymbol{r})\right]\Psi(\boldsymbol{r}). \tag{2.4}$$

Since the term on the left side of Eq. (2.4) only depends on time and the one on the right side only depends on the variable $\boldsymbol{r}$, these two terms in Eq. (2.4) are equal to a constant,

which we will call E. Consequently, we get the time-independent Schrödinger equation,

$$\hat{H}\Psi(\boldsymbol{r}) = E\Psi(\boldsymbol{r}). \tag{2.5}$$

For a molecule consisting of a certain number N of electrons and a certain number K of nuclei, the non-relativistic Hamiltonian ($\hat{H}_{mol}$) depends on the coordinates of all the electrons and nuclei (in atomic units):

$$\hat{H}_{mol} = \underbrace{-\frac{1}{2}\sum_{i}^{N}\nabla_i^2}_{\hat{T}_e} \underbrace{-\frac{1}{2}\sum_{A}^{K}\nabla_A^2}_{\hat{T}_N} \underbrace{-\sum_{i}^{N}\sum_{A}^{K}\frac{Z_A}{|\boldsymbol{r}_i - \boldsymbol{R}_A|}}_{\hat{V}_{eN}} + \underbrace{\sum_{i}^{N-1}\sum_{j>i}^{N}\frac{1}{|\boldsymbol{r}_i - \boldsymbol{r}_j|}}_{\hat{V}_{ee}} + \underbrace{\sum_{A}^{K-1}\sum_{B>A}^{K}\frac{1}{|\boldsymbol{R}_A - \boldsymbol{R}_B|}}_{\hat{V}_{NN}}, \tag{2.6}$$

where $\boldsymbol{r}$ and $\boldsymbol{R}$ stand for the position vectors; subscripts i/j and A/B refer to the electrons and nuclei, respectively. In Eq. (2.6), the first and second sum denote the kinetic energy operator of electrons ($\hat{T}_e$) and nuclei ($\hat{T}_N$), respectively; the third sum describes the attractive Coulomb interaction between nuclei and electrons ($\hat{V}_{eN}$), which is responsible for the stability of molecules; the last two terms correspond to the electrostatic repulsion between electrons ($\hat{V}_{ee}$) and between nuclei ($\hat{V}_{NN}$), respectively.

For such a molecule containing N-electrons and K-nuclei, the corresponding time-independent Schrödinger equation is a function of $3N$+$3K$ variables. Generally, it is impossible to solve such a problem neither analytically or numerically. To handle this problem, Born and Oppenheimer propose an approximation[119] in 1927, which is based on the large mass difference between electrons and nuclei. Accordingly, the electrons are able to respond instantaneously to any change in the nuclear configuration. In this approximation, it is possible to separate the motion of nuclei and the motion of electrons, leading to a molecular wavefunction in terms of electron position and nuclear position,

$$\Psi(\boldsymbol{r}, \boldsymbol{R}) = \psi_n(\boldsymbol{R})\psi_e(\boldsymbol{r}; \boldsymbol{R}), \tag{2.7}$$

where $\psi_n(\boldsymbol{R})$ and $\psi_e(\boldsymbol{r}; \boldsymbol{R})$ correspond to the nuclear and electron wavefunctions, respectively; $\hat{H}_N$ and $\hat{H}_e$ stand for the Hamiltonian operator of nuclei and electrons, respectively. By means of this ansatz, we can obtain the electronic Schrödinger equation:

$$\hat{H}_e\psi_e(\boldsymbol{r}; \boldsymbol{R}) = (\hat{T}_e + \hat{V}_{eN} + \hat{V}_{ee})\psi_e(\boldsymbol{r}; \boldsymbol{R}) = E_e(\boldsymbol{R})\psi_e(\boldsymbol{r}; \boldsymbol{R}), \tag{2.8}$$

and nuclear Schrödinger equation:

$$\hat{H}_n\psi_n(\boldsymbol{R}) = (\hat{T}_N + \hat{V}_{NN} + E_e(\boldsymbol{R}))\psi_N(\boldsymbol{R}) = E_{tot}\psi_n(\boldsymbol{R}). \tag{2.9}$$

Since the electronic wavefunction contains lots of useful information about the molecular properties, such as electron density, polarizability, dipole moment and so on, the solution

of the electronic Schrödinger equation is the objective of quantum chemistry programs. According to Eq. (2.8) the electronic energy and wavefunction depend parametrically on the nuclear geometry because the electronic Hamiltonian is a function of the position of nuclei $\boldsymbol{R}$. This also indicates that the electronic Schrödinger equation has to be solved for a given nuclear geometry.

2.1.2 Hartree-Fock

As the electronic Schrödinger equation is the main focus of quantum chemistry, we label the electronic wavefunction as $\psi(\boldsymbol{r})$ for simplicity. According to the Pauli principle,[120] the electronic wavefunction needs to satisfy the antisymmetry requirement with respect to the interchange of any set of space-spin coordinates, namely $\psi(\boldsymbol{x}_1, \boldsymbol{x}_2) = -\psi(\boldsymbol{x}_2, \boldsymbol{x}_1)$, because electrons are fermions. Here, the $\boldsymbol{x}$ denotes the complete set of coordinates of one particle comprised of the spatial ($\boldsymbol{r}$) and spin (α or β) parts. To fulfill this requirement, a Slater determinant formed by mutually orthonormal single particle states ($\phi_i(\boldsymbol{x}_m)$) is employed: [121]

$$\psi(\boldsymbol{x}_1, \boldsymbol{x}_2, \ldots, \boldsymbol{x}_N) = \frac{1}{\sqrt{N!}} \begin{vmatrix} \phi_1(\boldsymbol{x}_1) & \phi_2(\boldsymbol{x}_1) & \ldots & \phi_N(\boldsymbol{x}_1) \\ \phi_1(\boldsymbol{x}_1) & \phi_2(\boldsymbol{x}_1) & \ldots & \phi_N(\boldsymbol{x}_1) \\ \vdots & \vdots & & \vdots \\ \phi_1(\boldsymbol{x}_N) & \phi_2(\boldsymbol{x}_N) & \ldots & \phi_N(\boldsymbol{x}_N) \end{vmatrix}, \tag{2.10}$$

where the single particle states $\phi_i(\boldsymbol{x}_m)$ are composed of a spatial orbital $\varphi_i(\boldsymbol{r}_m)$ and one of the two orthonormal spin functions,

$$\phi_i(\boldsymbol{x}_m) = \varphi_i(\boldsymbol{r}_m)\sigma, \qquad \sigma = \alpha \text{ or } \beta. \tag{2.11}$$

The rows of the Slater determinant are numbered by the coordinates of electrons and the columns by the occupied spin orbitals. After considering that the HF wavefunction has the form of a Slater determinant, the energy will be given by the usual quantum mechanical expression (assuming the wavefunction is normalized):

$$E_e = \langle \psi | \hat{H}_e | \psi \rangle. \tag{2.12}$$

Then in Hartree-Fock theory we rewrite the electronic Hamiltonian as

$$\hat{H}_e = \sum_i^N \left(-\frac{1}{2}\nabla_i^2 - \sum_A^K \frac{Z_A}{\boldsymbol{r}_{iA}} \right) + \sum_i^N \sum_{j>i}^N \frac{1}{\boldsymbol{r}_{ij}}, \tag{2.13}$$

$$= \sum_i^N \hat{h}_1(i) + \sum_i^N \sum_{j>i}^N \hat{h}_2(i,j), \tag{2.14}$$

where $\hat{h}_1(i)$ is one-electron operator of the i-th electron and $\hat{h}_2(i,j)$ is two-electron operator involving electron i and j. Combining Eq. (2.12) and Eq. (2.14), the expectation value of the Hamiltonian for the Slater determinant is

$$E_{\mathrm{HF}} = \langle\psi|\hat{H}_e|\psi\rangle = \sum_i^N \left\langle \phi_i \middle| \hat{h}_1 \middle| \phi_i \right\rangle + \frac{1}{2}\sum_{i,j}^N \left[\left\langle \phi_i\phi_j \middle| \hat{h}_2 \middle| \phi_i\phi_j \right\rangle - \left\langle \phi_j\phi_i \middle| \hat{h}_2 \middle| \phi_i\phi_j \right\rangle \right]. \tag{2.15}$$

Next, we apply the variation principle to seek for an optimal set of single particle states that makes $\langle\psi|\hat{H}_e|\psi\rangle$ stationary under arbitrary infinitesimal changes, $\phi_i \longrightarrow \phi_i + \delta\phi_i$. But the variations in $\phi_i(x_m)$ are constrained by the orthonormality requirement, i.e. $\langle\phi_i|\phi_i\rangle - \delta_{ij} = 0$. To accommodate this requirement, the Lagrange multipliers ϵ_{ij} are introduced in this optimization problem. This is a technique in which one minimizes the Lagrange function F

$$\delta F \equiv \delta\left[\langle\psi|\hat{H}_e|\psi\rangle - \sum_{i,j} \epsilon_{ij}(\langle\phi_i|\phi_i\rangle - \delta_{ij}) \right] = 0, \tag{2.16}$$

rather than the energy expectation $\langle\psi|\hat{H}_e|\psi\rangle$ directly. Performing this variation, we can obtain the following one-particle eigenvalue equation:

$$\hat{h}_1\phi_k(\boldsymbol{x}_1) + \sum_i \left[\int \phi_i^*(\boldsymbol{x}_2)\hat{h}_2\phi_i(\boldsymbol{x}_2)\phi_k(\boldsymbol{x}_1)d\boldsymbol{x}_2 - \int \phi_i^*(\boldsymbol{x}_2)\hat{h}_2\phi_i(\boldsymbol{x}_1)\phi_k(\boldsymbol{x}_2)d\boldsymbol{x}_2 \right] = \epsilon_k\phi_k(\boldsymbol{x}_1) \tag{2.17}$$

It is customary to write Eq. (2.17) using the Fock operator $\hat{F}$

$$\hat{F}\phi_k = \epsilon_k\phi_k, \tag{2.18}$$

where

$$\hat{F} = \hat{h}_1 + \sum_i (\hat{J}_i - \hat{K}_i). \tag{2.19}$$

In the above equation, $\hat{J}_i$ is Coulomb operator, describing the classical Coulomb repulsion; $\hat{K}_i$ is the non-classical exchange operator and it is the consequence of the antisymmetry of the wavefunction.

But we have to note that Eq. (2.18) involves the evaluation of the orbitals at every single point in space, which is a rather daunting task for the large system. A significant improvement in the practical solution of the Fock equation is introduced by Roothaan in 1951.[122] In this method, the spatial orbital is expanded in terms of a known basis set

$$\varphi_i(\boldsymbol{r}_1) = \sum_\mu^M C_{\mu i}\chi_\mu(\boldsymbol{r}_1), \tag{2.20}$$

where M is the number of basis functions used; $C_{\mu i}$ is the coefficient of a basis function contributing to the spatial orbital of index i. In most cases, the χ_μ are atomic-like functions, centered about single nuclei in a molecule. Conceptually, this is LCAO, where the molecular orbitals are approximated by a linear combination of atomic orbitals. If the basis set is completed, the above expression will be exact. Having Eq. (2.20) in hand, the Fock equation in Eq. (2.18) becomes:

$$\hat{F}\sum_{\mu}^{K} C_{\mu i}\chi_\mu(\boldsymbol{r}_1) = \epsilon_i \sum_{\mu}^{K} C_{\mu i}\chi_\mu(\boldsymbol{r}_1). \tag{2.21}$$

Then we multiply by $\chi_\nu^*(\boldsymbol{r}_1)$ on the left and integrate to obtain

$$\sum_{\mu} \underbrace{\left[\int d\boldsymbol{r}_1 \chi_\nu^*(\boldsymbol{r}_1)\hat{F}\chi_\mu(\boldsymbol{r}_1)\right]}_{F_{\nu\mu}} C_{\mu i} = \epsilon_i \sum_{\mu} \underbrace{\left[\int d\boldsymbol{r}_1 \chi_\nu^*(\boldsymbol{r}_1)\chi_\mu(\boldsymbol{r}_1)\right]}_{S_{\nu\mu}} C_{\mu i}. \tag{2.22}$$

For simplicity, two definitions of the matrix are introduced: this first one is the Fock matrix $F_{\nu\mu}$ and the second is the overlap matrix $S_{\nu\mu}$. With these definitions, we can get the Roothaan equation:

$$\sum_{\mu} F_{\nu\mu}C_{\mu i} = \epsilon_i \sum_{\mu} S_{\nu\mu}C_{\mu i}, \tag{2.23}$$

or even more simply as matrices

$$\mathbf{FC} = \mathbf{SC}\boldsymbol{\epsilon}. \tag{2.24}$$

Here, the matrix $\boldsymbol{\epsilon}$ is diagonal and contains the orbital energy ϵ_i; $\mathbf{C}$ is a $K \times K$ coefficient matrix whose n-th column denotes the expansion coefficient of φ_i in the basis set χ_μ. Furthermore, the element of the Fock matrix $\mathbf{F}$ themselves depends on the coefficients $C_{\mu i}$. It indicates that the Roothaan equation is nonlinear and can not be solved directly by standard linear techniques. Instead, an iterative approach can be applied in practical calculations. First, a guess of the coefficients, named $\mathbf{C}^0$, is applied to construct a Fock matrix. Upon solving Eq. (2.24), an improved set of coefficient $\mathbf{C}^1$ can be acquired. This new coefficients $\mathbf{C}^1$ are then used in turn to construct an improved Fock matrix, which could be further employed to obtain a second improved set of coefficients $\mathbf{C}^2$. This procedure is repeated until self-consistency is attained to some desired level of accuracy. Such an iterative method is referred to as a self-consistent field (SCF) method.

An advantage of the HF method is that the non-classical exchange interaction is included in an exact manner. Furthermore, the HF method is quite good for representing the shapes of atomic and molecular orbitals and describing the electronic charge distributions. However, the HF wavefunctions are approximate owing to the employment of the single Slater determinant, ignoring the electron-electron correlation. This is an example of mean-field approximation, in which the electrons are described as moving in the average

potential field of all the other electrons. The instantaneous influence of electrons that come close together at some points is not considered. In reality, the electrons try to avoid each other and therefore, their motions are correlated. This implies that the electrons actually are further apart from each other than what the HF orbital describes. Thus, the HF energy is not as low as the exact energy. The energy difference between the exact and HF solution is known as correlation energy:

$$E_{\text{corr}} = E_{\text{exact}} - E_{\text{HF}}. \tag{2.25}$$

To capture the electron-electron correlation neglected in the HF method, many post-HF methods have been proposed, such as Möller-Plesset perturbation theory[123] and configuration interaction method (CI).[124] The Möller-Plesset perturbation theory retreats the HF solution as the starting point and performs perturbation theory in the Coulomb interaction; while the CI method employs a trial wavefunction, which is formed as a linear combination of products of Slater determinants. But there are several serious limitations of these approaches, that is the computational effort grows very rapidly with increasing of the number of electrons and the wavefunctions are complicated objects. Therefore, such post-HF methods are not practical to realistic models of systems, especially for large systems. An alternative to HF calculations used in some cases is density functional theory, which we will discuss in the next section.

2.2 Density functional theory

As we discussed before, the HF method ignores the electron-electron correlation and post-HF methods improve the results over basic HF calculation at the price of much increased computational effort. An alternative approach for treating the many-electrons problem is density functional theory (DFT), which uses the electron density $\rho(\boldsymbol{r})$ as functional variable instead of wavefunctions. Since the density $\rho(\boldsymbol{r})$ is a function of only three spatial coordinates rather than the $4N$ coordinates of the wavefunction, DFT is computationally feasible for large systems. What's more, the applicability of DFT ranges from atoms, molecules to solids.

The foundations of DFT are the Hohenberg-Kohn (HK) theorem and Kohn-Sham (KS) equation.[125, 126] The former provides the basic theoretical foundation for modern DFT and the latter presents a practical way to solve the ground-state electron density by replacing the complicated many-electron problem with an auxiliary non-interacting system. An alternative proof of this theorem (Hohenberg-Kohn theorem I) is provided by Levy, which is simpler and more constructive.[127] Following Levy's approach, we will start with HK theorems which is first put forward to the density variational principle rooted in the wavefunction variational principle.

2.2.1 Hohenberg-Kohn theorem

▶ **Theorem 2.1 (Hohenberg-Kohn theorem I).** The ground-state $\rho_0(\boldsymbol{r})$ of a bound system of interacting electrons determines not only the electron number, but also the external potential $v_{\text{ext}}(\boldsymbol{r})$ and thus the Hamiltonian and all physical properties of the system. ◀

Proof of Theorem 2.1. We assume that there are two different external potentials $v^1_{\text{ext}}(\boldsymbol{r})$ and $v^2_{\text{ext}}(\boldsymbol{r})$, which have the same ground-state density $\rho_0(\boldsymbol{r})$. These two different external potential will result into two different Hamiltonians $\hat{H}_1$ and $\hat{H}_2$ with different ground-state wavefunctions ψ_1 and ψ_2. The ψ_2 is used as test function for the state ψ_1. Then

$$E_1 = \langle \psi_1 | \hat{H}_1 \psi_1 \rangle < \langle \psi_2 | \hat{H}_1 | \psi_2 \rangle, \tag{2.26}$$

where

$$\langle \psi_2 | \hat{H}_1 | \psi_2 \rangle = \langle \psi_2 | \hat{H}_2 | \psi_2 \rangle + \langle \psi_2 | \hat{H}_1 - \hat{H}_2 | \psi_2 \rangle = E_2 + \int dr \left[v^1_{\text{ext}}(r) - v^2_{\text{ext}}(r) \right] \rho_0(r). \tag{2.27}$$

Combining Eq. (2.26) and Eq. (2.27), we can get

$$E_1 < E_2 + \int dr \left[v^1_{\text{ext}}(\boldsymbol{r}) - v^2_{\text{ext}}(\boldsymbol{r}) \right] \rho_0(\boldsymbol{r}). \tag{2.28}$$

Exchanging the labels leads to

$$E_2 < E_1 + \int d\boldsymbol{r}\left[v^2_{\text{ext}}(\boldsymbol{r}) - v^1_{\text{ext}}(\boldsymbol{r})\right]\rho_0(\boldsymbol{r}). \tag{2.29}$$

Addition of Eq. (2.28) and Eq. (2.29) results in the contradiction

$$E_1 + E_2 < E_1 + E_2. \tag{2.30}$$

Therefore, our assumption that the existence of a second potential (which is not equal to $v^1_{\text{ext}}(\boldsymbol{r})$ +constant) that gives the same electron density $\rho_0(\boldsymbol{r})$ must be wrong. The $\rho_0(\boldsymbol{r})$ also determines the number of electrons N

$$N = \int \rho_0(\boldsymbol{r})d\boldsymbol{r}. \tag{2.31}$$

Since $\rho_0(\boldsymbol{r})$ determines both $v_{\text{ext}}(\boldsymbol{r})$ and N, the full Hamiltonian $\hat{H}$ and other observable physical properties of this system can be further determined through the solution of the time-independent or time-dependent Schrödinger equation. ■

▶ **Theorem 2.2 (Hohenberg-Kohn theorem II).** There exists an universal functional of density, $F[\rho]$, such that for N-representable density, the energy functional can be written as

$$E_v[\rho] = F[\rho] + \int dr v_{\text{ext}}(\boldsymbol{r})\rho(\boldsymbol{r}) \geq E_0. \tag{2.32}$$

The equality holds when the density $\rho(\boldsymbol{r})$ is the ground-state density for the external potential $v_{\text{ext}}(\boldsymbol{r})$. ◀

Proof of Theorem 2.2. We define a universal function as

$$F[\rho] = \left\langle \psi^{\min}_\rho \middle| \hat{T}_e + \hat{V}_{ee} \middle| \psi^{\min}_\rho \right\rangle, \tag{2.33}$$

where the minimum is taken over all ψ that give ρ. Then according to the minimum properties of the ground-state, we get

$$E_v[\rho] = \left\langle \psi^{\min}_\rho \middle| \hat{H} \middle| \psi^{\min}_\rho \right\rangle = F[\rho] + \int d\boldsymbol{r} v_{\text{ext}}(\boldsymbol{r})\rho(\boldsymbol{r}) \geq E_0. \tag{2.34}$$

The equality, $\psi^{\min}_\rho = \psi_0$ and $\left\langle \psi_0 \middle| \hat{H} \middle| \psi_0 \right\rangle = E_0$ only holds when the density $\rho(\boldsymbol{r})$ is the ground-state density ρ_0. ■

From the second Hohenberg-Kohn theorem, the ground-state energy and density correspond to the minimum of the energy functional, $E_v[\rho]$. As the density constrains the correct number of electrons, $\int \rho(\boldsymbol{r})d\boldsymbol{r} = N$ (N is fixed), a Lagrange multiplier μ is

introduced in minimizing the energy functional

$$\delta\left[E_v[\rho] - \mu \int d\boldsymbol{r}\rho(\boldsymbol{r})\right] = 0. \tag{2.35}$$

Because

$$\delta\left[E_v[\rho] - \mu \int d\boldsymbol{r}\rho(\boldsymbol{r})\right] = \int d^3\boldsymbol{r}\left[\frac{\delta F[\rho]}{\delta\rho(\boldsymbol{r})} + v_{\text{ext}}(\boldsymbol{r}) - \mu\right]\delta\rho(\boldsymbol{r}), \tag{2.36}$$

we can further get the Euler equation

$$\frac{\delta E_v(\boldsymbol{r})}{\delta\rho(\boldsymbol{r})} = \frac{\delta F[\rho]}{\delta\rho(\boldsymbol{r})} + v_{\text{ext}}(\boldsymbol{r}) = \mu. \tag{2.37}$$

The Lagrange multiplier μ is identified as the chemical potential. According to the second Hohenberg-Kohn theorem, the ground-state density $\rho_0(\boldsymbol{r})$ corresponding to the external potential $v_{\text{ext}}(\boldsymbol{r})$ can be obtained as solution of the Euler equation.

2.2.2 Kohn-Sham equation

As the HK theorem has stated before, all properties of systems are functionals of the density. But the HK theorem does not tell us how to construct the $E_v[\rho]$ or $F[\rho]$. A major breakthrough in DFT is provided by Kohn and Sham.[126] The idea is to introduce an auxiliary system of non-interaction electrons moving in an effective external potential $v_{\text{eff}}(\boldsymbol{r})$ so that the ground-state density is equal to the ground-state density of the fully interacting system. The Hamiltonian of this auxiliary system is simply

$$\hat{H}_{\text{aux}} = \sum_i^N \left[-\frac{1}{2}\nabla_i^2 + v_{\text{eff}}(\boldsymbol{r_i})\right]. \tag{2.38}$$

The auxiliary system is non-interacting. In other words, the corresponding ground-state wavefunction consists of a Slater determinant of single particle states $\phi_i(\boldsymbol{r})$. Thus, they have the form of a single particle Schrödinger-like equation, known as Kohn-Sham equation

$$\left(-\frac{1}{2}\nabla^2 + v_{\text{eff}}\right)\phi_i(\boldsymbol{r}) = \varepsilon_i\phi_i(\boldsymbol{r}). \tag{2.39}$$

Here $\phi_i(\boldsymbol{r})$ are the Kohn-Sham one-electron orbitals and the ground-state density of non-interacting system can be written as

$$\rho(\boldsymbol{r}) = \sum_i^n |\phi_i(\boldsymbol{r})|^2. \tag{2.40}$$

Then we partition the Hohenberg-Kohn functional $F[\rho]$ in the following way

$$F[\rho] = T_s[\rho] + J[\rho] + E_{\text{xc}}, \tag{2.41}$$

1. $T_s[\rho]$ denotes the kinetic energy of non-interacting system,

$$T_s[\rho] = -\frac{1}{2}\sum_i^N \left\langle \phi_i(\boldsymbol{r}) \middle| \nabla^2 \middle| \phi_i(\boldsymbol{r}) \right\rangle. \tag{2.42}$$

   Since the Kohn-Sham kinetic energy is not the true kinetic energy, a correction of the kinetic energy, $(T_{\text{exact}}(\rho) - T_s(\rho))$, is needed to consider.

2. $J[\rho]$ is classical Coulomb repulsion energy, corresponding the second term in Eq. (2.17) and also referred as Hartree energy

$$J[\rho] = \frac{1}{2}\int d\boldsymbol{r}_1 d\boldsymbol{r}_2 \frac{\rho(\boldsymbol{r}_1)\rho(\boldsymbol{r}_2)}{|\boldsymbol{r}_1 - \boldsymbol{r}_2|}. \tag{2.43}$$

3. $E_{\text{xc}}[\rho]$ is the so-called exchange-correlation (xc) energy, which is formally defined by

$$E_{\text{xc}}[\rho] = (T_{\text{exact}}[\rho] - T_s[\rho]) + (V_{ee}[\rho] - J[\rho]). \tag{2.44}$$

   According the above definition, $E_{\text{xc}}[\rho]$ is in fact a sum of the error made in using a non-interacting kinetic energy and the error made in the electron-electron interaction.

It should be noted that such a partition of $F[\rho]$ is quite clever because the first two terms, kinetic energy and Hartree energy, usually contain the largest contribution to the ground-state energy, and the errors in the approximation of E_{xc} can be guaranteed to be relatively small. Finally, the total energy functional of the real system can be written as

$$E[\rho] = T_s[\rho] + J[\rho] + V_{\text{ext}}[\rho] + E_{\text{xc}}[\rho], \tag{2.45}$$

where $V_{\text{ext}}[\rho]$ characterizes the coupling between particles and external potential

$$V_{\text{ext}}[\rho] = \int d\boldsymbol{r} v_{\text{ext}}\rho(\boldsymbol{r}). \tag{2.46}$$

The $E_{\text{xc}}[\rho]$ is not exactly known and further approximations are needed to make. More details about the exchange-correlation energy functional will be discussed in the next section. From the equations and definitions above, we can derive the form of the effective potential v_{eff} from Eq. (2.38)

$$v_{\text{eff}}(\boldsymbol{r}) = v_{\text{ext}}(\boldsymbol{r}) + \int d\boldsymbol{r}_2 \frac{\rho(\boldsymbol{r}_2)}{|\boldsymbol{r}_1 - \boldsymbol{r}_2|} + v_{\text{xc}}[\rho](\boldsymbol{r}), \tag{2.47}$$

where the exchange-correlation potential is defined by

$$v_{\mathrm{xc}}[\rho](\boldsymbol{r}) = \frac{\delta E_{\mathrm{xc}}(\rho)}{\delta \rho(\boldsymbol{r})}. \tag{2.48}$$

2.2.3 Exchange-correlation functional

Based on our previous discussion, the formulation of DFT is exact if we know the exact functional $E_{\mathrm{xc}}[\rho]$, which accounts for the remaining electronic energy not included in the non-interacting kinetic and electronic terms. But this functional is not known and thus for practical calculations, one needs to use an approximation for this quantity. Several approximations at different levels of theory have been developed for $E_{\mathrm{xc}}[\rho]$.
The most simple approximation for $E_{\mathrm{xc}}[\rho]$ is the local density approximation (LDA). It assumes variations of the density to be slow and treats the local density as an uniform electron gas:

$$E_{\mathrm{xc}}^{\mathrm{LDA}}[\rho] = \int d\boldsymbol{r}\rho(\boldsymbol{r})\varepsilon_{\mathrm{xc}}^{\mathrm{unif}}[\rho], \tag{2.49}$$

where $\varepsilon_{\mathrm{xc}}^{\mathrm{unif}}$ is the exchange-correlation energy per electron for the uniform electron gas. In practice, it is common to divide the $E_{\mathrm{xc}}[\rho]$ into groups of exchange and correlation parts:

$$E_{\mathrm{xc}}^{\mathrm{LDA}}[\rho] = E_{\mathrm{x}}^{\mathrm{LDA}}[\rho] + E_{\mathrm{c}}^{\mathrm{LDA}}[\rho]. \tag{2.50}$$

The analytical expression of the exchange energy $E_{\mathrm{x}}^{\mathrm{LDA}}[\rho]$is known exactly.[128] In contrast, the $E_{\mathrm{c}}^{\mathrm{LDA}}[\rho]$ can't be reproduced in analytical form and is usually obtained by fitting to the many-body studies of Gell-Mann and Brueckner and Ceperly and Alder.[129, 130] In principle, LDA approximation is expected to be quite good for systems with (or near) homogeneous density. Although this condition is hardly met by real systems, it turns out that this approximation works better than expected for a wide range of materials. This is due to a cancellation of error between its exchange and correlation pieces. Properties such as lattice parameter, vibrational frequencies and elastic moduli are described reliably for many inhomogeneous systems. Taking the 2H-MoS_2 monolayer as example (see Table 2.1), the lattice constant predicted by LDA is 3.12 Å, which is underestimated only by 1.3% error in comparison with experimental result. But for weakly bonded systems, such as a water dimer, the problem with LDA functional becomes severe.[131] On the other hand, one often needs to deal with spin polarized systems in practice. To solve this problem, local spin density approximation (LSDA) is developed. Its exchange-correlation energy is given by:

$$E_{\mathrm{xc}}^{\mathrm{LSDA}}[\rho] = \int \rho(\boldsymbol{r})\varepsilon_{\mathrm{xc}}^{\mathrm{unif}}[\rho_{\uparrow}(\boldsymbol{r}), \rho_{\downarrow}(\boldsymbol{r})]d\boldsymbol{r} \tag{2.51}$$

where $\rho_{\uparrow}(\boldsymbol{r})$, $\rho_{\downarrow}(\boldsymbol{r})$ are the spin up electron density and spin down electron density, respectively.

In the quest for improved functional, an extension of LDA is proposaed by Perdew and Wang in 1986, called generalized gradient approximation (GGA).[133] In this approximation, the gradient of the electron density is added to LDA (or LSDA) for exchange-correlation energy, which substantially increased the accuracy of description. Therefore, the xc energy is expressed as a functional of electron density and its gradient:

$$E_{\mathrm{xc}}^{\mathrm{GGA}}[\rho] = \int \rho(\boldsymbol{r})\varepsilon_{\mathrm{xc}}^{\mathrm{unif}}(\rho)F_{\mathrm{xc}}[\rho_{\uparrow}(\boldsymbol{r}), \rho_{\downarrow}(\boldsymbol{r}), \nabla\rho_{\uparrow}(\boldsymbol{r}), \nabla\rho_{\downarrow}(\boldsymbol{r})]d\boldsymbol{r}, \tag{2.52}$$

where F_{xc} is the enhancement factor that corrects many errors within LDA for a given $\rho(\boldsymbol{r})$. According to Eq. (2.52), this approximation considers not only the actual value of the electron density, but also its slope at the given position. Therefore, it is often called "semi-local" functional. The choice of F_{xc} makes one GGA differ from another. Within the framework of GGA, the most popular functionals include PBE,[134] PW91[135], Lee-Yang-Parr[136] and Perdew86.[137] For many properties, such as geometries and ground-state energies of molecules and solids, it has been proven that GGA can give a better description than LDA.[138] As displayed in Table 2.1, the lattice constant of monolayered MoS_2 calculated by the PBE functional is 3.18 Å with an error of 0.6%, which is much closer to the experimental value than that of LDA.

To improve the accuracy, further corrections on the exchange-correlation energy functional are considered, such as the inclusion of new inhomogeneity parameters of electron density or the addition of the exact exchange energy. The former is called meta-GGA functional which takes either the Laplace of density ($\nabla^2\rho$)[139, 140] or the kinetic energy density ($\tau = \frac{1}{2}\sum_i^N|\nabla\phi_i(r)|^2$)[141, 142] into account; while the latter, known as hybrid exchange functionals, mixes a fraction of exact exchange from HF with GGA exchange. For example, the PBE0 functional[143, 144]

$$E_{\mathrm{xc}}^{\mathrm{PBE0}} = 0.75E_{\mathrm{x}}^{\mathrm{PBE}} + 0.25E_{\mathrm{x}}^{\mathrm{HF}} + E_{\mathrm{c}}^{\mathrm{PBE}}, \tag{2.53}$$

mixes 75% PBE exchange energy and 25% HF exchange energy with the full PBE correlation energy. We should note that as the accuracy of these functionals increases, the computational cost increases at the same time. Thus, the proper choice of the functional depends on whether the required accuracy can be balanced with the computational efficiency of different methods.

Table 2.1: Equilibrium lattice constant (Å) of the 2H-MoS_2 monolayer calculated by DFT method with different functionals with 500 eV cutoff energy and 24×24 k-points sampling.

	LDA	PBE	revPBE	vdW-DF	vdW-DF2	Exp[132]
lattice constant (Å)	3.12	3.18	3.20	3.25	3.30	3.16

2.2.4 Dispersion correction

The deficiency of conventional DFT functionals discussed above is that they rely on a (semi-)local description of the correlation energy. The long-range dispersion interaction, however, arises from correlated fluctuating motions of electron densities corresponding two distant atoms or molecules.[145] Therefore, the conventional DFT functionals are insufficient to capture such interactions. The dispersion interaction plays a crucial role for many systems such as layered structures and biological systems although it is very weak.

Generally, the dispersion interaction between two atoms or molecules A and B, separated by a distance $\boldsymbol{R}$, can be expressed as[145]

$$E_{\text{disp}}^{\text{AB}}(\boldsymbol{R}) = -\left(\frac{C_6}{\boldsymbol{R}^6} + \frac{C_8}{\boldsymbol{R}^8} + \frac{C_{10}}{\boldsymbol{R}^{10}} \cdots\right). \tag{2.54}$$

The C_n coefficients are the dispersion coefficients where C_6 represents the interaction between two instantaneous dipoles, C_8 describes the interaction between a quadrupole and a dipole and C_{10} includes the interaction between an octopole and a dipole as well as between two quadrupoles. Usually, this expression is truncated after the C_6 term. Accordingly, the most basic method to describe the dispersion interaction is to add a pairwise interaction on top of standard DFT calculation. Grimme et al. proposed to incorporate semiempirical atom pairwise interactions of the form of $-C_6/\boldsymbol{R}^6$, known as dispersion-corrected DFT-Dn (n=1, 2,3).[146–148] In DFT-Dn (n=1, 2), the dispersion energy term has the form

$$E_{\text{disp}} = -S_6 \sum_{A}^{\text{atoms}} \sum_{B>A}^{\text{atoms}} \left(\frac{C_{6,AB}}{\boldsymbol{R}_{AB}^6}\right) f_{\text{damp}}(\boldsymbol{R}_{AB}), \tag{2.55}$$

where S_6 is a scaling parameter and can be used to adjust the correction to the repulsive behavior of the chosen exchange-correction density functional; $C_{6,AB}$ is the dispersion coefficient for the atom pair AB; $\boldsymbol{R}_{AB}$ is the distance between atom A and B; $f_{\text{damp}}(\boldsymbol{R}_{AB})$ is the damping function, which determines the short-range behavior of the dispersion correction and is needed to avoid double-counting effects of electron correction at the intermediate distances

$$f_{\text{damp}}(\boldsymbol{R}_{AB}) = \frac{1}{1 + e^{-d(\boldsymbol{R}_{AB}/\boldsymbol{R}_r - 1)}}, \tag{2.56}$$

where $\boldsymbol{R}_r$ is the sum of atomic vdW radii; d is an adjustable parameter. The total energy is given by

$$E_{\text{tot}} = E_{\text{KS-DFT}} + E_{\text{disp}}. \tag{2.57}$$

The DFT-Dn (n=1, 2) only consider the R^{-6} term; while the DFT-D3 also includes the R^{-8} term in a recursive manner, which is found to improve the description of mid-

range dispersion.[148] It has been proved that DFT-D*n* methods, especially DFT-D3 are accurate and robust for non-covalently bound complexes, even for proteins.[149] The apparent advantage of this method is that everything is calculated only based on Cartesian coordinates and atomic numbers and no information on the atom connectivity is required. But the drawback is the semi-empirical formulation itself.
There is a completely different method, which introduces non-local correlation energy. This is based on the idea of Dion et al. in their vdW-DF.[150, 151] In this scheme, the exchange-correlation energy functional is divided into two pieces,

$$E_{\mathrm{xc}}^{\mathrm{vdW\text{-}DF}}[\rho] = E_{\mathrm{xc}}^{0}[\rho] + E_{\mathrm{c}}^{\mathrm{nl}}[\rho], \tag{2.58}$$

which are treated in different approximations. The first term $E_{\mathrm{xc}}^{0}[\rho]$ includes the semi-local functional, which describe the energetic contribution of short-range exchange and correlation effects. In vdW-DF1, this term is given by the sum of LDA correlation and gradient-corrected exchange given within GGA using the reparametrization of PBE (revPBE).[139] However, since revPBE is generally too repulsive near the equilibrium separation,[152] the PW86 functional[133] is adopted in DFT-DF2. This is because the PW86 gives a good agreement with HF results without spurious exchange binding. Finally, the first term $E_{\mathrm{xc}}^{0}[\rho]$ is given by

$$E_{\mathrm{xc}}^{0}[\rho] = E_{\mathrm{x}}^{\mathrm{GGA}}[\rho] + E_{\mathrm{c}}^{\mathrm{LDA}}[\rho]. \tag{2.59}$$

The second term $E_{\mathrm{c}}^{\mathrm{nl}}[\rho]$ is defined to include the longest ranged or non-local correlation. In both vdW-DF1 and vdW-DF2, the long-range term $E_{\mathrm{c}}^{\mathrm{nl}}[\rho]$ has the simplest form of

$$E_{\mathrm{c}}^{\mathrm{nl}}[\rho] = \int\int \rho(\boldsymbol{r})\phi(\boldsymbol{r},\boldsymbol{r'})\rho(\boldsymbol{r'})d^3\boldsymbol{r}d^3\boldsymbol{r'}. \tag{2.60}$$

The kernel ϕ is given as a function of $R \times f(\boldsymbol{r})$ and $R \times f(\boldsymbol{r'})$, where $R = |\boldsymbol{r} - \boldsymbol{r'}|$ and $f(\boldsymbol{r})$ is a function of $\rho(r)$ and its gradient.[151] To obtain tractable expressions of $E_{\mathrm{c}}^{\mathrm{nl}}[\rho]$ for layered systems, it is necessary to use an additional approximation, as suggested by Lundqvist et al.[153] In this approximation, the nonlocal part of exchange-correlation energy functional has the form of

$$E_{\mathrm{c}}^{\mathrm{nl}}[\rho] = \int_0^\infty \frac{du}{4\pi}\mathrm{Tr}\{S_{\mathrm{xc}}^2 - (\nabla S_{\mathrm{xc}} \cdot \nabla G)^2\} \tag{2.61}$$

where S_{xc} is a symmetric function, describing the plasmon-response; $G = -v/4\pi$ denotes the Coulomb Green function ($v(\boldsymbol{r},\boldsymbol{r'}) = 1/|\boldsymbol{r} - \boldsymbol{r'}|$), u is the imaginary frequency ($\omega = iu$) replacing the time variable . Based on vdW-DF2, vdW-DF-cx is also proposed with reduced gradient to describe the plasmon-response description, where cx stands for consistent exchange.[154] The advantage of vdW-DF-cx is to improve the consistency

between semilocal functional $E_{xc}^{0}[\rho]$ and the plasmon description. It has proven that the vdW-DF-cx functional has excellent performance for solid, layered materials and aromatic molecules.[154]
More accurate approaches beyond the above functional involve the occupied and unoccupied single particle orbitals, such as random phase approximation (RPA),[155] second order screened exchange (SOSEX),[156] and CI that we mentioned in the HF method. These approaches hold a higher accuracy in comparison with standard DFT, but with a high computational cost.

2.2.5 Band gap problem

One of the most important properties of a periodic solid is its fundamental band gap, which provides information about the electronic response of the solid to external influences. It is the smallest energy difference between adding and subtracting one electron from a system, that is the difference of the first ionization potential (E_{IP}) and the first electron affinity (E_{EA}),

$$E_{gap} = E_{IP} - E_{EA} = E(N+1) - 2E(N) + E(N-1). \tag{2.62}$$

But predicting the band gap accurately of a material is still a problem. The first attempt to predict the band gap is by the use of Koopmans' theorem based on the HF theory.[157] Koopmans' theorem states that each eigenvalue of the Fock operator gives the energy required to remove (or add) an electron from (to) the corresponding single-electron state,

$$E_{IP}^{HF} = E_{HF}(N) - E_{HF}(N-1) = \varepsilon_{N}^{HF}, \tag{2.63}$$

$$E_{EA}^{HF} = E_{HF}(N) - E_{HF}(N+1) = \varepsilon_{N+1}^{HF}. \tag{2.64}$$

Koopmans' theorem performs quite well for molecules and has been used for a long time for the calculation of E_{IP} and E_{EA}. But it turns out that it is not a good choice to calculate the band gap of a solid. Firstly, within this theorem it is assumed that the orbitals do not change after ionization, known as the frozen-orbitals approximation, which is a rough approximation. Furthermore, as we discussed before, the HF theory completely neglects electron-electron correlation effect since the wavefunction is approximated by a single Slater determinant. In particular, the electron density of the solid-state is more delocalized compared with molecules, which means that the correlation energy is at the similar magnitude with exchange energy. Consequently, the neglect of correlation in HF will lead to a substantial overestimate of the calculated band gap in semiconductors and insulators. In addition, the HF calculation is considerably expensive computationally for a solid due to the fully nonlocal nature of the exchange operator.
The second attempt is to adopt the DFT method, since it is a formally exact way to determine the ground-state energy and electron density of interacting electrons in an external potential. Similar to Koopmans' theorem, the band gap can be given by the

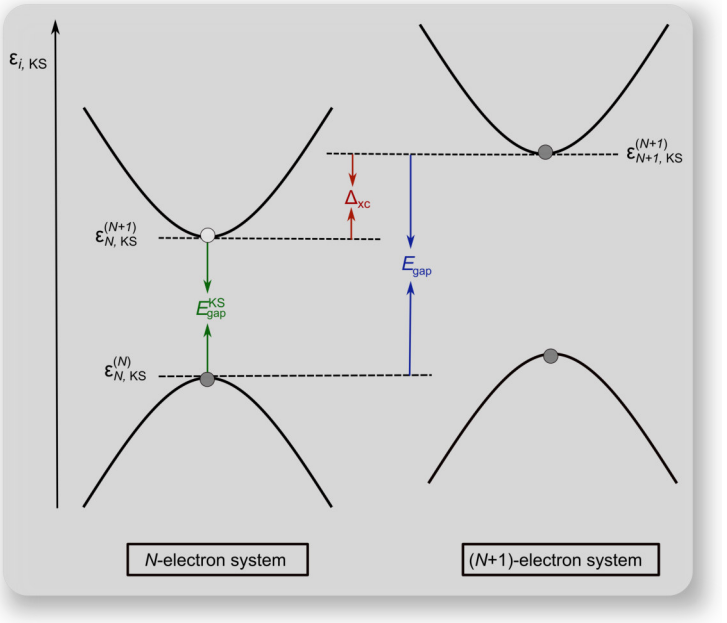

Figure 2.1: Schematic diagram of the DFT band structure of a semiconductor. The exact KS potential jumps up by an additive-constant discontinuty Δ_{xc} when an electron is added to a N-electrons system. The exact band gap is the difference between the two eigenvalues indicated: $E_{gap} = \varepsilon^{(N)}_{N,KS} - \varepsilon^{(N+1)}_{N+1,KS}$.

difference of two KS orbitals:

$$E^{KS}_{gap} = \varepsilon^{(N)}_{N,KS} - \varepsilon^{(N+1)}_{N,KS}, \tag{2.65}$$

where $\varepsilon_{i,KS}$ is the eigenvalue of the i-th KS orbital and N is the total number of electrons with the system. But, it turns out that the use of the $N + 1$ excited state eigenvalue from the KS calculation for an N particle system will lead to an underestimate of the band gap for solid-state systems as shown in Figure 2.1. The exact and KS band gaps are related by

$$E_{gap} = E^{KS}_{gap} + \Delta_{xc}, \tag{2.66}$$

where Δ_{xc} is the derivative discontinuity in xc energy with respect to the particle number.[158–160] This additive-constant discontinuity is the energy associated with a change in the xc potential when an electron is added to an N-electron system. The absence of this discontinuity in the LDA and GGA approximation results in a great underestimate in the prediction of band gap. For example, as indicated in Table 2.2 the calculated band gaps with DFT by PBE functional of the bulk Si, monolayered 2H-MoS_2, 2H-WS_2, h-BN and phosphorene are much smaller than the values observed by experiment. It results in an error of up to 50% for the given systems. Therefore, to obtain an accurate band gap, it is necessary to find a method calculating the derivative discontinuity, such as through

the GLLB-SC functional[161, 162] or using a completely different method, such as the many-body perturbation theory.

Table 2.2: Comparison of the calculated band gaps by DFT, GLLBSC and G_0W_0 methods using the PBE functional to experimental values. The values are given in eV.

	bulk Si	2H-MoS_2	2H-WS_2	h-BN	phosphorene
DFT-PBE	0.58	1.64	1.54	4.64	0.90
GLLB-SC	1.06[163]	2.21[164]	2.16[164]	7.99[165]	1.75[166]
G_0W_0@PBE	1.14	2.54	2.51	7.06	2.03
Exp	1.17[167]	2.50[35]	2.73[36]	6.09[168]	1.50[169]

2.3 Many-body perturbation theory

In the previous section, we discussed that the DFT is ill-equipped to describe the electronic band structure, especially the size of band gap of semiconductors or insulators. A popular way to overcome this limitation of DFT is provided by many-body perturbation theory (MBPT),[170, 171] which not only allows to obtain accurate band structure but also provides access to the excited states. In this section, I will briefly introduce the basic concepts of MBPT and show how to calculate the electronic and optical properties of a solid by the GW method in combination with the BSE on the basis of DFT.
An N-electron state $|\phi_N\rangle$ can be given by the occupancy number of the single-particle states

$$|\phi_N\rangle = |\boldsymbol{r}_1, \boldsymbol{r}_2 ...., \boldsymbol{r}_N\rangle. \tag{2.67}$$

The quantum field operator $\hat{\psi}^\dagger(\boldsymbol{r})$ creates an electron at position $\boldsymbol{r}$,

$$\hat{\psi}^\dagger(\boldsymbol{r})|\boldsymbol{r}_1, ..., \boldsymbol{r}_N\rangle = |\boldsymbol{r}_1, ..., r, ...\boldsymbol{r}_N\rangle, \tag{2.68}$$

and the quantum field operator $\hat{\psi}(\boldsymbol{r})$ annihilates an electron at position $\boldsymbol{r}$,

$$\hat{\psi}(\boldsymbol{r})|\boldsymbol{r}_1, ..., r, ...\boldsymbol{r}_N\rangle = |\boldsymbol{r}_1, ..., \boldsymbol{r}_N\rangle. \tag{2.69}$$

In MBPT, using the quantum field operators the many-body electronic Hamiltonian in Eq. (2.8) can be re-written as

$$\hat{H}_e = \hat{h}_0 + \hat{v}_{ee}. \tag{2.70}$$

Here $\hat{h}_0$ is non-interacting Hamiltonian, which is given by

$$\hat{h}_0 = \int \hat{\psi}^\dagger(\boldsymbol{r}) \left[-\frac{1}{2}\nabla^2 + v_{\text{ext}}(\boldsymbol{r}) \right] \hat{\psi}(\boldsymbol{r}) d\boldsymbol{r}; \tag{2.71}$$

and the electron interaction $\hat{v}_{ee}$ is given by

$$\hat{v}_{ee} = \int \int \frac{\hat{\psi}^\dagger(\boldsymbol{r})\hat{\psi}^\dagger(\boldsymbol{r'})\hat{\psi}(\boldsymbol{r})\hat{\psi}(\boldsymbol{r'})}{|\boldsymbol{r} - \boldsymbol{r'}|} d\boldsymbol{r} d\boldsymbol{r'}. \tag{2.72}$$

This approach not only makes it easy to handle general systems with any number of electrons but also ensures correct particle statistics when developing the perturbation theory.

2.3.1 One-particle Green's function and self-energy

In DFT, the basic variable is the one-body density. Similarly, the building block of MBPT is the one-particle Green's function. One-particle Green's function, also known as a one-particle propagator, is defined as the expectation values of the time-ordered product

of creation and annihilation operators as follows:

$$G(1,2) = -i\left\langle N\middle|\hat{T}\{\hat{\psi}(1)\hat{\psi}^{\dagger}(2)\}\middle|N\right\rangle, \tag{2.73}$$

where $|N\rangle$ is the N-electron ground-state wavefunction; 1 represents a space-time coordinate $(\boldsymbol{r}_1, t_1)$ also subsumes a spin if present; the operators $\hat{\psi}(1)$ and $\hat{\psi}^{\dagger}(2)$ mean to remove and add an electron in space-time positions $(\boldsymbol{r}_1, \mathrm{t}_1)$ and $(\boldsymbol{r}_2, \mathrm{t}_2)$, respectively; $\hat{T}$ is the time-ordering operator:

$$\hat{T}\{\hat{\psi}(1)\hat{\psi}^{\dagger}(2)\} = \begin{cases} \hat{\psi}(1)\hat{\psi}^{\dagger}(2) & \mathrm{t}_1 > t_2, \\ -\hat{\psi}^{\dagger}(2)\hat{\psi}(1) & \mathrm{t}_2 > t_1. \end{cases} \tag{2.74}$$

Since the Green's function in Eq. (2.73) is inconvenient for the actual calculation, two different methods can be employed to proceed. The first method follows from the Heisenberg equation for the field operator,

$$i\frac{\partial\hat{\psi}}{\partial t} = [\hat{\psi}, \hat{H}] = \hat{h}_0(\boldsymbol{r}_1)\hat{\psi}(1) + \int v(12)\hat{\psi}^{\dagger}(2)\hat{\psi}(2)\hat{\psi}(1)d2. \tag{2.75}$$

The second one is to insert a set of complete states and transform them to frequency space by Fourier transformation. Both methods can reach the Lehman representation[172] of the single-particle Green's function,

$$G(\boldsymbol{r}, \boldsymbol{r'}; \omega) = \sum_i \frac{\phi_i^{QP}(\boldsymbol{r})\phi_i^{*QP}(\boldsymbol{r'})}{\omega - \varepsilon_i^{QP} + i\eta \times \mathrm{sgn}(\varepsilon_i^{QP} - \mu)}, \tag{2.76}$$

where μ is the chemical potential, η is a positive real infinitesimal introduced to guarantee the convergence of the Fourier transformation, $\phi_i^{QP}(\boldsymbol{r})$ is the so-called Lehman amplitudes or quasi-particle (QP) wavefunction and ε_i^{QP} is the quasi-particle eigenvalue, which follows

$$\phi_i^{QP}(\boldsymbol{r}) = \begin{cases} \langle N|\hat{\psi}(r)|\phi_i^{N+1}\rangle & \varepsilon_i > \mu, \\ \langle\phi_i^{N-1}|\hat{\psi}(r)|N\rangle & \varepsilon_i < \mu, \end{cases} \tag{2.77}$$

and

$$\varepsilon_i^{QP} = \begin{cases} E_i^{N+1} - E_0 & \varepsilon_i > \mu, \\ E_0 - E_i^{N-1} & \varepsilon_i < \mu. \end{cases} \tag{2.78}$$

Here ϕ_i^{N+1} or ϕ_i^{N-1} denotes the wavefunction of the system in ith state after one electron is removed or added; E_i^N is the total energy of the N-electrons system in its ground-state; E_i^{N+1} and E_i^{N-1} are the total energy of the system in the ith state after removal or addition of an electron. It is worth mentioning that the ε_i^{QP} corresponds to the ionization energy

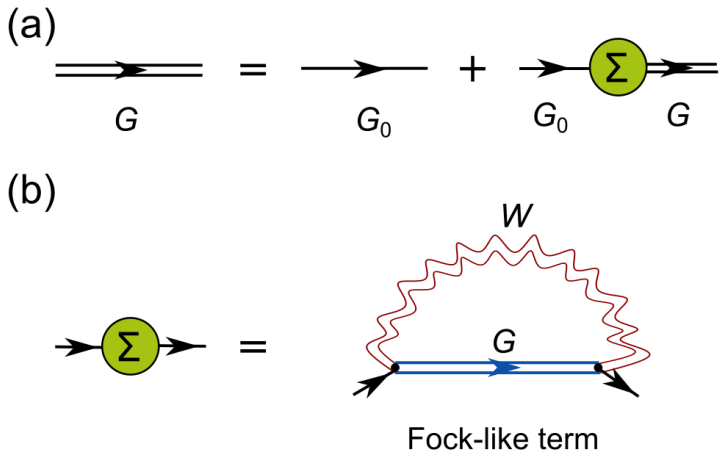

Figure 2.2: (a) Feynman diagrams for the Dyson equation connecting the interacting Green's function G, non-interacting Green's function G_0 and self-energy Σ; (b) In the GW approximation, the self-energy is given by a Fock-like term which is based on the screened Coulomb interaction W.

or electron affinity measured by photoemission or inverse photoemission spectroscopy, which means if the accurate one-particle Green's function is available, the accurate band gap can be obtained.

We introduce a quantity called the self-energy Σ to the equations of motion of Green's function $G(1,2)$

$$\left[i\frac{\partial}{\partial t_1} - \hat{h}_0(\boldsymbol{r}_1)\right]G(1,2) + V_H(1)G(1,2) - \int d3\Sigma(1,3)G(3,2) = \delta(1,2), \tag{2.79}$$

where δ is Dirac's delta function and V_H is the Hartree potential. According to the above equation, the self-energy represents a correction to the single-particle Hamiltonian owing to the inter-particle interaction. Inserting Lehman's representation into Eq. (2.79) yields an integral equation for QP wavefunction and energy, called the quasi-particle equation,

$$\left[\hat{h}_0(\boldsymbol{r}) + V_H(\boldsymbol{r})\right]\phi_i^{QP}(\boldsymbol{r}) + \int d\boldsymbol{r}'\Sigma(\boldsymbol{r},\boldsymbol{r}';\varepsilon_i)\phi_i^{QP}(\boldsymbol{r}) = \varepsilon_i^{QP}\phi_i^{QP}(\boldsymbol{r}). \tag{2.80}$$

The quasiparticle equation is similar to the KS equation. The difference between them is that the self-energy is non-local and non-Hermitian, and is related to energy. We have to note that because the self-energy is non-Hermitian, the eigenvalues ε_i^{QP} may have an imaginary part, suggesting the QP has a finite lifetime.

2.3.2 Hedin's equation and GW approximation

To determine the quasi-particle energy, the interacting Greens' function is needed to be simplified and the self-energy to be determined. As shown in Figure 2.2(a), the first

problem can be solved via the Dyson equation,

$$G(1,2) = G_0(1,2) + \int\int d(3,4)G_0(1,3)\Sigma(3,4)G(4,2), \tag{2.81}$$

where $G_0(1,2)$ is the non interacting particles Green's function that satisfies the Green's function equation of motion with $\Sigma = 0$. Next step we only need to determine the self-energy. For this purpose, Lars Hedin developed a set of coupled equations in 1965.[173] Figure 2.3 describes Hedin's equations which connect the single-particle Green's function G, the self-energy Σ, and the dynamically screened interaction W to the irreducible polarizability P and the vertex function Γ. These equations are

$$\Sigma(1,2) = i\int d(3,4)G(1,4)W(1^+,3)\Gamma(4,2;3); \tag{2.82}$$

$$W(1,2) = v(1,2) + \int d(3,4)v(4,2)P(3,4)W(1,3); \tag{2.83}$$

$$P(1,2) = -i\int d(3,4)G(2,3)G(4,2)\Gamma(3,4;1); \tag{2.84}$$

$$\Gamma(1,2;3) = \delta(1,2)\delta(1,3) + \int d(4,5,6,7)\frac{\delta\Sigma(1,2)}{\delta G(4,5)}G(4,6)G(7,5)\Gamma(6,7;3); \tag{2.85}$$

where 1^+ represents that the time variable is augmented by a positive infinitesimal ($t_1^1 = t_1 + 0^+$). The irreducible polarizability P is defined as the functional derivative of the electronic density with respect to the total potential, e.g. $P(\boldsymbol{r}, t; \boldsymbol{r'}, t') = \delta\rho(\boldsymbol{r}, t)/\delta v_{\text{tot}}(\boldsymbol{r'}, t')$. In Hedin's equation, one important concept is the dynamically screened interaction W. We use Figure 2.4 to explain the difference between the bare interaction v and dynamically screened interaction W: (a) in a vacuum, the electron-electron interaction can be described well by the bared interaction; (b) in the homogenous polarizable medium, two electrons interact with each other by the screened interaction; (c) while in Hedin's equations, the electron-electron interaction is mediated via a virtual electron-hole pair, which leads to dynamic charge redistribution and the electrons seeing other electrons only through a screened interaction. Consequently, the dynamically screened interaction W depends on frequency or a time difference. The corresponding equations are also shown in Figure 2.4.

In principle, when the one-particle Green's function of the interacting system is available, the Dyson equation and Hedin equations form a closed set of equations where the self-energy and interacting Green's function can be determined through an iteration process. But the vertex function Γ, depending on three space-time points, makes it difficult to perform in practical calculations. Hedin introduces a simplification regarding the vertex function, which only takes the zeroth order of the vertex function:

$$\Gamma(1,2;3) = \delta(1,2)\delta(1,3). \tag{2.86}$$

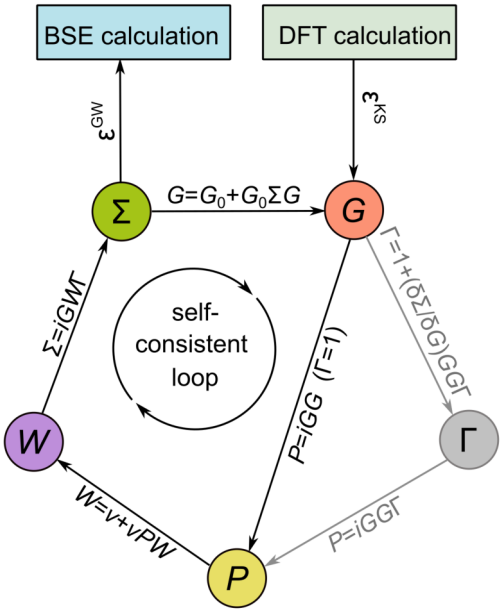

Figure 2.3: Hedin's pentagon.[174] The black paths represent the self-consistent GW process which bypasses the computation of the vertex function Γ. In practise, DFT (or HF) orbitals and their corresponding energies has to be provided as input. As output, GW approximation provides corrected QP states and energies for BSE calculation.

This equation means that the variation of self-energy caused by the polarization of the material is ignored and the resulting approximation is known as random phase approximation (RPA). Applying the RPA in Eq. (2.82), we could obtain a simple form of self-energy,

$$\Sigma = iG(1,2)W(1^+,2). \tag{2.87}$$

This equation states that the self-energy is the product of only the Green's function G and the screened Coulomb interaction W, also known as GW approximation. It turns out that the self-energy is the Hartree term plus a Fock-like term, as shown in Figure 2.2(b). The irreducible polarizability P is also simplified to

$$P(1,2) = -iG(1,2)G(2,1). \tag{2.88}$$

As shown in Figure 2.3, Hedin's equations can be solved in an iterative cycle, just as the case of the KS equation as we talked about previously. This cycle needs to be initialized from a first guess Green's function G_0. But in practice, this is a expensive computational task, and thus a further approximation is often made. Generally, we use the Kohn-Sham (or HF) wavefunction as a trial wavefunction and the corresponding expectation value of Eq. (2.80) is

$$\varepsilon_i^{\mathrm{QP}} = \varepsilon_i^{\mathrm{KS}} - \langle \phi_i^{\mathrm{KS}} | v_{xc}(r) | \phi_i^{\mathrm{KS}} \rangle + \langle \phi_i^{\mathrm{KS}} | \Sigma(\varepsilon_i^{\mathrm{QP}}) | \phi_i^{\mathrm{KS}} \rangle. \tag{2.89}$$

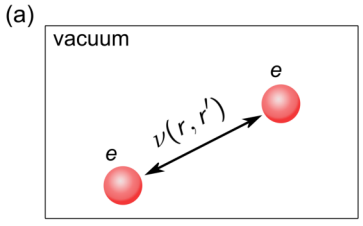

bare interaction:

$$\nu(r,r') = \frac{1}{4\pi\varepsilon_0}\frac{e^2}{|r-r'|}$$

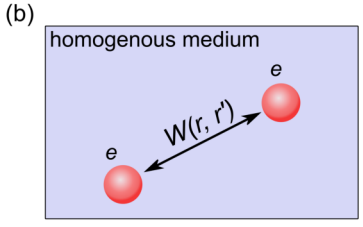

screened interaction:

$$W(r,r') = \frac{1}{4\pi\varepsilon_0\varepsilon_r}\frac{e^2}{|r-r'|}$$

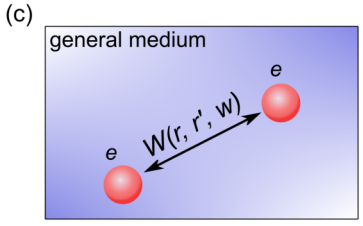

dynamically screened interaction:

$$W(r,r',w) = \frac{e^2}{4\pi\varepsilon_0}\int dr''\frac{\varepsilon^{-1}(r,r'',w)}{|r'-r''|}$$

Figure 2.4: Diagrammatic representation of the bare Coulomb interaction, screened interaction and dynamically screened interaction.

Assuming that the Kohn-Sham equation is adequate to provide a good description concerning the system, the difference between the self-energy and Kohn-Sham exchange-correction contribution is expected to be small. Therefore, the self-energy at the particle energy can be expanded around the energy $\varepsilon_i^{\mathrm{KS}}$ to the first order,

$$\Sigma_i(\varepsilon_i^{\mathrm{QP}}) \approx \Sigma_i(\varepsilon_i^{\mathrm{KS}}) + (\varepsilon_i^{\mathrm{QP}} - \varepsilon_i^{\mathrm{KS}}) \left.\frac{\partial \Sigma_i(\omega)}{\partial \omega}\right|_{\omega=\varepsilon_i^{\mathrm{QP}}}. \tag{2.90}$$

Such simplification allows us to evaluate the self-energy from the KS energies rather than QP energies, which can dramatically reduce the computational requirement at the cost of accuracy. Then we can estimate the roots of Eq. (2.89) by the Newton-Raphson method:

$$\varepsilon_i^{\mathrm{QP}} = \varepsilon_i^{\mathrm{KS}} + Z_i \langle \phi_i^{\mathrm{KS}} | \Sigma(\varepsilon_i^{\mathrm{KS}}) - v_{xc}^{\mathrm{KS}} | \phi_i^{\mathrm{KS}} \rangle, \tag{2.91}$$

where Z_i is called the renormalization factor ranging from 0 to 1, describing the correlation grade in materials,

$$Z_i = \left\langle \phi_i^{\mathrm{KS}} \middle| 1 - \left.\frac{\partial \Sigma(\omega)}{\partial \omega}\right|_{\omega=\varepsilon_i^{\mathrm{QP}}} \middle| \phi_i^{\mathrm{KS}} \right\rangle^{-1}. \tag{2.92}$$

If $Z_i \approx 1$, it means an electronically less correlated system, indicating it is very close to a real quasi-particle wavefunction. But if $Z_i \ll 1$, it implies a poor description for the system. Obviously, from the Eq. (2.91), the quality of results is strongly starting-point dependent due to its perturbation nature. Such a method, where the input KS energies are corrected to yield better electronic energy levels, is known as the one-shot GW or G_0W_0 approach. In the G_0W_0 approach, there is no iteration, no update of G and W. The standard process of G_0W_0 approach is:

1. Perform DFT (or HF) calculation to provide the single-particle eigenvalues and eigenfunction in ground-state of the considered system;

2. Construct the one-particle Green's function and polarizability according to Eq. (2.76) and Eq. (2.88);

3. Determine the screened Coulomb energy and self-energy according to Eq. (2.83) and Eq. (2.87);

4. Obtain the QP energies and QP wavefunctions according to Eq. (2.91).

The G_0W_0 method has achieved great success for the prediction of electronic band structure, especially for the band gap of semiconductors and insulators.[163] The calculated QP band gaps by G_0W_0 are collected in Table 2.2, which are much closer to the experimental values in comparison with DFT results for the considered systems. But the dependency of G_0W_0 approach on the choice of starting wavefunction is an issue. To tackle this problem, one can employ a partially or fully self-consistent GW scheme to

tune the starting point of wavefunction.
Up to now, we discuss the HF, DFT and GW methods. To make a direct comparison, we list these different electronic structure methods:

- In density functional theory,

$$\left(-\frac{1}{2}\nabla^2 + V_{\text{ext}}(\boldsymbol{r}) + V_{\text{H}}(\boldsymbol{r}) + V_{\text{xc}}(\boldsymbol{r})\right)\phi_i(\boldsymbol{r}) = \varepsilon_i\phi_i(\boldsymbol{r}); \tag{2.93}$$

- In HF or hybrid functionals,

$$\left(-\frac{1}{2}\nabla^2 + V_{\text{ext}}(\boldsymbol{r}) + V_{\text{H}}(\boldsymbol{r})\right)\phi_i(\boldsymbol{r}) + \int V^{\text{x}}(r, r')\phi_i(\boldsymbol{r}')d^3\boldsymbol{r}' = \varepsilon_i\phi_i(\boldsymbol{r}), \tag{2.94}$$

  where V^{x} is the bare non-local Fock exchange,

$$V^{\text{x}} = -\sum_{\text{occ}} \phi_i(\boldsymbol{r})\phi_i^*(\boldsymbol{r}) \times \frac{e^2}{|\boldsymbol{r} - \boldsymbol{r}'|} = G(r, r') \underbrace{v(\boldsymbol{r}, \boldsymbol{r}')}_{\substack{\text{bare} \\ \text{interaction}}}. \tag{2.95}$$

- In GW approximation,

$$\left(-\frac{1}{2}\nabla^2 + V_{\text{ext}}(\boldsymbol{r}) + V_{\text{H}}(\boldsymbol{r})\right)\phi_i(\boldsymbol{r}) + \int \Sigma(\boldsymbol{r}, \boldsymbol{r}', \varepsilon_i)\phi_i(\boldsymbol{r}')d^3\boldsymbol{r}' = \varepsilon_i\phi_i(\boldsymbol{r}) \tag{2.96}$$

  where

$$\Sigma(\boldsymbol{r}, \boldsymbol{r}', \varepsilon_i) = iG(\boldsymbol{r}, \boldsymbol{r}', \omega) \underbrace{W(\boldsymbol{r}, \boldsymbol{r}', \omega)}_{\substack{\text{dynamically} \\ \text{screened} \\ \text{interaction}}} \tag{2.97}$$

According to the above equations, the form of GW approximation is similar to HF, but the bare interaction is replaced by dynamically screened interaction, which remedies the most serious deficiency of HF.

2.3.3 Bethe-Salpeter equation

When a material is subjected to an external perturbation, such as an optical field or fast electrons, it will respond in a manner that depends on the nature of perturbation. If the external perturbations is weak, it is possible to describe the response of the system to the external perturbation in a linear form, known as the Kubo formula.[175] Therefore, before talking about the Bethe-Salpeter equation (BSE), we firstly discuss the concept of dielectric function and its key role in describing the optical response of a material.

Dielectric function

If we apply a small external potential $v_{\text{field}}(\boldsymbol{r})$ to an electronic system with density $\rho(\boldsymbol{r})$, the electrons will move around, in other words, the system will become polarized. [176, 177] The new total density can be written as

$$\rho_{\text{tot}}(\boldsymbol{r}) = \rho_0(\boldsymbol{r}, t) + \rho_{\text{ind}}(\boldsymbol{r}, t), \tag{2.98}$$

where $\rho_{\text{ind}}(\boldsymbol{r}, t)$ is the induced density. The external potential can be considered to cause a small perturbation to the Hamiltonian

$$\hat{H}'(t) = \int \hat{\rho}(\boldsymbol{r}) v_{\text{field}}(\boldsymbol{r}, t) d\boldsymbol{r}, \tag{2.99}$$

where $\hat{\rho}(\boldsymbol{r})$ is the density operator and it is assumed that the perturbation has been adiabatically turned on in the infinite past. Since the magnitude of the perturbation is small enough, the induced density can be calculated by applying the Kubo formula:

$$\rho_{\text{ind}}(\boldsymbol{r}, t) = \int_{t_0}^{t} dt' \int d\boldsymbol{r}' \chi^r(\boldsymbol{r}, \boldsymbol{r}', t, t') v_{\text{field}}(\boldsymbol{r}', t') \tag{2.100}$$

where $\chi^r(\boldsymbol{r}, \boldsymbol{r}', t, t')$ is the retarded density-density response function and can be obtained in terms of the density operator as

$$\chi^r(\boldsymbol{r}, \boldsymbol{r}', t, t') = -i\theta(t - t')\langle[\hat{\rho}(\boldsymbol{r}, t), \hat{\rho}(\boldsymbol{r}', t')]\rangle_0. \tag{2.101}$$

where the equilibrium average, $\langle\rangle_0$, of the commutator is taken. If we assume that the external potential oscillates periodically with time, namely, $v_{\text{field}}(\boldsymbol{r}', t') = v_{\text{field}}(\boldsymbol{r}')e^{i\omega t'}$, the Eq. (2.100) is conveniently transformed to Fourier space

$$\rho_{\text{ind}}(\boldsymbol{r}, \omega) = \int d\boldsymbol{r}' \chi(\boldsymbol{r}, \boldsymbol{r}', \omega) v_{\text{field}}(\boldsymbol{r}', \omega), \tag{2.102}$$

where χ is density-density response function, also known as electric susceptibility, reducible polarizability or the interacting density response function. The reducible polarizability χ and irreducible polarizability P are related by a Dyson-like equation

$$\chi(\boldsymbol{r}, \boldsymbol{r}', \omega) = P(\boldsymbol{r}, \boldsymbol{r}', \omega) + \int \int d\boldsymbol{r} d\boldsymbol{r}' P(\boldsymbol{r}, \boldsymbol{r}', \omega) v(\boldsymbol{r}, \boldsymbol{r}') \chi(\boldsymbol{r}, \boldsymbol{r}', \omega) \tag{2.103}$$

Note that $v(\boldsymbol{r}, \boldsymbol{r}')$ is the bare Coulomb potential, which is related to the induced potential v_{ind} by

$$v_{\text{ind}}(\boldsymbol{r}, t) = \int d\boldsymbol{r}' v(\boldsymbol{r}, \boldsymbol{r}') \hat{\rho}(\boldsymbol{r}', t). \tag{2.104}$$

The total potential can be written as the external potential plus the induced potential,

$$v_{\text{tot}} = v_{\text{field}} + v_{\text{ind}}. \tag{2.105}$$

The dielectric function is one of the fundamental quantities in solid, which is used to measure the screening in the system arising from polarization effects. The external potential $v_{\text{field}}(\boldsymbol{r}, t)$ is related to the total potential $v_{\text{tot}}(\boldsymbol{r}', t')$ by the dielectric function $\epsilon(\boldsymbol{r},, t; \boldsymbol{r}'.t')$:

$$v_{\text{field}}(\boldsymbol{r}, t) = \int \int \epsilon(\boldsymbol{r}, t; \boldsymbol{r}', t') v_{\text{tot}}(\boldsymbol{r}', t') dt' d\boldsymbol{r}'. \tag{2.106}$$

Employing the Kubo formula to get the induced potential and Fourier transforming in time, we can further obtain the dielectric function by the form of

$$\epsilon^{-1}(\boldsymbol{r}, \boldsymbol{r}', \omega) = \frac{\delta v_{\text{tot}}(\boldsymbol{r}', \omega)}{\delta v_{\text{field}}(\boldsymbol{r}, \omega)} = \delta(\boldsymbol{r} - \boldsymbol{r}') + \int v(\boldsymbol{r}, \boldsymbol{r}'') \chi(\boldsymbol{r}'', \boldsymbol{r}', \omega) d\boldsymbol{r}'', \tag{2.107}$$

The dielectric function and the irreducible polarisability are related by:

$$\epsilon(\boldsymbol{r}, \boldsymbol{r}', \omega) = \delta(\boldsymbol{r}, \boldsymbol{r}') - \int d\boldsymbol{r}'' v(\boldsymbol{r}, \boldsymbol{r}'') P(\boldsymbol{r}'', \boldsymbol{r}', \omega). \tag{2.108}$$

Within the RPA approximation, the dielectric function can be expressed in terms of non-interacting density response function χ^0:

$$\epsilon^{-1}(\boldsymbol{r}, \boldsymbol{r}', \omega) = \delta(\boldsymbol{r} - \boldsymbol{r}'') + \int v(\boldsymbol{r} - \boldsymbol{r}'') \chi^0(\boldsymbol{r}'', \boldsymbol{r}', \omega) d\boldsymbol{r}''. \tag{2.109}$$

For a periodic system, like crystal, it is favorable to work in reciprocal space and the dielectric function within RPA approximation takes the form:

$$\epsilon_{G,G'}(\boldsymbol{q}, \omega) = \delta_{G,G'} - \frac{4\pi}{|\boldsymbol{q} + \boldsymbol{G}|^2} \chi^0_{G,G}(\boldsymbol{q}, \omega), \tag{2.110}$$

Here $\boldsymbol{G}$ denotes a reciprocal lattice vector and $\boldsymbol{q}$ the point grid in the Brillouin zone.

BSE

In the previous part, we discussed the RPA approximation, which is sufficient to describe the photoemission spectrum; while for the photoluminescence (PL), one has to go beyond the one-particle scheme. Although RPA approximation is a many-body formalism according to the definition, it does not consider the electron-hole interactions (excitonic effect) due to the simplification of irreducible polarisation ($P = iGG$). From the physical point of view, the accurate irreducible polarisation is an electron-hole pair propagator, which propagates simultaneously and interacts with each other. Therefore, the ignorance of the excitonic effect in RPA approximation makes it inadequate to describe the optical

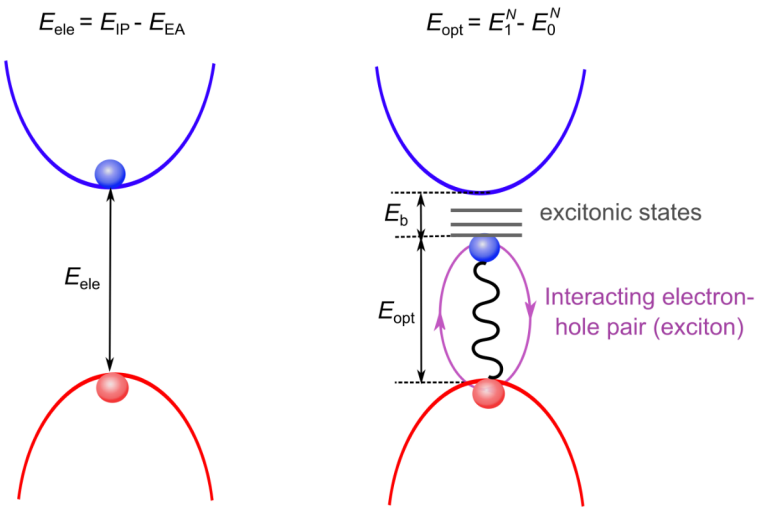

Figure 2.5: Definition of the electronic band gap E_{ele} and optical band gap E_{opt}. The E_{ele} represents the excitation of an electron from the occupied bands to the unoccupied bands without the interaction between the excited electron (blue) and created hole (red), e.g. $E_{ele} = E_{IP} - E_{EA}$. The bound electron-hole pair, called exciton, is shown in purple. The excitation energy to the first excitonic state is then defined as the optical band gap (E_{opt}), e.g. $E_{opt} = E_1^N - E_0^N$. The binding energy of exciton is given by $E_b = E_{ele} - E_{opt}$.

properties of materials.

The band gap that we mentioned in the previous sections will now be redefined as the electronic band gap, and we will introduce the optical band gap as the energy difference associated with the exciton. An exciton is created when an electron is excited from the valence band to the conduction band leaving a hole behind as described in Figure 2.5. The difference between the electronic band gap and optical band gap is called excitonic binding energy. It can be as large as several hundred meV, especially for 2D materials or several layer structures owing to their low dielectric screening. The interactive Coulomb interaction between electron-hole leads to the formation of excitonic states. These excitonic states are easily to identify and show up in the PL spectrum as narrow peaks below the electronic band gap due to their high oscillator strength.

To capture the excitonic effect, we have to make a better approximation for the irreducible polarization by considering the electron-hole interaction. To achieve that, Bethe and Salpeter introduce the interacting four-point reducible polarizability L (known as two-body correlation function) since an exciton is related to two-particle problem,[178]

$$L(1,2;3,4) = -iG(1;3)G(4;2) + G_2(1,2;3,4), \tag{2.111}$$

where $G_2(1,2;3,4)$ is a two-particle Green's function,

$$G_2(1,2;3,4) = -\langle N|\hat{T}\hat{\psi}(1)\hat{\psi}(2)\hat{\psi}(3)^{\dagger}\hat{\psi}(4)^{\dagger}|N\rangle. \tag{2.112}$$

The four-point reducible polarizability will reduce to the reducible polarizability when its coordinates are contracted in the following manner,

$$\chi(1;2) = L(1,1^+;2,2^+). \tag{2.113}$$

As proposed by Bethe and Salpeter, the interacting four-point reducible polarisability satisfies a Dyson equation,

$$L(1,2;3,4) = L_0(1,2;3,4) + \int d(5,6,7,8)L_0(1,2;3,4)K(5,6;7,8)L(1,2;3,4), \tag{2.114}$$

which goes under the name of the Bethe-Salpeter equation (BSE). Here $L_0(1,2;3,4)$ is non-interacting reducible polarisability,

$$L_0(1,2;3,4) = -iG(1;3)G(4,2); \tag{2.115}$$

and K is an interaction kernel that takes into account the many-body effects in the system and can be expressed as:

$$K(1,2;3,4) = v(1,3)\delta(1,2)\delta(3,4) + i\frac{\delta\Sigma(1;2)}{\delta G(3;4)} \tag{2.116}$$

Now let us discuss the meaning of Eq. (2.114). When the kernel is equal to zero, $K = 0$, the BSE will reduce to $L = L_0$, corresponding to the four-point version of the RPA in Eq. (2.88). The RPA consists of a simple product of free propagators of an electron and a hole without interacting. When the K differs from zero, the interaction between the electron and hole is introduced in a self-consistent manner through the Dyson equation. To proceed further, we need to specify an approximation for self-energy (Σ) and further evaluate its derivative with respect to the Green's function ($\delta\Sigma/\delta G$). For that, we adopt the GW approximation for the self-energy, namely Eq. (2.87), and disregard the variation of the screened interaction, i.e. $\delta W(1;2)/\delta G(3;4) = 0$. This is because this term is much more cumbersome to be calculated. Besides, up to now, there is no strong evidence that it is crucial to include this term. Therefore, we can rewrite the Eq. (2.116) as

$$K(1,2;3,4) = v(1,3)\delta(1,2)\delta(3,4) - \delta(1,3)\delta(2,4)W(1,2). \tag{2.117}$$

By employing the static approximation for the screened interaction, namely $W(1,2) = 1/2\pi W(\boldsymbol{r}_1,\boldsymbol{r}_2,\omega = 0)\delta(t_1,t_2)$, we can rewrite the BSE equation as a simple product in frequency space:

$$L(\boldsymbol{r}_1,\boldsymbol{r}_2,\boldsymbol{r}_3,\boldsymbol{r}_4;\omega) = L_0(\boldsymbol{r}_1,\boldsymbol{r}_2,\boldsymbol{r}_3,\boldsymbol{r}_4;\omega)+$$

$$\int d(\boldsymbol{r}_5, \boldsymbol{r}_6, \boldsymbol{r}_7, \boldsymbol{r}_8) L_0(\boldsymbol{r}_1, \boldsymbol{r}_2, \boldsymbol{r}_3, \boldsymbol{r}_4; \omega) K(\boldsymbol{r}_5, \boldsymbol{r}_6, \boldsymbol{r}_7, \boldsymbol{r}_8) L(\boldsymbol{r}_1, \boldsymbol{r}_2, \boldsymbol{r}_3, \boldsymbol{r}_4; \omega), \tag{2.118}$$

or even more simply

$$L(\omega) = L_0(\omega) + L_0(\omega) K L(\omega). \tag{2.119}$$

Here the kernel K is frequency independent within the static approximation. To solve the above equation, the exciton state is introduced based on the two-particel space. In such space, the basis function is a product of two single-particle wave functions:

$$\phi_S(\boldsymbol{r}_1, \boldsymbol{r}_2) = \phi^*_{n_1,\boldsymbol{k}}(\boldsymbol{r}_1) \phi_{n_2,\boldsymbol{k}+\boldsymbol{q}}(\boldsymbol{r}_2), \tag{2.120}$$

where n corresponds to the KS orbital states; the $\boldsymbol{k}$ and $\boldsymbol{q}$ are the momentum in the two-particel space; S is the contracted notation, i.e. $S = (n_1, n_2, \boldsymbol{k}, \boldsymbol{k}+\boldsymbol{q})$. From now on, we will use the notation of S to represent the BSE equation.After projecting the BSE (Eq. (2.118)) to the two-particle space, we obtain

$$L(\boldsymbol{r}_1, \boldsymbol{r}_2, \boldsymbol{r}_3, \boldsymbol{r}_4; \omega) = \sum_{\boldsymbol{q}}^{\mathrm{BZ}} \sum_{SS'} L_{SS'}(\boldsymbol{q}) \phi_S(\boldsymbol{r}_1, \boldsymbol{r}_2) \phi^*_{S'}(\boldsymbol{r}_3, \boldsymbol{r}_4), \tag{2.121}$$

where $L_{SS'}(\boldsymbol{q})$ is diagonal in $\boldsymbol{q}$ follows from the translational invariance of the system. As anticipated above, $L_{SS'}(\boldsymbol{q}, \omega)$ is found through the following spectral representation

$$L_{SS'}(\boldsymbol{q}, \omega) = \sum_{\lambda\lambda'} \frac{A^S_\lambda(\boldsymbol{q}) [A^{S'}_{\lambda'}(\boldsymbol{q})]^* N^{-1}_{\lambda\lambda'}(\boldsymbol{q})}{\omega - E_\lambda(\boldsymbol{q}) - i\eta} \tag{2.122}$$

where $N_{\lambda\lambda'}$ is the overlap matrix, $N_{\lambda\lambda'}(\boldsymbol{q}) = \sum_S [A^S_\lambda(\boldsymbol{q})]^* A^{S'}_{\lambda'}(\boldsymbol{q})$; $A^S_\lambda(\boldsymbol{q})$ and $E_\lambda(\boldsymbol{q})$ are the eigenfunctions and eigenvalues of the non-hermitian two-particle Hamiltonian $H_{SS'}(\boldsymbol{q})$, respectively,

$$H_{SS'}(\boldsymbol{q}) = (\epsilon_{n_2,\boldsymbol{k}+\boldsymbol{q}} - \epsilon_{n_1,\boldsymbol{k}}) \delta_{SS'} - (f_{n_2,\boldsymbol{k}+\boldsymbol{q}} - f_{n_1,\boldsymbol{k}}) K_{SS'}(\boldsymbol{q}). \tag{2.123}$$

Here, the $f_{n,k}$ and $\epsilon_{n,k}$ are the occupation density and dielectric function of state n with moment k, respectively. The diagonal part of $H_{SS'}$ consists of single-particle transition energies while the off-diagonal terms are given by the BSE kernel $K_{SS'}(\boldsymbol{q})$ in the two-particle space. The kernel in the two-particle space is rewritten as

$$K_{SS'}(\boldsymbol{q}) = V_{SS'}(q) - \frac{1}{2} W_{SS'}(q). \tag{2.124}$$

The factor 1/2 is generated by the optical selection rule. In this way, we can convert the BSE equation to a Schrödinger-like equation

$$H_{SS'}A^S_\lambda = E^S_\lambda A^S_\lambda. \tag{2.125}$$

In the practical calculation, to simplify the diagonalization we employ a further approximation, referred to Tamm-Dancoff approximation.[179] This approximation restricts the two-particle space to only the positive frequency transitions, namely transitions from the valence to conduction band. The final expression for the reducible polarizability matrix is [165]

$$\chi_{GG'}(\boldsymbol{q},\omega) = \frac{1}{\Omega}\sum_{SS'} L_{SS'}(\boldsymbol{q},\omega)\rho_S(\boldsymbol{G})\rho_{S'}(\boldsymbol{G}), \tag{2.126}$$

with Ω volume of unit cell.

2.4 Periodic systems

In a solid, the problem of electrons is in principle a many-electron problem. The full Hamiltoniam of the solid contains not only the one-electron potentials describing the interactions of the electrons with atomic nuclei, but also pair potentials describing the electron-electron interactions. X-ray diffraction investigation has proven, that in a crystal, the atoms are arranged periodically. For many solids, it is a good approximation to look at them as crystals since they consist of small groups of atoms that are arranged in a repetitive manner. In this way, under suitable assumptions, the many-electrons problem for many solids can be converted into the much simpler problem of an electron in a periodic potential.

2.4.1 Electrons in a periodic potential

The fundamental property of a crystal is regularity in its atomic structure, in other words, the atoms in a crystal are arranged in a periodic array. To define a crystal, two concepts, a lattice and a basis, are introduced. A lattice is a set of points in space that form a periodic structure. Each point sees the same environment as all others. Any lattice point in the unit cell can be described by

$$\boldsymbol{r}' = \boldsymbol{r} + n_1\boldsymbol{a_1} + n_2\boldsymbol{a_2} + n_3\boldsymbol{a_3} = \boldsymbol{r} + \boldsymbol{T}, \tag{2.127}$$

where $\boldsymbol{a_1}$, $\boldsymbol{a_2}$ and $\boldsymbol{a_3}$ are vectors, which are linearly independent; n_1, n_2 and n_3 are integers whose values depend on the lattice site. $\boldsymbol{T}$ is a translation vector. Either the collection of lattice points, or the primitive translation vectors which construct the lattice is referred to as a Bravais lattice. A basis is a collection of atoms in a particular fixed arrangement in space, consisting of perhaps many atoms. For graphene, where the basis consists of two carbon atoms and the two lattice vectors for 2D periodic lattice are given in Figure 2.6(a).
When we want to examine the properties of an electron in a periodic lattice, we need to consider Schrödinger's equation, such that the potential energy term $V(\boldsymbol{r})$ reflects the fact that the electrons see a periodic potential. A typical crystalline potential might be expected to have the form shown in Figure 2.7, assuming an ionized atom located at each lattice point. The potential energy is obviously periodic, i.e. $V(\boldsymbol{r}) = V(r + a)$. This means that if we pick up the crystal and move it by one lattice constant, it would look exactly the same as before we moved it. Such property is known as translational invariance. Owning to the translational invariance of the potential, the physical properties of any wavefunction that is a solution to the Schrödinger equation also shares the same properties, such as orbitals and electron density. To better describe the properties of the crystal, the periodic functions are subjected to Fourier analysis, which transfers the real space coordinates to the reciprocal coordinates. For example, the density can be

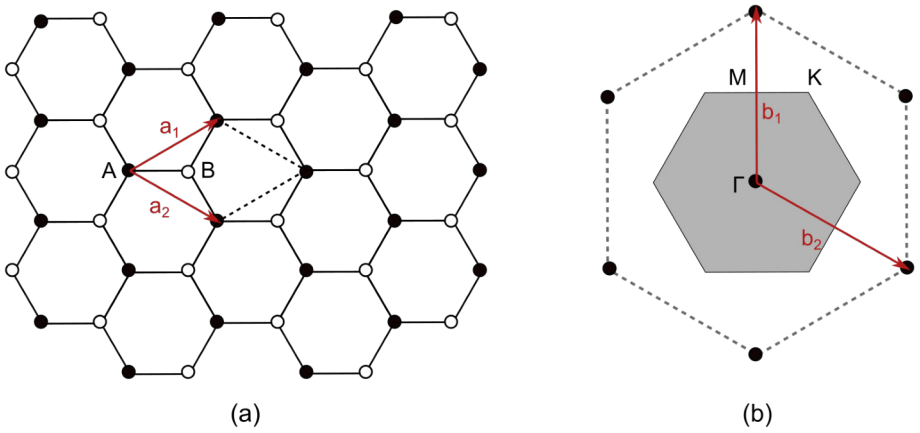

Figure 2.6: (a) The lattice structure of graphene consisting of two identical hexagonal sublattices A (black ball) and B (white ball). (b) The first Brillouin zone of graphene (marked with gray hexagons). Atom A and B form a basis and all black (or white) balls form a Bravais lattice. The lattice and reciprocal lattice vectors are represented in $\boldsymbol{a}$ and $\boldsymbol{b}$, respectively. The high-symmetry points Σ, K and M are also shown.

expanded by a Fourier transformation

$$\rho(\boldsymbol{r}) = \sum_{G} \rho_G e^{iG\boldsymbol{r}}, \tag{2.128}$$

where $\boldsymbol{G}$ is a set of vectors in reciprocal space. Similar to $\boldsymbol{T}$, $\boldsymbol{G}$ has the following form:

$$\boldsymbol{G} = k_1\boldsymbol{b_1} + k_2\boldsymbol{b_2} + k_3\boldsymbol{b_3}, \tag{2.129}$$

where k_1, k_2 and k_3 are integers, and the Miller indices (k_1, k_2, k_3), called Miller indices, indicates the perpendicular direction of a plane of atoms in a crystal; $\boldsymbol{b_1}$, $\boldsymbol{b_2}$ and $\boldsymbol{b_3}$ are the reciprocal lattice vectors. The latters are related to the real space lattice vectors by:

$$|\boldsymbol{b_i}| = \frac{2\pi}{|\boldsymbol{a_i}|}, \tag{2.130}$$

where the factor 2π is introduced by the Fourier transforms. In reciprocal space, we define the Wigner-Seitz primitive cell as Brillouin zone (BZ). The first Brillouin zone is the smallest volume entirely enclosed by planes obtained by bisecting with perpendicular planes nearest neighbors reciprocal lattice vectors (see Figure 2.6(b)). There are also the second, third and so on Brillouin zone, but these are used more rarely since the first Brillouin zone contains almost all information that we need.

Up to now, we introduced the basic concepts in solid state. Next, we turn to the Schrödinger equation for an electron in a periodic potential.

▶ **Theorem 2.3 (Bloch's theorem).** The eigenstates ψ of the one-electron Hamiltonian $\hat{H} = -\hbar^2\nabla^2/2m + V(\boldsymbol{r})$, where $V(\boldsymbol{r} + \boldsymbol{R}) = V(\boldsymbol{r})$ for all $\boldsymbol{R}$ in a Bravais lattice, can be

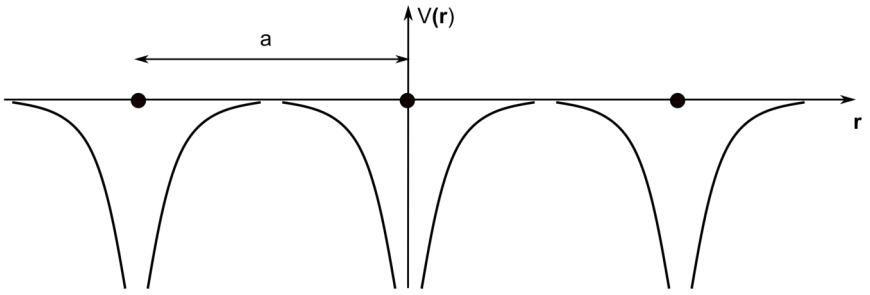

Figure 2.7: One-dimensional visualization of potential $V(\boldsymbol{r})$ versus position $\boldsymbol{r}$ in a periodic lattice. a is the period of the lattice.

chosen to have the form of a plane wave times a function with the periodicity of the Bravais lattice:

$$\psi_{n\boldsymbol{k}}(\boldsymbol{r}) = \mu_{n\boldsymbol{k}}(\boldsymbol{r})e^{i\boldsymbol{k}\boldsymbol{r}}, \tag{2.131}$$

where n is called band index; $\boldsymbol{k}$ is the wavevector in the Brillouin zone; $\mu_{n\boldsymbol{k}}$ is a periodic function with the periodicity of the lattice,

$$\mu_{n\boldsymbol{k}}(\boldsymbol{r}+\boldsymbol{R}) = \mu_{n\boldsymbol{k}}(\boldsymbol{r}), \tag{2.132}$$

for all $\boldsymbol{R}$ in the Bravais lattice.
Bloch's theorem is sometimes stated in this alternative form: the eigenstates of $\hat{H}$ can be chosen so that associated with each ψ is a wave vector $\boldsymbol{k}$ such that

$$\psi(\boldsymbol{r}+\boldsymbol{R}) = \psi(\boldsymbol{r})e^{i\boldsymbol{k}\boldsymbol{R}} \tag{2.133}$$

◀

In Bloch's theorem, the wave vector k is confined to the first Brillouin zone because any k' not within the first Brillouin zone can be expressed as

$$\boldsymbol{k}' = \boldsymbol{k} + \mathbf{G}. \tag{2.134}$$

In addition, the appearance of the band index n in Bloch's theorem is caused by the fact that for a given $\boldsymbol{k}$, there are many solutions to the Schrödinger equation. As $\boldsymbol{k}$ becomes continuous, these solutions form energy bands. Using Bloch's theorem in the one-electron Schrödinger equation,

$$\begin{aligned}\hat{H}e^{i\boldsymbol{k}\boldsymbol{r}}\mu_{n\boldsymbol{k}}(r) &= \left[-\frac{\hbar^2}{2m}\nabla^2 + V(\boldsymbol{r})\right]e^{i\boldsymbol{k}\boldsymbol{r}}\mu_{n\boldsymbol{k}}(r) \\ &= e^{i\boldsymbol{k}\boldsymbol{r}}\left[-\frac{\hbar^2}{2m}\nabla^2 - 2\frac{\hbar^2}{2m}i\boldsymbol{k}\nabla + \frac{\hbar^2}{2m}\boldsymbol{k}^2 + V(\boldsymbol{r})\right]\mu_{n\boldsymbol{k}}(r)\end{aligned}$$

$$= e^{i\boldsymbol{k}\boldsymbol{r}}\left[\frac{\hbar^2}{2m}(-i\nabla+\boldsymbol{k})^2+V(\boldsymbol{r})\right]\mu_{n\boldsymbol{k}}(r), \tag{2.135}$$

we find that $\mu_{n\boldsymbol{k}}(r)$ is determined by the eigenvalue problem

$$\left[\frac{\hbar^2}{2m}(-i\nabla+\boldsymbol{k})^2+V(\boldsymbol{r})\right]\mu_{n\boldsymbol{k}}(r) = E_n(\boldsymbol{k})\mu_{n\boldsymbol{k}}(r), \tag{2.136}$$

with boundary conditions of Eq. (2.132). Owing to the periodic boundary condition, Eq. (2.136) is in fact an eigenvalue problem restricted to a single primitive cell of the crystal. Accordingly, in the fixed finite volume, we will get an infinite number of discrete eigenvalues $E_n(\boldsymbol{k})$ for each $\boldsymbol{k}$, which is labeled with the band index n. The set of eigenvalues $E_n(\boldsymbol{k})$ is usually called band structure. Bloch's theorem can be denoted by $\psi_{n\boldsymbol{k}}(r)$ which indicates that each value of band index n and vector $\boldsymbol{k}$ specifies an electron state or orbital in solid state physics with energy $E_n(\boldsymbol{k})$.
In solid physics, another property that we are interested in is the density of states (DOS). It is defined as the number of energy eigenstates $N(E)$ in the interval $E \to E+dE$ per unit volume and per spin:

$$\begin{aligned} N(E) &= \frac{1}{V}\sum_{n;\boldsymbol{k}\in BZ}\delta[E-E_n(\boldsymbol{k})], \\ &= \sum_n \int_{BZ}\frac{d^3k}{(2\pi)^3}\delta[E-E_n(\boldsymbol{k})], \quad \text{for } V\to\infty. \end{aligned}$$

Here, V denotes the macroscopic volume and E has units of energy in real space. Then, we can express the delta function in terms of a surface integral,

$$N(E) = \frac{1}{2\pi^3}\sum_n \int_{S(E)}\frac{d^2k}{\nabla_{\boldsymbol{k}}E_n(\boldsymbol{k})}, \tag{2.137}$$

where $S(E)$ is the surface in reciprocal space that is defined by the solution of $E = E_n(\boldsymbol{k})$ with respect to $\boldsymbol{k}$; $\nabla_{\boldsymbol{k}}E_n(\boldsymbol{k})$ is given by

$$\nabla_{\boldsymbol{k}}E_n(\boldsymbol{k}) = \frac{\partial E_n(\boldsymbol{k})}{\partial k(\boldsymbol{k})}\boldsymbol{n}(\boldsymbol{k}), \tag{2.138}$$

where $\boldsymbol{n}$ is the unit vector with a direction perpendicular to $E_n(\boldsymbol{k}) = E$. Generally, the shapes of DOS curves are predictable from the band structure. Besides, the flatter the band, the greater the DOS at the energy.

2.4.2 Basis set

In simulations of periodic solids, different families of basis have been developed to expand the electronic wavefunctions. The choice of basis is of paramount importance because it

determines not only the numerical accuracy but also the computational cost of electronic methods. In the following, we will introduce the most common basis sets with brief comments.

Plane Wave

Bloch's theorem states that each electronic wavefunction in a periodic solid takes the form of a plane wave modulated by a periodic function (see Eq. (2.131)). The periodic function can be expanded in a set of plane waves, whose wave vectors are reciprocal lattice vectors of the crystal $\boldsymbol{G}$:[180]

$$\mu_{n\boldsymbol{k}} = \sum_{\boldsymbol{G}} C_{n,\boldsymbol{G}} e^{i\boldsymbol{G}\boldsymbol{r}}, \tag{2.139}$$

where $C_{n,\boldsymbol{G}}$ are the expansion coefficients. Accordingly, each wavefunction can be written as a sum of plane waves

$$\psi_{n\boldsymbol{k}} = \sum_{\boldsymbol{G}} c_{n,\boldsymbol{k}+\boldsymbol{G}} e^{i(\boldsymbol{k}+\boldsymbol{G})\boldsymbol{r}}. \tag{2.140}$$

Theoretically, we can use an infinite plane wave basis set to expand the electronic wavefunction. But it turns out that the coefficients $c_{n,\boldsymbol{k}+\boldsymbol{G}}$ with small kinetic energy are more important for the plane waves than those with large kinetic energy.[180] Thus, in practice, we truncate the plane wave basis set and consider the corresponding plane wave only when its kinetic energy is smaller than a certain cutoff energy E_{cut},

$$\frac{1}{2}|\boldsymbol{k}+\boldsymbol{G}|^2 \leq E_{\text{cut}}. \tag{2.141}$$

In practical calculations, a key issue in the plane wave method is the choice of the cutoff energy. This parameter is usually determined by testing the convergence of quantities of interest, such as the energy, the electron density, or the forces and stresses. We also have to note that a larger cut-off will lead to more accurate results, but at the price of increasing the computational cost significantly.
A built-in advantage of the plane wave method is its independence with respect to the atomic position and species, and therefore, it does not suffer from basis set superposition errors.[181] But the wavefunctions of valence electrons, which oscillate rapidly in the core region in order to satisfy the orthogonality constraint, require a large number of plane waves. Therefore, the plane wave method is used in combination with pseudopotentials or the projected-augmented wave method.

Augmented plane wave

The wavefunctions exhibit different manners in the different regions of space. In the bonding region, it is smooth, while in the core region, it displays rapid oscillations.

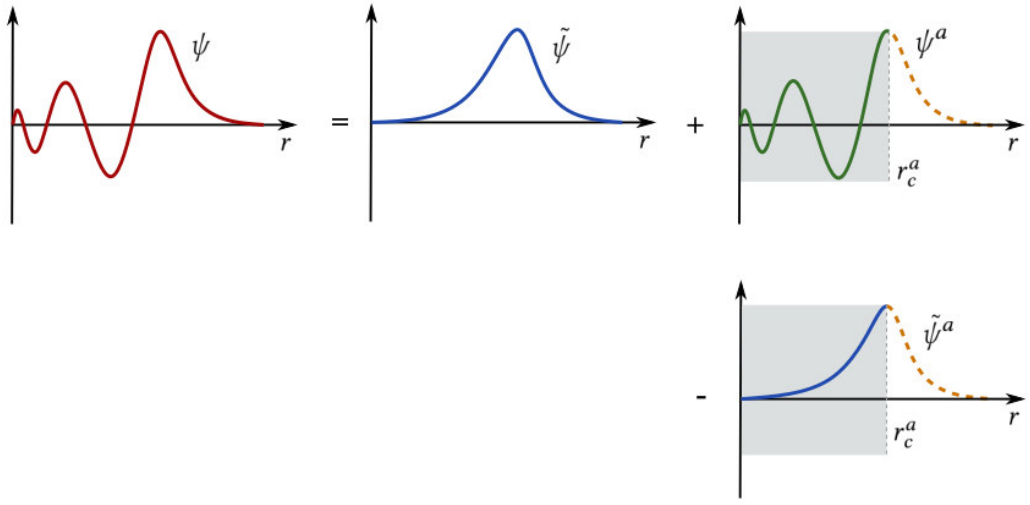

Figure 2.8: Schematic representation of PAW.[186] The all electron wavefunction $\psi_{n\boldsymbol{k}}$ is the sum of a smooth auxiliary function $\tilde{\psi}_{n\boldsymbol{k}}$ and correction term. r_c^a is the cutoff radii.

Augmented plane wave (APW) is another family of basis sets to deal with the rapidly varying oscillation near the nuclei. This method is first proposed by Slater in 1937.[182] Thereafter, several methods are developed on the basis of projector augmented wave (PAW) to get rid of the energy dependency, such as the linearized augmented plane wave (LAPW)[183] and linearized augmented plane wave with local orbitals (LAPW+lo).[184, 185] In the APW method, the real space is partitioned into two different types of region, namely (1) muffin-tins sphere Ω_1, which is centered around each nucleus a; (2) interstitial regions Ω_2 between these spheres. In the Ω_1, the potential is assumed to be spherically symmetric. The APW consist of

$$\psi_G(\boldsymbol{k},\boldsymbol{r}) = \begin{cases} e^{i(\boldsymbol{k}+\boldsymbol{G})\boldsymbol{r}}, & \mathrm{r} \in \Omega_1, \\ \sum_{lm} a_L^{\mu G}(\boldsymbol{k})\mu_l(r^\mu, E)Y_L(\hat{\boldsymbol{r}}^\mu), & \mathrm{r} \in \Omega_2, \end{cases} \tag{2.142}$$

where L is short for the quantum numbers lm; $\mu_l(r^\mu, E)$ is the numerical solution to the radial Schrödinger equation at the energy E; $a_L^{\mu G}$ are coefficient determined from the requirement that the wavefunctions are continuous at the boundary of the muffin-tins spheres.

Pseudopotentials

As we discussed before, the plane wave method needs a large number of plane waves to describe the rapid oscillations of the wavefunctions of the valence electrons. We know that most physical properties of solids depend on the valence electrons rather than core electrons. The pseudopotential approximation employs the screening effects of the

core electrons on the valence electrons to replace the nuclear potential with a weaker potential.[187, 188] Outside the core region, the pseudopotential is identical with the full electron potential. In the core region, the functions are smooth and nodeless and thus, they only require a small basis set.

The PAW method is an extension of the augmented wave method and the pseudopotential approximation.[189] The basic idea of PAW is to express the all-electron wavefunction $\psi_{n\boldsymbol{k}}$ for the $\boldsymbol{k}$ vector and band index n as the sum of a smooth auxiliary function $\tilde{\psi}_{n\boldsymbol{k}}$ and correction term, which contains the oscillation behavior in the core region:

$$\psi_{n\boldsymbol{k}}(r) = \tilde{\psi}_{n\boldsymbol{k}}(r) + \sum_a \left(\psi^a_{n\boldsymbol{k}}(r) - \tilde{\psi}^a_{n\boldsymbol{k}}(r)\right), \tag{2.143}$$

where a is the atom index; $\psi^a_{n\boldsymbol{k}}(r)$ and $\tilde{\psi}^a_{n\boldsymbol{k}}(r)$ are the atom-centered hard and smooth auxiliary wavefunction, respectively. The connection between $\psi_{n\boldsymbol{k}}$ and $\tilde{\psi}_{n\boldsymbol{k}}$ is established by a linear transformation $\hat{\mathcal{T}}$,

$$|\psi_{n\boldsymbol{k}}\rangle = \hat{\mathcal{T}}\left|\tilde{\psi}_{n,\boldsymbol{k}}\right\rangle. \tag{2.144}$$

The corresponding schematic representation of PAW is displayed in Figure 2.8.

2.4.3 2D systems

In the previous section, we talked about the periodic boundary conditions and plane wave method, which have been proven to be an effective way to calculate the properties of the bulk employing the translational symmetry of infinite crystal solid. In the last few decades, increasing interest has been developed in systems with reduced dimensionality like 2D systems. From a theory point of view, although 2D systems are periodic along only two dimensions, we still apply the 3D periodic boundary conditions to 2D systems in calculations. This is because it requires special implementation and is not practical if we work in the plane wave basis in the periodic direction and a real space basis with zero boundary conditions in the non-periodic direction. But since the vanishing of electron density along the non-periodic direction, the wave functions and other properties of 2D systems will be different in the non-periodic direction. For example, the Eq. (2.131) of 2D systems in Bloch's theorem can be re-written as (we assume the z direction is non-periodic),

$$\psi_{n\boldsymbol{k}_\parallel} = \mu_{n\boldsymbol{k}_\parallel}(\boldsymbol{r}_\parallel, z)e^{i\boldsymbol{k}_\parallel \boldsymbol{r}_\parallel}, \tag{2.145}$$

where $\boldsymbol{k}_\parallel$ is the wave vector in the two-dimensional Brillouin zone. For GW calculation of 2D materials performed with periodic boundary conditions in the out-of-plane direction, the direct use of Eq. (2.80) will lead to significant over-screening due to the long-range interaction between the repeated images. One method to solve this problem is to apply a large vacuum in the out-of-plane direction. But the number of basis sets and computational cost will increase greatly as the thickness of the vacuum increases.

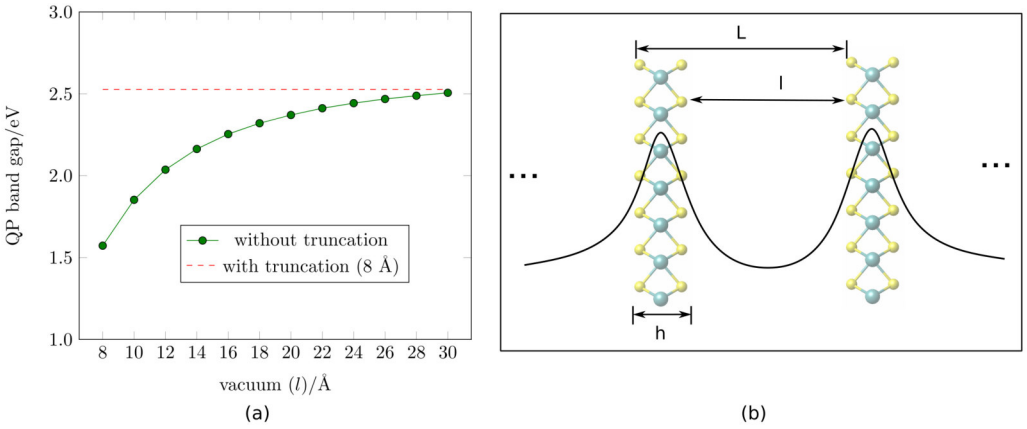

Figure 2.9: (a) The calculated QP band gap of the 2H-MoS_2 monolayer as a function of vacuum thickness with bare Coulomb potential ($\sim 1/r$). Results with 2D truncation are also shown (dashed line). All calculations are performed with PBE functional, 18×18×1 k-points sampling and 50 eV G_0W_0 self-energy. (b) Illustration of the interaction with artificial images introduced by the truncated Coulomb potential. The vacuum thickness (l), the length of the unit cell (L) and thickness of the 2H-MoS_2 (h) monolayer are also marked ($L = h + l$). The region with a width of h contains the non-vanishing density.

One effective way for this problem is to generate a truncated Coulomb potential. For low-dimensional materials, we can define a screening region Ω, where[190]

$$v_C(r) = \begin{cases} \dfrac{1}{\boldsymbol{r}}, & \mathrm{r} \in \Omega, \\ 0, & \mathrm{r} \notin \Omega. \end{cases} \tag{2.146}$$

The choice of Ω is suggested by symmetry considerations. For example, it has a spherical-shaped region for 0D systems, a cylindrical-shaped region for 1D systems and a box-shaped region for 2D systems. For 2D systems, the Coulomb potential is truncated in the out-of-plane direction in the real space[191, 192]

$$v_C^{2D}(r; r') = \frac{\theta(\frac{L}{2} - |r'_z - r_z|)}{\sqrt{(\boldsymbol{r}'_{\parallel} - \boldsymbol{r}_{\parallel})^2 + (r'_z - r_z)^2}}, \tag{2.147}$$

where L is the length of the finite unit cell in the z direction and the $L/2$ is set as the truncation length. Using the Fourier transform, we can get the following equation in reciprocal space

$$v_G^{2D}(\boldsymbol{q}_{\parallel}) = \frac{4\pi}{|\boldsymbol{q}_{\parallel} + \boldsymbol{G}|^2}\left[1 - e^{-|\boldsymbol{q}_{\parallel}+\boldsymbol{G}_{\parallel}|L/2}\cos(G_z L/2)\right], \tag{2.148}$$

with $\boldsymbol{q}$-point grid in the in-plane Brillouin zone. When $\boldsymbol{G} = 0$, the truncated Coulomb potential reduces to

$$v_0^{2D}(\boldsymbol{q}) = \frac{4\pi}{|\boldsymbol{q}|^2}(1 - e^{-|\boldsymbol{q}|L/2}). \tag{2.149}$$

It is similar to the usual untruncated 3D Coulomb potential $v(\boldsymbol{q}) = 4\pi/\boldsymbol{q}^2$ for $|q_{||} + G_{||}|L/2 \gg 1$ in the small wavelength limit.

To better illustrate the importance of the truncated Coulomb potential, here we use 2H-MoS_2 monolayer as an example. The calculated QP band gaps as a function of the vacuum thickness l without truncated Coulomb potential are displayed in Figure 2.9. The vacuum thickness l, the length of the unit cell (L) and the thickness of studied system are related by $L = h + l$. It is clear that the bare Coulomb interaction gives a very slow convergence with respect to the vacuum thickness. In up to 30 Å vacuum space, the QP band gap of 2H-MoS_2 tends to converge if no truncation is applied, whereas we can get converged results with 8 Å vacuum in the presence of the truncated Coulomb potential. Our results indicate that the employment of a truncated Coulomb potential allows us to achieve faster convergence and at the same time eliminate the interaction between the repeated images along the non-periodic direction. But the largest disadvantage of this method is that the truncation length limits the range of the GW interaction inside the material and in the two directions parallel to the surface. It means that the length of the unit cell should satisfy (refer to Figure 2.9),

$$L > 2h, \tag{2.150}$$

which increases the computation time again for thicker systems.

Macroscopic dielectric function

In the previous section, what we derived was the microscopic dielectric function which differs from the optical measurement (known as the macroscopic dielectric function). This is because the macroscopic quantities are measured on a macroscopic scale, which is slowly varying over the atomic length scale; while the microscopic quantities include the contribution from electrons in all regions of the cell and change rapidly over the unit cell. In other words, the result of optical measurement is an average over a large area of a material. Therefore, we need to calculate the averaged dielectric function, i.e. macroscopic dielectric function, on the basis of the microscopic one. The macroscopic component of the dielectric function corresponds to evaluating the $\boldsymbol{G} = \boldsymbol{G}' = 0$ of the microscopic dielectric function since the interaction potential from the light can be assumed to be constant for the size of the unit cell. In addition, the microscopic details of the dielectric function are obtained from the off-diagonal elements of the dielectric matrix, and therefore the macroscopic dielectric function is defined by 1 over the inverse

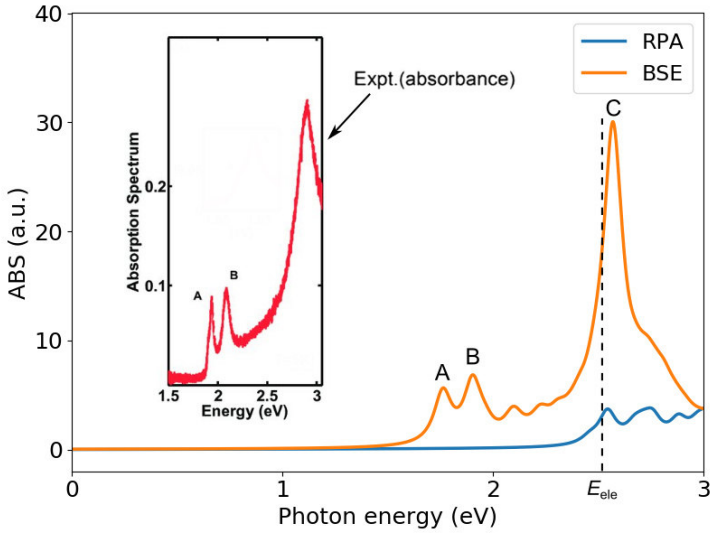

Figure 2.10: The imaginary parts of the dielectric function for monolayer MoS_2 without (RPA) and with (BSE) excitonic effect, respectively. The experimental absorption spectrum for MoS_2 is extracted from Ref [193]. The electronic band gap (E_{ele}) of MoS_2 is also shown.

microscopic dielectric function with $G = G' = 0$:

$$\epsilon_M(\boldsymbol{q},\omega) = \frac{1}{\epsilon_{00}^{-1}(\boldsymbol{q},\omega)}. \tag{2.151}$$

In general, the dielectric function consists of a real part (ϵ_1) and an imaginary part (ϵ_2); $\epsilon = \epsilon_1 + i\epsilon_2$. From the view of classical electrostatics, the real part is related to the reflectance of the material; the imaginary part is related to the absorbance of the material which is proportional to the polarisability of the material and in the optical limit in reciprocal space takes the form[194, 195]

$$\mathrm{ABS}(\boldsymbol{q}\to 0,\omega) = -4\pi \lim_{\boldsymbol{q}\to 0}\left[\frac{1}{\boldsymbol{q}^2}\mathrm{Im}P(\boldsymbol{q},\omega)\right]. \tag{2.152}$$

By taking the imaginary part of Eq. (2.108) in reciprocal space, we can get

$$\mathrm{Im}\epsilon_{GG'}(\boldsymbol{q},\omega) = v(\boldsymbol{q})\mathrm{Im}P_{GG'}(\boldsymbol{q},\omega). \tag{2.153}$$

In 3D system, the Coulomb interaction $v(\boldsymbol{q})$ scales as $4\pi/\boldsymbol{q}^2$ and thus by inserting the above equation into Eq. (2.152), one obtains the optical absorption through

$$\mathrm{ABS}^{3D}(\boldsymbol{q}\to 0,\omega) = \lim_{\boldsymbol{q}\to 0}[\mathrm{Im}\epsilon_M(\boldsymbol{q},\omega)] = \lim_{\boldsymbol{q}\to 0}\left[\mathrm{Im}\frac{1}{\epsilon_{00}^{-1}(\boldsymbol{q},\omega)}\right]. \tag{2.154}$$

But for the 2D systems, the Coulomb interaction is scaled to $1/\boldsymbol{q}$ and therefore, we can not use the above equation to get the optical absorption. But if we consider Eq. (2.103) in

reciprocal space, irreducible polarisability P can be isolated by

$$P(\boldsymbol{q},\omega) = \chi(\boldsymbol{q},\omega)(1 + v(\boldsymbol{q})\chi(\boldsymbol{q},\omega))^{-1}. \tag{2.155}$$

In all dimensions the density response function χ scales as $\boldsymbol{q}^2$ in the optical limit, which means that $v(\boldsymbol{q}_\parallel)\chi(\boldsymbol{q}_\parallel,\omega) \sim \boldsymbol{q}_\parallel$. Accordingly, the optical absorption of 2D systems can be defined from the macroscopic density response function:

$$\mathrm{ABS}^{2D}(\boldsymbol{q}\to 0,\omega) = -4\pi \lim_{\boldsymbol{q}_\parallel\longrightarrow 0}\left[\mathrm{Im}\frac{1}{\boldsymbol{q}_\parallel^2}\chi_{00}(\boldsymbol{q}_\parallel,\omega)\right]. \tag{2.156}$$

Here we use the MoS_2 monolayer as an example and the corresponding optical absorption spectra with and without excitonic effect are displayed in Figure 2.10. One can see the spectrum is completely different when including excitons and the onset of the absorption is lower than the electronic energy gap E_{ele}. From the BSE results, we can distinguish several peaks. The peaks A and B are located at 1.76 and 1.91 eV, respectively, associating with the direct transitions from the spin-orbit split valence bands to the conduction bands (about spin-orbit splitting, readers can read Ref [196]). These results agree well with the experimental observations.[193] Overall, the excitonic effects are crucial for the description of optical properties of materials.

2.4.4 Excitons

Excitons are hydrogen-like bound states of a negatively charged electron and a positively charged hole. In excitons, the electron and hole are attracted to each other by the electrostatic Coulomb force. The attractive interaction that an excited electron feels from the hole it left behind is also called excitonic binding energy. The binding energy of excitons (E_b) can be calculated by

$$E_b = E_{\mathrm{ele}} - E_{\mathrm{opt}} \tag{2.157}$$

Depending on the strength of Coulomb interaction and dielectric constant, excitons are divided into three types which are Frenkel excitons, charge-transfer excitons and Wannier-Mott excitons (see Figure 2.11). In solids with small dielectric constant, such as ionic crystals and organic molecule semiconductors composed of aromatic molecules, the Frenkel and charge-transfer excitons are typical. In the case of Frenkel excitons, the electron and hole are located on the same molecules and therefore, they have a radius comparable to the interatomic distance. Such localized excitons are tightly bounded with the exciton binding energy on the order of 0.1~1.0 eV. Regarding the charge-transfer excitons, the electron-hole pair is typically located on the nearest or next nearest molecules, which in its lowest-energy variation has an electron-hole separation of one molecule.

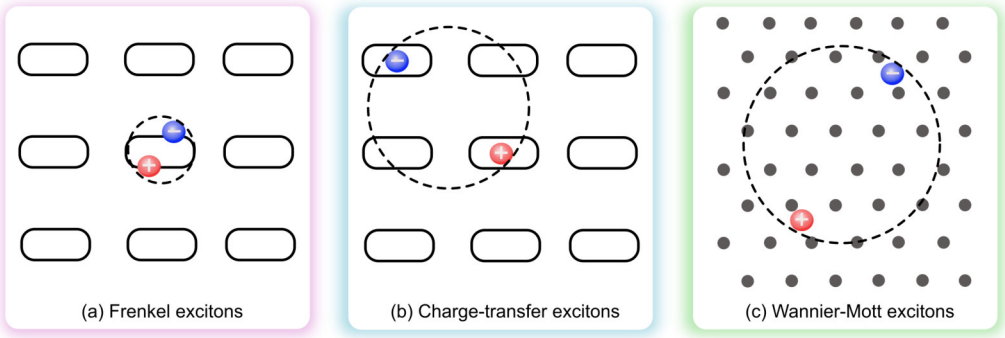

Figure 2.11: Schematic of three types of excitons: (a) Frenkel exciton, (b) charge-transfer exciton and (c) Wannier-Mott exciton.

The charge-transfer excitons may occur in systems with an alternating structure of two types of molecules, but also in crystals with just one type of molecule.[197]
In inorganic semiconductors, the lowest-lying electronic excitations are Wannier-Mott excitons. Due to the large dielectric screening in inorganic semiconductors, the electron-hole interaction is effectively screened by the dielectric environment, resulting in a delocalized exciton with a radius much larger than the lattice space (Figure 2.11). The corresponding binding energy is on the order of 0.1 eV, which is much smaller than those of their organic counterparts. But when the dimension of the inorganic semiconductor converts from 3D to 2D, the electronic Coulomb screening is dramatically reduced. As a consequence, the dielectric constant ϵ can fall to 1 from $\epsilon \gg 1$ in conventional bulk materials. The reduced dielectric screening further enhances exciton binding energy in 2D materials. Generally, the binding energies of the strongly bound excitons in atomically thin 2D materials are on the order of 0.1~1.0 eV.[198] For example, the excitonic binding energy of the 2H-MoS_2 monolayer is up to 0.57 eV.[35]
When the dimension of a material degrades from bulk to 2D, the types of excitons experience a boom. As shown in Figure 2.12, the different types of excitons can be observed in the low-dimensional materials. Neutral excitons can be bright or dark.[199, 200] A bright exciton forms when a single photon is absorbed. Concerning dark excitons, the electron and hole are connected by an optically forbidden transition, namely spin-forbidden or momentum-forbidden states. This suggests that the electron does not reach the conduction band through photon absorption alone and it also needed phonon scattering. Therefore, the dark excitons have relatively long radiative lifetimes. When an electron or a hole is bound to a neutral exciton, trions can be formed, which are also called charged excitons.[40, 200] Since the trion is the three-particle bound state, it has an extra charge and nonzero spin, which has been of strong interest especially in the field of spin manipulation. After photo-excitation of the heterostructure (possess a type-II band alignment), holes or electrons can tunnel to the other layer forming interlayer excitons. A typical example is the TMDCs vdW heterostructure, such as WS_2/WSe_2,[201,

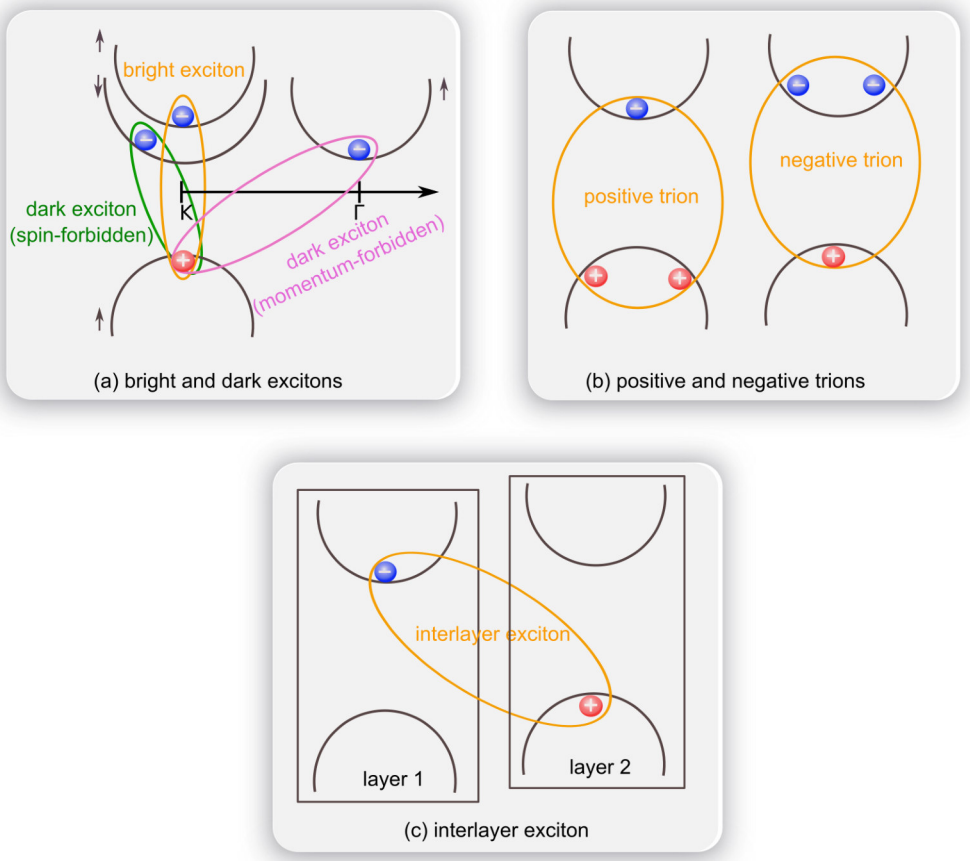

Figure 2.12: Schematic of different types of excitons in the low-dimensional materials: (a) bright and dark excitons, (b) positive and negative trions and (c) interlayer exciton. In dark excitons with spin-forbidden state, electron and hole have opposite spin; with momentum-forbidden state, electron and hole are located at different valleys in the momentum space.

202] $MoS_2/MoSe_2$,[203, 204] MoS_2/WS_2,[205, 206] MoS_2/WSe_2 [207, 208]with the binding energy of interlayer excitons ranging from ~0.1 to ~1.6 eV.[209] In addition to above-mentioned intralayer excitons in bilayer, interlayer excitons can also be form in three or few-layer 2D materials, such as $MoS_2/MoSe_2/MoS_2$.[210]

3 Results

[M1] **Influence of surface and subsurface Co–Ir alloy on the electronic properties of graphene.**
K. Wang, T. Vincent, J. Bouhiron, J. B. Bouhiron, S. Pons, D. Roditchev, S. Simon, M. Fonin, B. Paulus, Y. Dedkov, S. Vlaic and E. Voloshina, *Carbon.* **2021**, *183*, 251–258.
DOI: doi.org/10.1016/j.carbon.2021.06.082

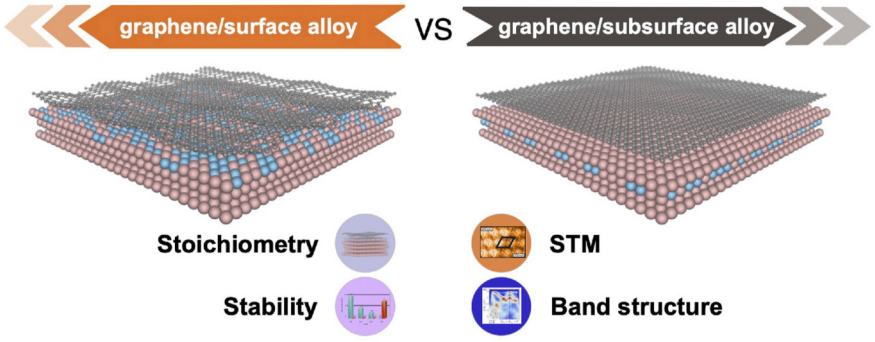

Graphical abstract of paper M1

Author contributions
The project was initially conceived by Elena Voloshina, Sergio Vlaic, and Yuriy Dedkov. Experiments were performed by Thomas Vincent, Jean Baptiste Bouhiron, Stephane Pons, Dimitri Roditchev, Sabina Simon, Mikhail Fonin; while myself performed the DFT calculations in close collaboration with Elena Voloshina and Beate Paulus. The manuscript was written by myself in collaboration with Sabina Simon, Elena Voloshina and Yuriy Dedkov.

[M2] **Electronic and optical properties of fluorinated graphene within many-body Green's function framework.**

K. Wang, J. Shao and B. Paulus, *J. Chem. Phys.* **2021**, *154*, 104705.

DOI: 10.1063/5.0042302

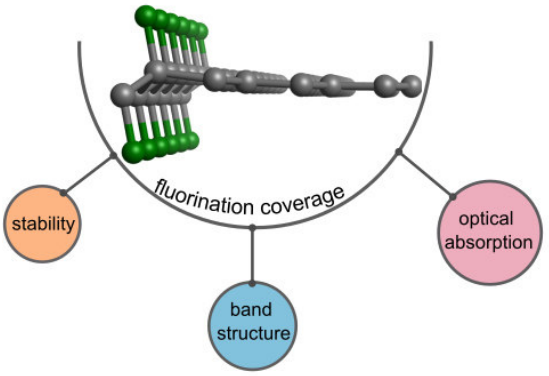

Graphical abstract of paper M2

Author contributions

The project was initially conceived by Beate Paulus and Jingjing Shao. All GW and BSE calculations presented in the manuscript were completed by myself. All figures of the structures and bandstructures were done by myself. The BSE figures were drawn by Jingjing Shao. The manuscript was written by Jingjing Shao in collaboration with Beate Paulus and with input from myself.

[M3] **Modulating electronic and optical properties of monolayered MoS_2 by covalent mono- and bisfunctionalization.**
K. Wang, M. Kapitzke, L. Green and B. Paulus, *submitted to J. Mater. Chem. C.*

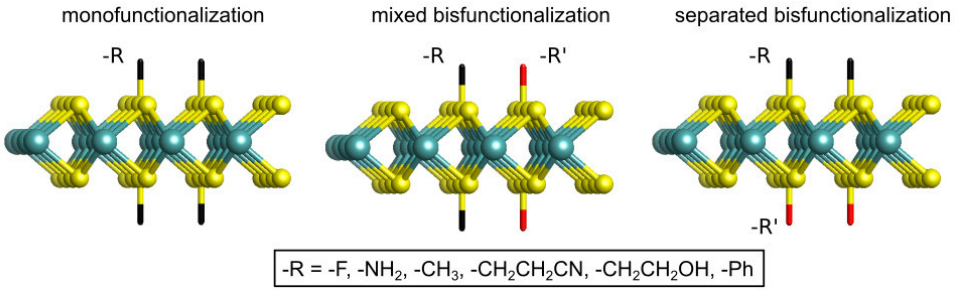

Graphical abstract of paper M3

Author contributions
The project was initially conceived by myself and Beate Paulus. Marco Kapitzke and Lauren Green performed initial test calculation at the DFT level and explored various possible groups for the project. All calculations contained in the manuscript were performed by myself. The manuscript was written by myself in collaboration with Beate Paulus, Marco Kapitzke and Lauren Green. Liangliang Zhang and Jianliang Low helped in proofreading the manuscript.

Journal Name

ARTICLE TYPE

Cite this: DOI: 00.0000/xxxxxxxxxx

Modulating Electronic and Optical Properties of Monolayered MoS_2 by Covalent Mono- and Bisfunctionalization†

Kangli Wang,* Marco Kapitzke, Lauren Green and Beate Paulus

Received Date
Accepted Date

DOI: 00.0000/xxxxxxxxxx

By employing first-principles simulations, we present theoretical predictions regarding the modification of structural, electronic and optical properties of 2H- and 1T'-MoS_2 monolayers by covalent mono- and bisfunctionalization. Specifically, non-aromatic groups (-F, -NH_2, -CH_3, -CH_2CH_2CN and -CH_2CH_2OH) and aromatic (-Ph, -$PhNO_2$ and PhOH) groups are utilized for monofunctionalization, and -F/-NH_2, -NH_2/-CH_3 and -CH_3/-Ph for bisfunctionalization. The stability of functionalized 2H- and 1T'-MoS_2 monolayers mainly depends on the bonded groups and their surface coverage. In particular, the mixed bisfunctionalization with -F/-CH_3 and -NH_2/-CH_3 groups enhances the stability of 2H-MoS_2 through the formation of intermolecular hydrogen bonds. Both 2H- and 1T'-MoS_2 can serve not only as electron donors, but also as electron acceptors, subject to the charge transfer behavior of the attached groups. Furthermore, mono- and bisfunctionalization are predicted to be efficient approaches to control the electronic band gaps in 2H- and 1T'-MoS_2, where the corresponding values can be tuned by varying the coverage of the absorbed groups. At the same time, the choice of the chemical groups and their coverage also effectively determines the optical adsorption range and intensity. Therefore, our work shows that chemical functionalization of 2D materials with varying coverage can be an important approach to extend the scope of 2D materials in specific electronic and optoelectronic applications.

1 Introduction

Monolayered MoS_2 is one of the most common transition metal dichalcogenides (TMDCs) and finds a range of promising applications such as photodetectors[1–3], advanced catalysts[4,5], gas sensors[6,7], batteries[8,9] and solar cells[10,11] due to its unique features and excellent tunability of the electronic properties. Depending on the arrangement of S atoms on both sides of Mo atoms, the MoS_2 monolayer has either of the three polytypic structures: the 2H, 1T and 1T' (distorted 1T) phases.[12–15] The Mo atom in the 2H and 1T phases is coordinated by six S atoms in an octahedral and trigonal prismatic arrangement, respectively. Generally, 1T phase is unstable under free-standing conditions and can be easily converted into the meta stable 1T' phase that consists of zigzag Mo chains. Owing to the different localization behaviors of the *d*-band in Mo,[16] 2H-MoS_2 is a semiconductor with a sizeable band gap and a photoluminophore, whereas 1T-MoS_2 exhibits metallic character without photoluminescence.[1,2,14–16] Interestingly, the 1T and 2H phases can also coexist in the same MoS_2 monolayer,[17] thereby allowing low contact resistance and holding high catalytic activity.[18,19]

To further improve the applicability of TMDCs in diverse fields, many methods have been developed to tune their properties, such as adsorption of gas molecules[20–22] and strain engineering[23,24]. Among them, covalent functionalization offers the most compelling route. Since the basal plane of 1T-MoS_2 is sensitive to functionalization, chemically exfoliated MoS_2 can react with phenyl diazonium salts[25,26] or organohalides (-I or -Br)[27,28] to form new S-Mo bonds. Although 2H-MoS_2 has a relatively inert basal plane, it is reported to be covalently functionalized by bonding through sulfur defects,[29–31] coordinating to metal complexes,[32] reacting with aryl diazonium[33] and thiolate salts[34] as well as maleimide derivatives.[35] More impressively, a bisfunctionalized MoS_2 hybrid structure bearing both alkyl and aryl groups has been recently demonstrated.[36] On the other hand, the coverage of functional groups achieved after functionalization varies from 10% to 70%, depending on different methods and conditions.[25,27,33,36,37] Given these experimental results, a theoretical perspective on how covalent functionalization alters the electronic and optical properties of 2H- and 1T-MoS_2 (or 1T'-MoS_2) is desirable. However, previous computational studies mainly focus on the monofunctionalization with small groups (-H, -O, -SH, -NH_2, -CH_3),[38–41] while monofunctionalization with large groups

Institut für Chemie und Biochemie, Freie Universität Berlin, 14195 Berlin, Germany; E-mail: klwang0329@zedat.fu-berlin.de

† Electronic Supplementary Information (ESI) available. See DOI: 00.0000/000.

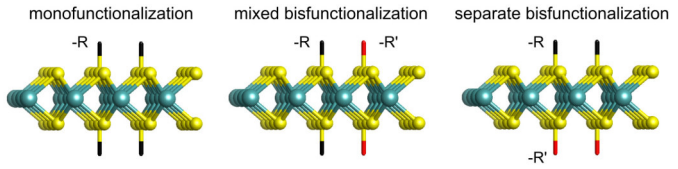

Fig. 1 Schematic representation of mono- and bisfunctionalization considered in this work.

as well as bisfunctionalization is far less explored.[42,43]

In this work, we aim to give a comprehensive understanding towards the two-sided covalent functionalization of monolayered 2H- and 1T'-MoS_2. We do not consider the functionalized T phase as this structure evolves to the T' phase upon structural optimization. Non-aromatic groups (-F, -NH_2, -CH_3, -CH_2CH_2CN and -CH_2CH_2OH) and aromatic groups (-Ph, -$PhNO_2$ and PhOH) are applied to monofunctionalize 2H- and 1T'-MoS_2. Furthermore, bisfunctionalization of MoS_2 is also considered in this study, including mixed bisfunctionalization (m-F/-NH_2, m-NH_2/-CH_3 and m-CH_3/-Ph) where each group is bonded to both sides of the MoS_2 monolayer and separate bisfunctionalization (s-F/-NH_2, s-NH_2/-CH_3 and s-CH_3/-Ph) where each side of the monolayer is uniquely functionalized by a specie as illustrated in Fig. 1. It is well known that density functional theory (DFT) alone is ill-equipped to describe the electronic band structure, especially when predicting the size of the band gap for semiconductors or insulators. To accurately model the electronic band structure and optical absorption, we employ the GW (Green's function (G) and screened Coulomb (W) potential) approximation within the framework of many-body perturbation theory and Bethe-Salpeter equation based on the DFT method (DFT-GW-BSE)[44–47]. This method includes self-energy and excitonic effects, and thus has been successfully applied to a wide variety of materials.[48–51]

2 Computational details

All of the calculations are performed with the GPAW code[52]. The structure is relaxed until all forces are below 0.01 eV/Å using the Perdew-Burke-Ernzerhof (PBE) exchange-correlation functional[53] with 450 eV plane wave cutoff, and more than 15 Å between periodically repeated layers. A 4×4 supercell (contains 32 adsorption sites) is considered to bond with 2, 4, ... , 14 groups corresponding to the functionalized coverages varying from 6.25% to 43.75%; a 2×2 supercell with 2 groups corresponds to a 50% coverage. A Γ-centered Monkhorst-Pack k-grid scheme of 6×6×1 and 12×12×1 are used for 4×4 and 2×2 supercells, respectively. The charge transfer between the group and the substrate is discussed by means of Bader analysis.[54]

The DFT-GW-BSE calculations are performed according to following protocol. Firstly, standard Kohn-Sham DFT calculations are performed to obtain the ground state Kohn-Sham orbitals. The same parameters as for the structural relaxation calculations are adopted. Then, non-self-consistent G_0W_0 is employed to calculate the quasiparticle (QP) band structures, which involves the calculation of QP energy using the input DFT orbitals. To avoid spurious interactions between neighboring supercells, a 2D Coulomb truncation is applied with 8 Å vacuum ensuring the convergence of the QP band gap. The dielectric matrix and correlation self-energy is evaluated using a cutoff of 50 eV on a nonlinear grid with $\Delta\omega_0 = 0.25$ eV frequency spacing. At $\omega_2 = 10$ eV, this spacing increases to $2\Delta\omega_0$. Finally, the BSE spectrum is obtained by applying the Tamm-Dancoff approximation.[55,56] The 24 highest valence and 48 lowest conduction bands are utilized as a basis for excitonic eigenstates, which is enough to attain converged optical absorption spectrum. A Lorentzian broadening of 0.05 eV is employed for all the optical calculations. The convergence tests for the DFT-GW-BSE treatment are in Supporting Information (see Fig. S1).

3 Results and discussion

Average binding energy. We first employ DFT to determine the most favorable adsorption sites and calculate the thermodynamic stability of the functionalized MoS_2 monolayer by computing the average binding energy per group as a function of the adsorbate coverages:

$$\Delta E = (E_{\text{tot}} - E_{\text{MoS}_2} - nE_{\text{group}})/n, \quad (1)$$

where E_{tot} is the total energy of functionalized MoS_2, E_{MoS_2} is the energy of the pristine 2H- or 1T'-MoS_2 monolayer, E_{group} is the energy of the isolated group and n is the number of groups that are added. A more negative binding energy indicates a stronger preference of the structure, while a positive value of the binding energy implies an unstable structure. The optimized structures for monofunctionalized MoS_2 at 6.25% coverage and bisfunctionalized MoS_2 at 12.5% coverage are presented in Fig. 2. The obtained average binding energies as a function of coverages are plotted in Fig. 3. As depicted in Fig. 3(a) and (c), at low coverage up to 25%, the average binding energy of each group on the functionalized 2H-MoS_2 system slightly decrease with the increase of coverage for most of the studied functionalizations. This indicates that the adsorbed group can act as an anchor, boosting further functionalization of 2H-MoS_2. When the coverage exceeds 25%, the computed binding energies of all systems become more positive as the coverage grows, suggesting that high coverage of 2H-MoS_2 is unfavorable due to the repulsive interaction between the adsorbed species. At high coverage, the 2H phase functionalized by -NH_2 and s-NH_3/-CH_3 tends to release NH_3 gas and therefore a stable covalent functionalization of 2H phase is not possible. However, mixed bisfunctionalization can promote the formation of intermolecular hydrogen bonds and thereby improves their stability as the coverage increases, such as m-F/-CH_3 and m-NH_2/-CH_3. In comparison to other groups, the average binding energy of -CH_2CH_2CN and -CH_2CH_2OH on the basal surface of 2H-MoS_2 is rather more positive and the Mo-C bond length is more than 1.91 Å. This is attributed to the stereostructures of -CH_2CH_2CN and -CH_2CH_2OH that weaken the interaction between the chemical adsorbate and 2H-MoS_2.

Fig. 3(b) and (d) illustrate the average binding energy of the functionalized 1T'-MoS_2 at varying coverage. For the 1T' phase, the average binding energy of each system reaches a minimum at 12.5% coverage, which is smaller than that of 2H-MoS_2. Furthermore, a considerable stability range of the functionalized 1T'

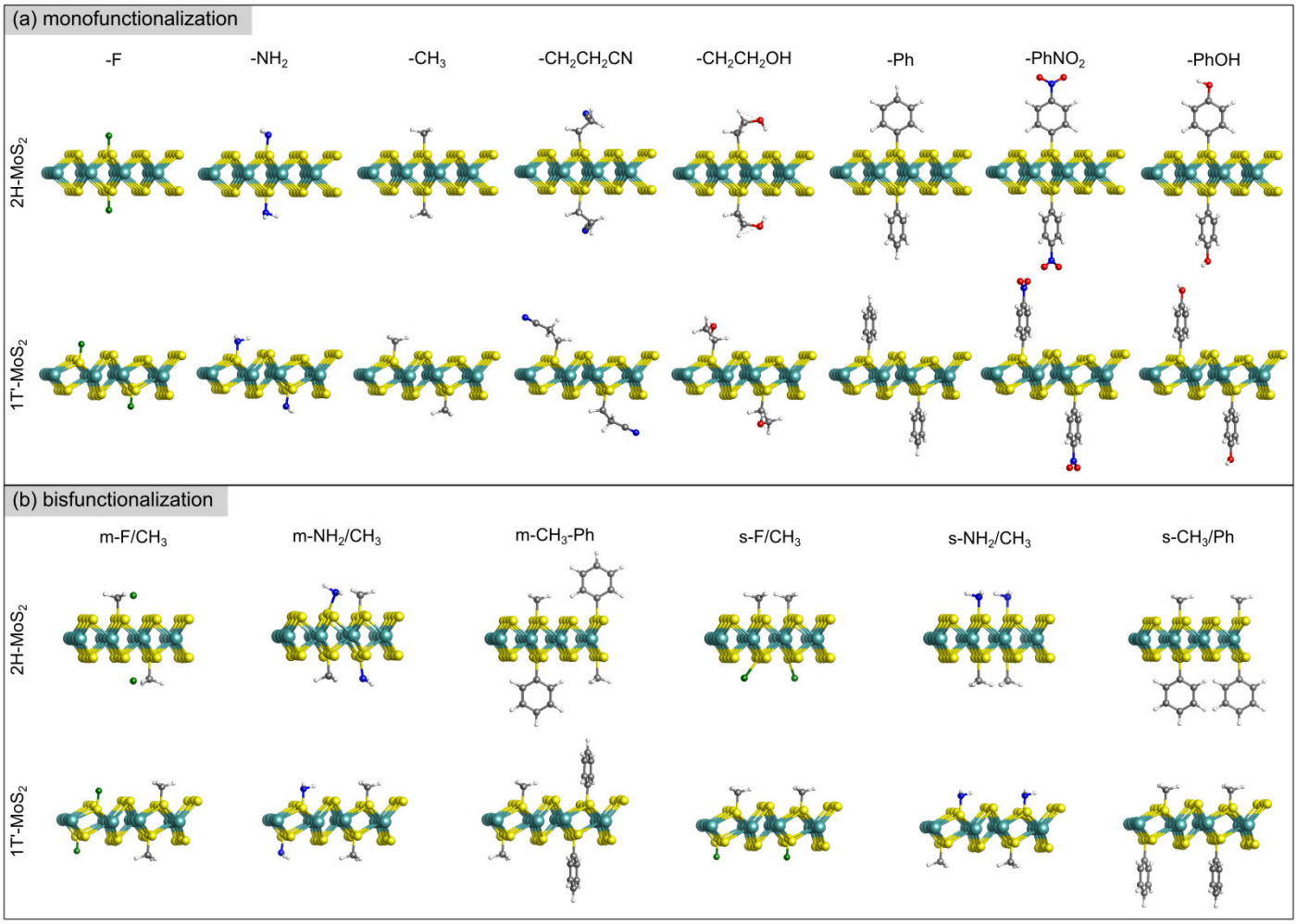

Fig. 2 Ball-and-stick model of the optimized structures of the monofunctionalized (6.25% coverage) and bisfunctionalized (12.5% coverage) 2H- and 1T'-MoS_2 by different groups (side and perspective views). The hydrogen, carbon, nitrogen, oxygen, fluorine, sulfur and molybdenum are in color white, gray, blue, red, green, yellow and turquoise, respectively.

phase can be noticed, exhibiting a negative average binding energy even at 50% coverage. This suggests the possibility of high functional group coverage of functionalized 1T'-MoS_2, which is consistent with previous experimental observations.[37] In addition, the average binding energy of 1T'-MoS_2 is much smaller than that of 2H-MoS_2 for any given coverage, indicating that the reaction of chemical functionalization of the 1T' phase is thermodynamically more favorable. This is attributed to the well-paired electrons in 2H-MoS_2, whereas the electronic states around the Fermi level are only partially filled in 1T'-MoS_2.[39]

By comparing the total energy between 2H- and 1T'-MoS_2, we investigate the phase stability (see Fig. S3). At low coverage, the functionalized 2H phase is more energetically stable regardless of mono- or bisfunctionalization. As the coverage increases, the energy difference becomes smaller. In particular, at high coverage, the functionalized 1T' phase is more stable than 2H case. This indicates that the selective tuning of the coverage of covalent functionalization enables the phase transformation of MoS_2.

To gain an insight into the bonding nature of the considered systems, we further execute the Bader charge analysis to investigate the charge transfer between the MoS_2 monolayer and the attached groups. The corresponding results are displayed in Fig. S4. When -F, -NH_2, m-F/-CH_3 and s-F/-CH_3 are bonded to the surface of both 2H- and 1T'-MoS_2, the electron is transferred to the groups from the substrate which acts as an electron-donor. In contrast, an inverted electron flow can be recognized for other functional groups, for instance -CH_3, -CH_2CH_2CN, -CH_2CH_2OH, -Ph, -$PhNO_2$ and -PhOH. Here the substrate gains electrons despite bare MoS_2 is an n-type semiconductor. The direction of charge transfer exhibits a clear dependence on the electron donating or withdrawing ability of the adsorbed species. Correlation of the binding energy with the electron donating or withdrawing properties of the functional group shows that when the 2H- or 1T'-MoS_2 serves as an electron-donor, the average binding energy becomes more negative for strongly electron-withdrawing groups (-F vs -NH_2). It implies that the stronger electron-withdrawing effect could enhance the stability of the functionalized MoS_2 monolayer in this case. On the other hand, the attached groups with a stronger electron donating-ability show more negative binding energies, advocating that MoS_2 monolayers are more stable un-

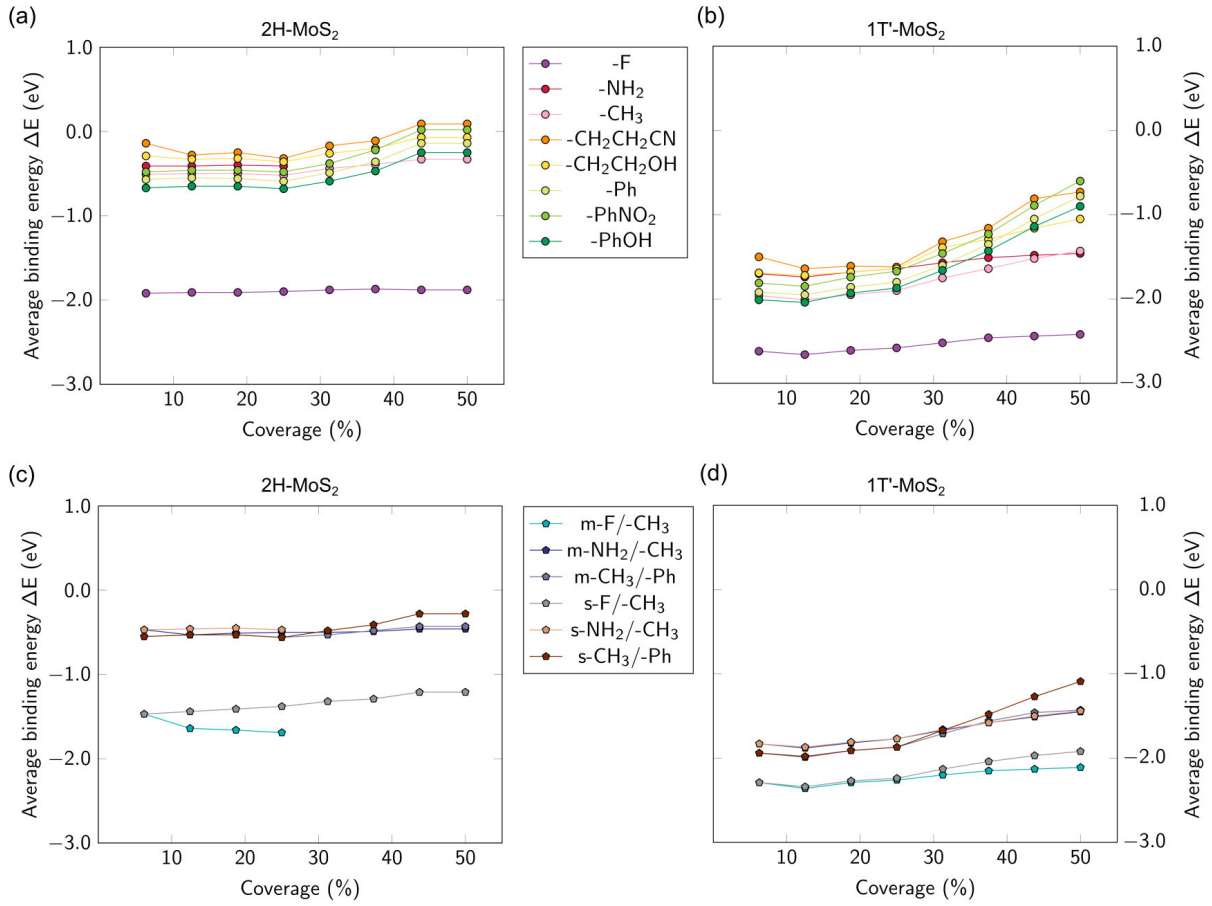

Fig. 3 Average binding energy as a function of the group coverage with respect to the 2H-MoS_2 and 1T'-MoS_2 monolayers.

der this condition. Examples include the monofunctionalization with -CH_2CH_2OH vs -CH_2CH_2CN or -PhOH vs -$PhNO_2$.

For bisfunctionalized 2H- and 1T'-MoS_2, the average binding energy can be compared to that of the corresponding monofunctionalized case. In particular, when -F and -CH_3 are functionalized separately on both sides of 2H-MoS_2, the average binding energy is more negative than the average between the two corresponding monofunctionalized 2H-MoS_2. This is because the cooperative effect of electron withdrawing and donating groups could promote the charge transfer and consequently enhances its stability. Intriguingly, the average binding energy for the 1T'-MoS_2 in the case is almost equal to the monofunctionalized ones. This is attributed to the distorted octahedral structure and non-equivalent S atoms of 1T'-MoS_2, which attenuates this cooperative effect. Concerning the mixed bisfunctionalization with -F and -CH_3, this combined effect is offset for both 2H- and 1T'-MoS_2. As for the bisfunctionaliation of -CH_3 and -Ph including the separate and mixed functionalization, the average binding energy is also close to average between the two corresponding monofunctionalized MoS_2 because both of these two groups tend to donate electrons to the substrate. In summary, the investigation of the average binding energy reveals that the coverage, stereostructure and electron doping of the groups drive the stability of both functionalized 2H- and 1T'-MoS_2 monolayers.

Electronic properties. To provide a benchmark for our computational scheme, we initially apply the DFT-GW-BSE method to the bare MoS_2 monolayer. The calculated electronic band gaps with the DFT method at PBE level are 1.65 eV and 0.04 eV for 2H- and 1T'-MoS_2, respectively, whereas the self-energy correction considered in G_0W_0 method opens the band gaps to 2.51 eV and 0.08 eV, respectively. The G_0W_0 results are consistent with reported experimental values of 2.50 eV and 0.08 eV for 2H-MoS_2 and 1T'-MoS_2, respectively.[57,58] Next, we turn our attention to the functionalized 2H- and 1T'-MoS_2 monolayers. Fig. 4 depicts the variation of the electronic band gaps calculated by the G_0W_0 method with different adsorbates and coverages. The corresponding DFT results are presented in Fig. S5. At 6.25% coverage, the monofunctionalized and bisfunctionalized 2H-MoS_2 display semiconducting characteristics with varying QP band gaps from 0.99 eV to 2.22 eV for the considered systems. The reduced band gap is associated with the donor or acceptor state inside the gap of bare 2H-MoS_2 (see Fig. S6). The introduced state primarily originates from the Mo 4*d* band with additional contributions from the 3*p* orbitals of S and the *sp* orbitals of the adsorbate. This suggests that the 4*d* of Mo atoms will make a main contribution to the electronic transport in all cases although groups bind directly to the S atoms of MoS_2. As adsorbate coverage increases from 12.5% to 25%, the band gap tends to decrease. At even higher coverage (31.25%-50%), the band gap fluctuates, except in the case of -NH_2/CH_3 and -F/CH_3. We note that the band gaps of both

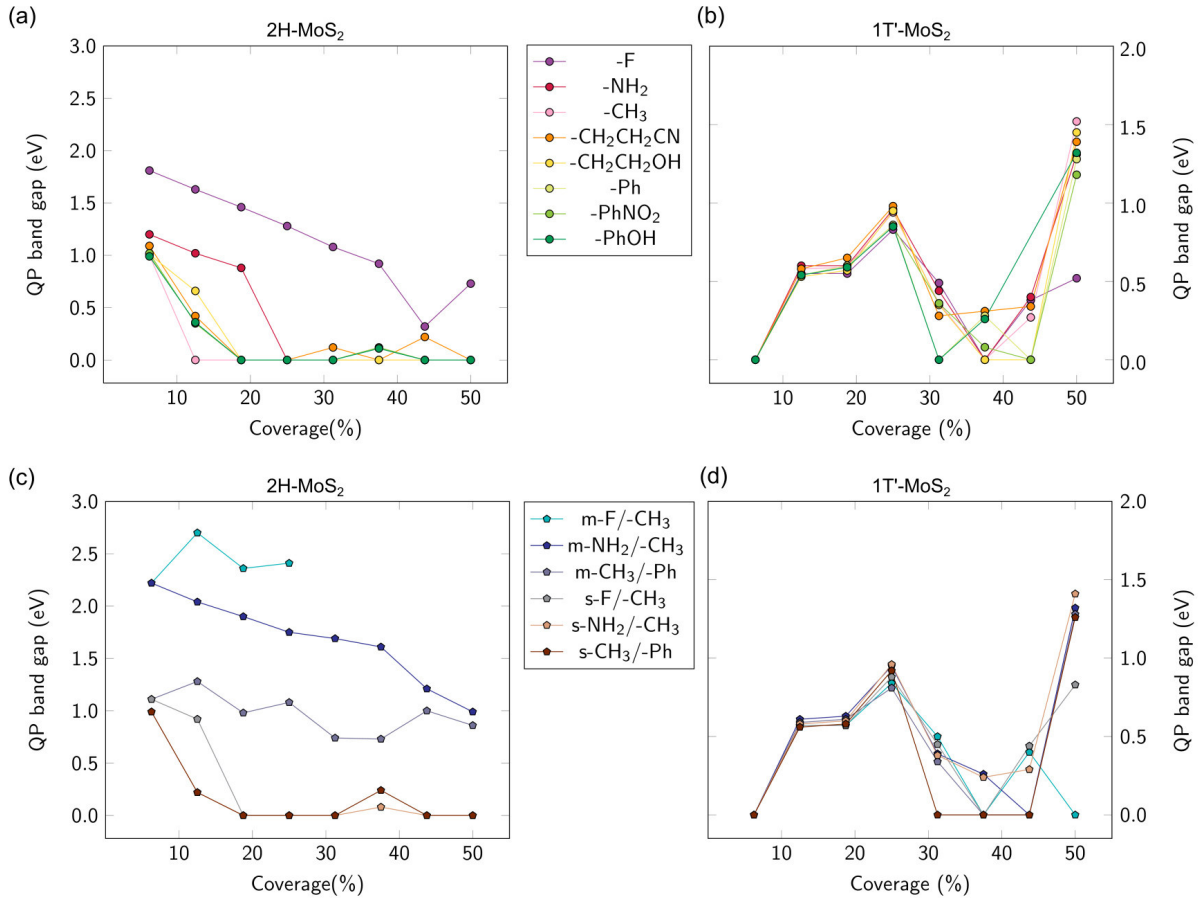

Fig. 4 QP band gaps as a function of the group coverages with respect to the functionalized 2H-MoS_2 and 1T'-MoS_2 monolayers.

mono- and bisfunctionaliation are highly sensitive to the adsorption site, which is also found in other materials.[59–61] Therefore, the modification of the band gap for mixed bisfunctionalization of -NH_2/-CH_3 and -F/-CH_3 differs due to the difference in adsorption sites which arises from the intermolecular hydrogen bonds. With respect to the introduced donor or acceptor state around the Fermi level, the contribution of both S 3*p* and adsorbate *sp* states increases with the increase of coverage for both mono- and bisfunctionalization, implying the influence of group coverage on electronic transport (Fig. S6).

Compared with the 2H phase, the 1T'-MoS_2 exhibits different behaviors after covalent functionalization. It is obvious from Fig. 4 that at 6.25% coverage, both mono- and bisfunctionalized 1T'-MoS_2 exhibit metallic character, in contrast to 2H-MoS_2. As the coverage increases, the QP band gaps first increase and then oscillate at high coverage. Furthermore, the variation of QP band gaps of m-NH_2/-CH_3 and m-F/-CH_3 displays a similar trend as that of monofunctionalized 1T'-MoS_2. This is caused by the distorted structure of the 1T' phase, which inhibits the formation of intermolecular hydrogen bonds and thereby enables the mixed groups to adsorb at the same or similar site with that of monofunctionalization. This also means the interaction between the adsorbate and the substrate in case of bisfunctionalized 1T'-MoS_2 is strong. Overall, our calculations reveal that the variation in the band gaps of both 2H- and 1T'-MoS_2 provides promising results of the utility of the chemical mono-/bisfunctionalization and coverages to tune the electronic properties of 2D materials.

Optical properties. Next, we examine the optical properties of the functionalized 2H- and 1T'-MoS_2, which are crucial for MoS_2-based optoelectronic devices. As a result of the low stability at high coverage, only low group coverages are considered. The corresponding optical absorption spectra of 2H phase are presented in Fig. 5. Compared to bare 2H-MoS_2, the optical absorption upon mono- and bisfunctionalization is red-shifted at 6.25% coverage. The red-shift is attributed to the interplay of two joint effects: (1) the reduced electronic band gap upon functionaliation as we discussed above and (2) the variation of the exciton binding energy (see Table S1). Our calculation shows that at 6.25% coverage, monofunctionalition with each group and bisfunctionalization with -NH_2/-CH_3 lowers the excitonic binding energy slightly; whereas the bisfunctionaliation with -F/-CH_3 or -CH_3/-Ph tends to strengthen the Coulomb interaction between the electron and hole of an exciton, promoting the formation of tight excitonic states. As the reduction of the electronic band gap is dominant upon functionalization, the optical spectrum is strongly red-shifted and the absorbance is enhanced in the 0−2 eV regime. It is worth mentioning that the optical band gap varies significantly from 0.18 eV to 1.49 eV at 6.25% coverage, indicating the high sensitivity of optical properties of 2H phase towards the different groups. As coverage increases to 18.75%, the overall

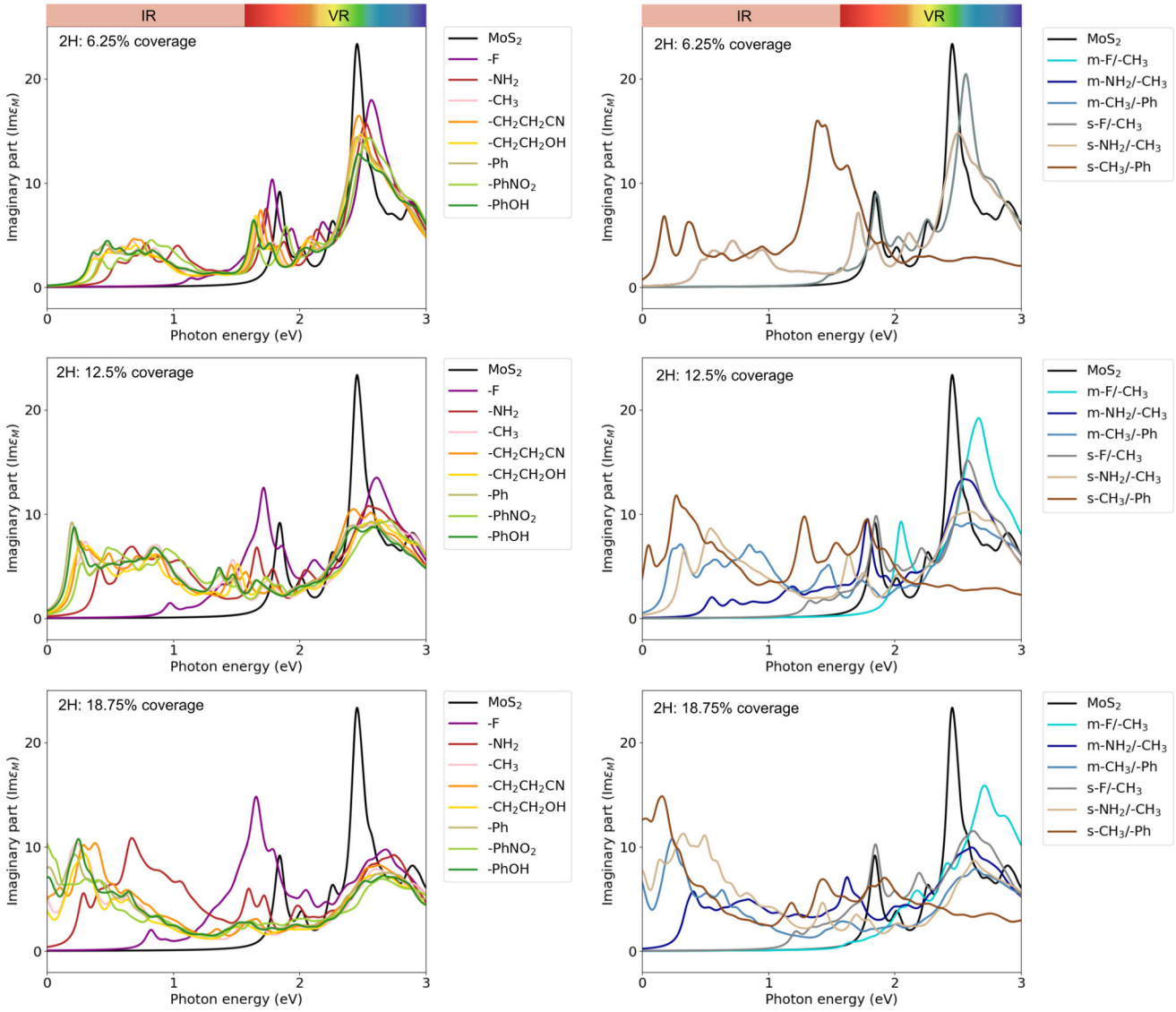

Fig. 5 Optical absorption spectra of the functionalized 2H-MoS_2 monolayer.

optical absorbance for each functionalization remains red-shifted with a reduced optical band gap. At the same time, the intensity of the optical absorption is remarkably enhanced, especially in the spectral range of 0−1 eV.

In the case of 1T'-MoS_2, we observe an obvious blue-shift of the optical spectrum and an increase in optical absorption as the coverage increases from 6.25% to 18.75% (see Fig. S7), which can be explained by the opening of the electronic band gap of 1T'-MoS_2 upon functionalization. Our study regarding the optical properties of the functionalized MoS_2 offers the prospect of artificially tuning the optical properties of MoS_2 by controlling the type and coverage of the functional groups.

4 Conclusion

In this work, we systemically study the stability, electronic band gap and optical absorption spectrum of both chemically functionalized 2H- and 1T'-MoS_2 for various adsorbates by means of the DFT-GW-BSE method. The chemical groups studied include -F, -NH_2, -CH_3, -CH_2CH_2CN, -CH_2CH_2OH, -Ph, -$PhNO_2$ and PhOH for monofunctionalization and m-F-CH_3, m-NH_2-CH_3, m-CH_3-Ph, s-F-CH_3, s-NH_2-CH_3 and s-CH_3-Ph for bisfunctionalization. We find when no intermolecular interaction is observed, the average binding energy falls at first and rises again as the coverage is elevated, reaching a minimum at 25% and 12.5% for 2H and 1T'-MoS_2, respectively. The bisfunctionalization of m-F-CH_3 and m-NH_2-CH_3 on 2H-MoS_2 can promote the formation of intermolecular hydrogen bonds and thus improve the stability. When -F, -NH_2, m-F/-CH_3 and s-F/-CH_3 are attached on the surface, both of 2H- and 1T'-MoS_2 serve as electron-donors; in other cases, both of 2H- and 1T'-MoS_2 act as electron acceptors. At low coverage, the functionalized 2H-MoS_2 generally exhibits semiconducting character, whereas the functionalized 1T'-MoS_2 is predicted to be metallic; as the coverage increases, the variation of band gaps of both 2H- and 1T'-MoS_2 shows an oscillatory behavior. The changes in the electronic structure as well as the excitonic binding energy of the functionalized 2H- and 1T'-MoS_2 lead to strong modulations of

their optical response with respect to the bare monolayers. In conclusion, our work demonstrates that mono- and bisfunctionalization of 2H- and 1T'-MoS_2 are vigorous tools for tuning the electronic and optical properties.

Conflicts of interest

The authors declare no conflicts of interest.

Acknowledgements

K. Wang acknowledges the China Scholarship Council for the financial support. The computations were performed with resources provided by the North-German Supercomputing Alliance (HLRN) and computer facilities of the Freie Universität Berlin (ZEDAT). Authors are also thankful to Liangliang Zhang and Jianliang Low for their assistance in the proofreading of the manuscript.

Notes and references

1 Z. Yin, H. Li, H. Li, L. Jiang, Y. Shi, Y. Sun, G. Lu, Q. Zhang, X. Chen and H. Zhang, *ACS Nano*, 2012, **6**, 74–80.

2 W. Zhang, C.-P. Chuu, J.-K. Huang, C.-H. Chen, M.-L. Tsai, Y.-H. Chang, C.-T. Liang, Y.-Z. Chen, Y.-L. Chueh, J. He-Hau, M.-Y. Chou and L.-J. Li, *Sci. Rep.*, 2014, **4**, 3826.

3 Y. Xin, X. Wang, Z. Chen, D. Weller, Y. Wang, L. Shi, X. Ma, C. Ding, W. Li, S. Guo and R. Liu, *ACS Appl. Mater. Interfaces*, 2020, **12**, 15406–15413.

4 Y. Li, H. Wang, L. Xie, Y. Liang, G. Hong and H. Dai, *J. Am. Chem. Soc.*, 2011, **133**, 7296–7299.

5 G. Li, Z. Chen, Y. Li, D. Zhang, W. Yang, Y. Liu and L. Cao, *ACS Nano*, 2020, **14**, 1707–1714.

6 H. Tabata, H. Matsuyama, T. Goto, O. Kubo and M. Katayama, *ACS Nano*, 2021, **15**, 2542–2553.

7 B. Zong, Q. Li, X. Chen, C. Liu, L. Li, J. Ruan and S. Mao, *ACS Appl. Mater. Interfaces*, 2020, **12**, 50610–50618.

8 K. Chang and W. Chen, *ACS Nano*, 2011, **5**, 4720–4728.

9 J. Xiao, D. Choi, L. Cosimbescu, P. Koech, J. Liu and J. P. Lemmon, *Chem. Mater.*, 2010, **22**, 4522–4524.

10 G. Eda and S. A. Maier, *ACS Nano*, 2013, **7**, 5660–5665.

11 M.-L. Tsai, S.-H. Su, J.-K. Chang, D.-S. Tsai, C.-H. Chen, C.-I. Wu, L.-J. Li, L.-J. Chen and J.-H. He, *ACS Nano*, 2014, **8**, 8317–8322.

12 F. Wypych and R. Schöllhorn, *J. Chem. Soc., Chem. Commun.*, 1992, 1386–1388.

13 J. A. Wilson and A. D. Yoffe, *Adv. Phys.*, 1969, **18**, 193–335.

14 I. Song, C. Park and H. C. Choi, *RSC Adv.*, 2015, **5**, 7495–7514.

15 X. Qian, J. Liu, L. Fu and J. Li, *Science*, 2014, **346**, 1344–1347.

16 R. Bissessur, M. G. Kanatzidis, J. L. Schindler and C. R. Kannewurf, *J. Chem. Soc., Chem. Commun.*, 1993, 1582–1585.

17 G. Eda, T. Fujita, H. Yamaguchi, D. Voiry, M. Chen and M. Chhowalla, *ACS Nano*, 2012, **6**, 7311–7317.

18 R. Kappera, D. Voiry, S. E. Yalcin, B. Branch, G. Gupta, A. Mohite and M. Chhowalla, *Nature materials*, 2014, **13**, 1128–1134.

19 Y. Yao, K. Ao, P. Lv and Q. Wei, *Nanomaterials*, 2019, **9**, 844.

20 T. Venanzi, H. Arora, A. Erbe, A. Pashkin, S. Winnerl, M. Helm and H. Schneider, *Appl. Phys. Lett.*, 2019, **114**, 172106.

21 K. Wang and B. Paulus, *Phys. Chem. Chem. Phys.*, 2020, **22**, 11936–11942.

22 S. Mouri, Y. Miyauchi and K. Matsuda, *Nano Lett.*, 2013, **13**, 5944–5948.

23 P. Gant, P. Huang, D. Pérez de Lara, D. Guo, R. Frisenda and A. Castellanos-Gomez, *Mater. Today*, 2019, **27**, 8–13.

24 S. Wang, M. S. Ukhtary and R. Saito, *Phys. Rev. Research*, 2020, **2**, 033340.

25 K. C. Knirsch, N. C. Berner, H. C. Nerl, C. S. Cucinotta, Z. Gholamvand, N. McEvoy, Z. Wang, I. Abramovic, P. Vecera, M. Halik, S. Sanvito, G. S. Duesberg, V. Nicolosi, F. Hauke, A. Hirsch, J. N. Coleman and C. Backes, *ACS Nano*, 2015, **9**, 6018–6030.

26 E. E. Benson, H. Zhang, S. A. Schuman, S. U. Nanayakkara, N. D. Bronstein, S. Ferrere, J. L. Blackburn and E. M. Miller, *J. Am. Chem. Soc.*, 2018, **140**, 441–450.

27 D. Voiry, A. Goswami, R. Kappera, C. d. C. C. e Silva, D. Kaplan, T. Fujita, M. Chen, T. Asefa and M. Chhowalla, *Nat. Chem.*, 2015, **7**, 45–49.

28 X. Chen, D. McAteer, C. McGuinness, I. Godwin, J. N. Coleman and A. R. McDonald, *Chem. Eur. J.*, 2018, **24**, 351–355.

29 S. S. Chou, M. De, J. Kim, S. Byun, C. Dykstra, J. Yu, J. Huang and V. P. Dravid, *J. Am. Chem. Soc.*, 2013, **135**, 4584–4587.

30 Q. Ding, K. J. Czech, Y. Zhao, J. Zhai, R. J. Hamers, J. C. Wright and S. Jin, *ACS Appl. Mater. Interfaces*, 2017, **9**, 12734–12742.

31 S. Bertolazzi, S. Bonacchi, G. Nan, A. Pershin, D. Beljonne and P. Samorì, *Adv. Mater.*, 2017, **29**, 1606760.

32 C. Backes, N. C. Berner, X. Chen, P. Lafargue, P. LaPlace, M. Freeley, G. S. Duesberg, J. N. Coleman and A. R. McDonald, *Angew. Chem. Int. Ed.*, 2015, **54**, 2638–2642.

33 X. S. Chu, A. Yousaf, D. O. Li, A. A. Tang, A. Debnath, D. Ma, A. A. Green, E. J. G. Santos and Q. H. Wang, *Chem. Mater.*, 2018, **30**, 2112–2128.

34 I. K. Sideri, R. Arenal and N. Tagmatarchis, *ACS Mater. Lett.*, 2020, **2**, 832–837.

35 M. Vera-Hidalgo, E. Giovanelli, C. Navío and E. M. Pérez, *J. Am. Chem. Soc.*, 2019, **141**, 3767–3771.

36 X. Chen, C. Bartlam, V. Lloret, N. Moses Badlyan, S. Wolff, R. Gillen, T. Stimpel-Lindner, J. Maultzsch, G. S. Duesberg, K. C. Knirsch and A. Hirsch, *Angew. Chem. Int. Ed.*, 2021, **60**, 13484–13492.

37 E. X. Yan, M. Cabán-Acevedo, K. M. Papadantonakis, B. S. Brunschwig and N. S. Lewis, *ACS Mater. Lett.*, 2020, **2**, 133–139.

38 Q. Tang and D.-e. Jiang, *ACS Catal.*, 2016, **6**, 4953–4961.

39 Q. Tang and D.-e. Jiang, *Chem. Mater.*, 2015, **27**, 3743–3748.

40 M. Palummo, A. N. D'Auria, J. C. Grossman and G. Cicero, *J. Phys. Condens. Matter*, 2019, **31**, 235701.

41 Y. Linghu, N. Li, Y. Du and C. Wu, *Phys. Chem. Chem. Phys.*, 2019, **21**, 9391–9398.

42 A. Gul, C. Bacaksiz, E. Unsal, B. Akbali, A. Tomak, H. M. Zareie and H. Sahin, *Mater. Res. Express.*, 2018, **5**, 036415.

43 L. O. Jones, M. A. Mosquera, M. A. Ratner and G. C. Schatz, *ACS Appl. Mater. Interfaces*, 2020, **12**, 4607–4615.

44 M. S. Hybertsen and S. G. Louie, *Phys. Rev. B*, 1986, **34**, 5390–5413.

45 M. Rohlfing and S. G. Louie, *Phys. Rev. Lett.*, 1998, **81**, 2312–2315.

46 L. X. Benedict, E. L. Shirley and R. B. Bohn, *Phys. Rev. Lett.*, 1998, **80**, 4514–4517.

47 S. Albrecht, L. Reining, R. Del Sole and G. Onida, *Phys. Rev. Lett.*, 1998, **80**, 4510–4513.

48 D. Y. Qiu, F. H. da Jornada and S. G. Louie, *Phys. Rev. Lett.*, 2013, **111**, 216805.

49 L. Yang, J. Deslippe, C.-H. Park, M. L. Cohen and S. G. Louie, *Phys. Rev. Lett.*, 2009, **103**, 186802.

50 C. D. Spataru, S. Ismail-Beigi, L. X. Benedict and S. G. Louie, *Phys. Rev. Lett.*, 2004, **92**, 077402.

51 M. L. Tiago and J. R. Chelikowsky, *Solid State Commun.*, 2005, **136**, 333–337.

52 J. Enkovaara, C. Rostgaard, J. J. Mortensen, J. Chen, M. Dułak, L. Ferrighi, J. Gavnholt, C. Glinsvad, V. Haikola, H. A. Hansen, H. H. Kristoffersen, M. Kuisma, A. H. Larsen, L. Lehtovaara, M. Ljungberg, O. Lopez-Acevedo, P. G. Moses, J. Ojanen, T. Olsen, V. Petzold, N. A. Romero, J. Stausholm-Møller, M. Strange, G. A. Tritsaris, M. Vanin, M. Walter, B. Hammer, H. Häkkinen, G. K. H. Madsen, R. M. Nieminen, J. K. Nørskov, M. Puska, T. T. Rantala, J. Schiøtz, K. S. Thygesen and K. W. Jacobsen, *J. Phys. Condens. Matter*, 2010, **22**, 253202.

53 J. P. Perdew, K. Burke and M. Ernzerhof, *Phys. Rev. Lett.*, 1996, **77**, 3865–3868.

54 W. Tang, E. Sanville and G. Henkelman, *J. Phys. Condens. Matter*, 2009, **21**, 084204.

55 I. Tamm, *Selected Papers*, Springer, 1991, pp. 157–174.

56 S. M. Dancoff, *Phys. Rev.*, 1950, **78**, 382–385.

57 A. R. Klots, A. K. M. Newaz, B. Wang, D. Prasai, H. Krzyzanowska, J. Lin, D. Caudel, N. J. Ghimire, J. Yan, B. L. Ivanov, K. A. Velizhanin, A. Burger, D. G. Mandrus, N. H. Tolk, S. T. Pantelides and K. I. Bolotin, *Sci. Rep.*, 2014, **4**, 6608.

58 X. Yin, Q. Wang, L. Cao, C. S. Tang, X. Luo, Y. Zheng, L. M. Wong, S. J. Wang, S. Y. Quek, W. Zhang, A. Rusydi and A. T. S. Wee, *Nat. Commun.*, 2017, **8**, 486.

59 K. Wang, J. Shao and B. Paulus, *J. Chem. Phys.*, 2021, **154**, 104705.

60 R. Nechache, C. Harnagea, L. Cardenas, W. Huang, J. Chakrabartty and F. Rosei, *Nat. Photonics*, 2014, **advance online publication**,.

61 C. Shao, C. Rui, J. Liu, T. Wang, Q. Shao and F. Chen, *Diam. Relat. Mater.*, 2020, **106**, 107824.

Supporting Information (SI)

Modulating Electronic and Optical Properties of Monolayered MoS_2 by Covalent Mono- and Bisfunctionalization

Kangli Wang*, Marco Kapitzke, Lauren Green, and Beate Paulus

Institut für Chemie und Biochemie, Freie Universität Berlin, Arnimallee 22, 14195 Berlin, Germany

E-mail: klwang0329@zedat.fu-berlin.de

Content:

Fig. S1: (a) The QP band gaps of the functionalized 2H-MoS_2 with -CH_3 group as a function of vacuum thickness with 50 eV G_0W_0 self-energy and 12×12 k-point sampling (2×2 supercell). (b) The QP band gaps of the functionalized 2H-MoS_2 with -CH_3 group as a function of k-point sampling with 50 eV G_0W_0 self-energy and 8 Å vacuum thickness (2×2 supercell) . (c) Optical absorption spectra of the functionalized 2H-MoS_2 with -CH_3 group as a function of the number of valence and conduction bands with 50 eV self-energy and 8 Å vacuum thickness (2×2 supercell).

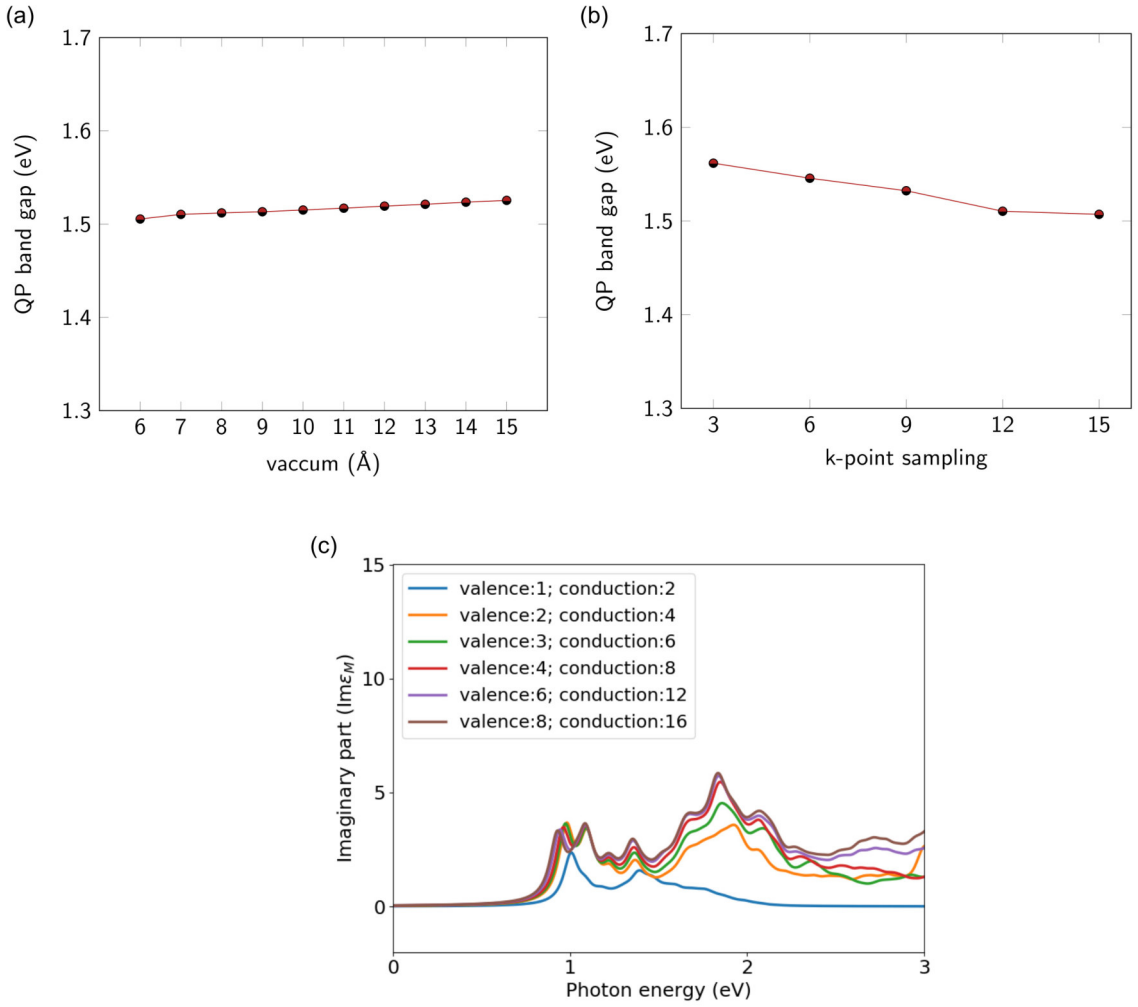

Fig. S2: Optimized structures of functionalized 2H-MoS_2 and 1T'-MoS_2 with various groups.

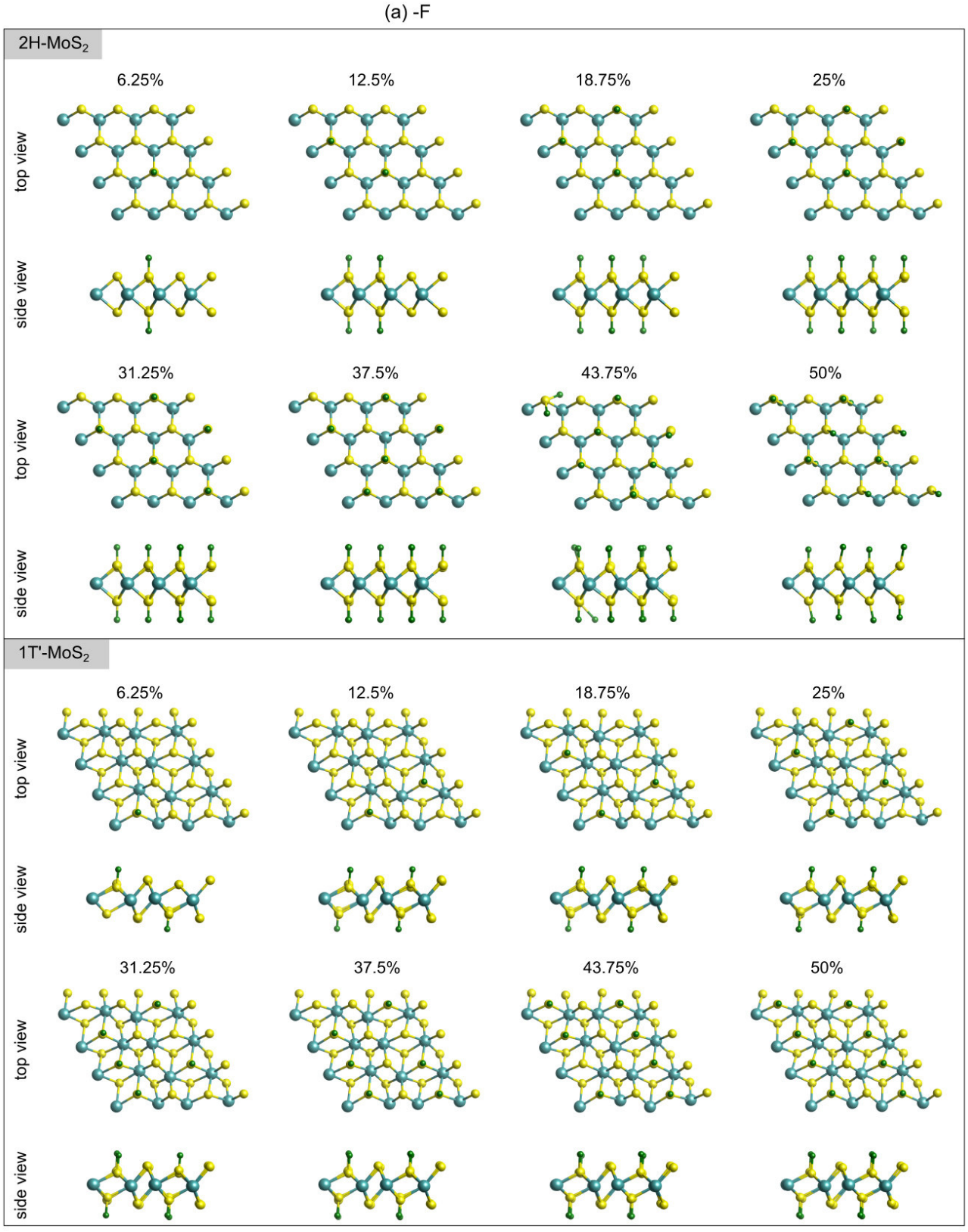

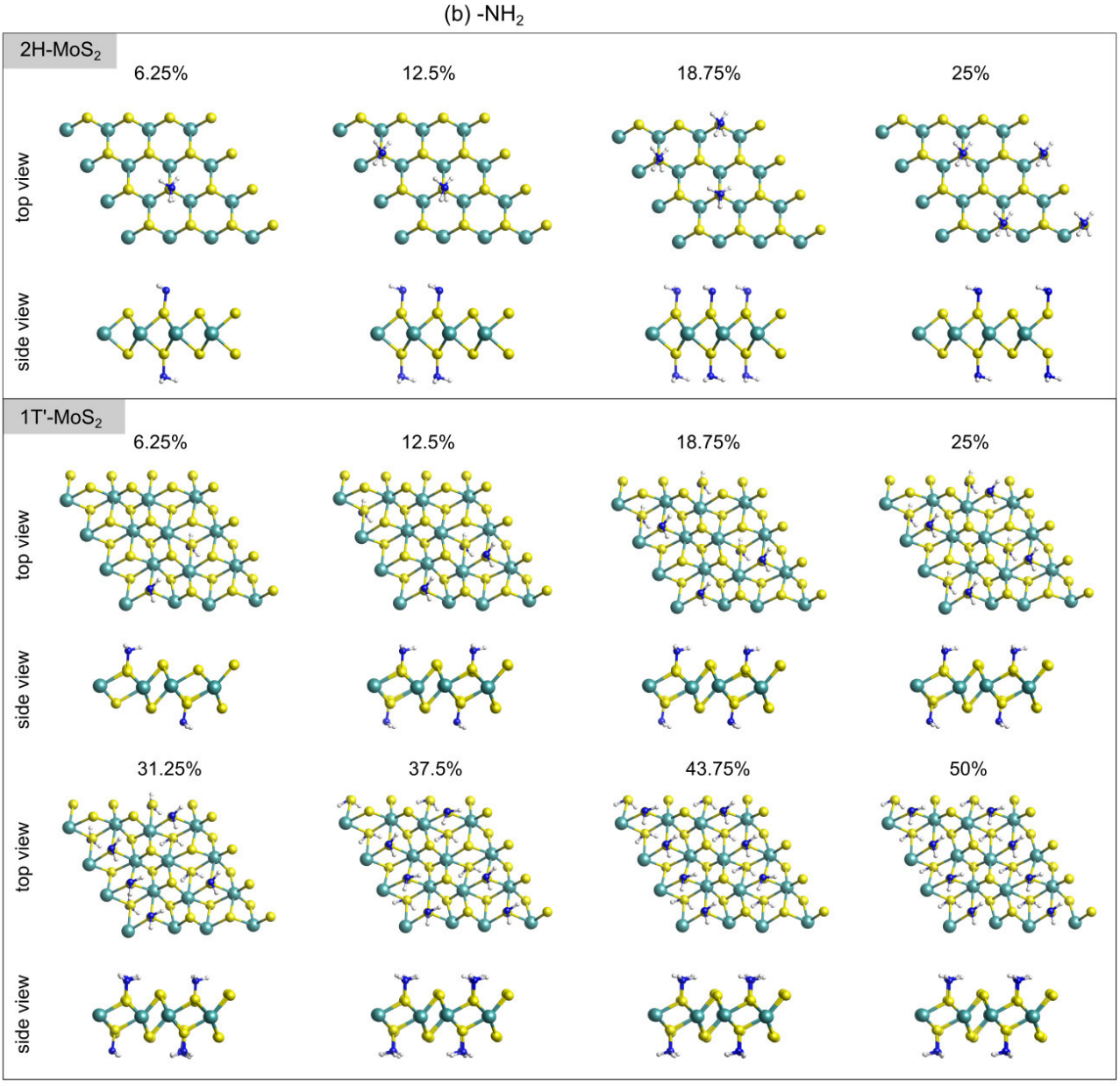
(b) -NH2
2H-MoS2
6.25%
12.5%
18.75%
25%
top view
side view
1T'-MoS2
6.25%
12.5%
18.75%
25%
top view
side view
31.25%
37.5%
43.75%
50%
top view
side view

(c) -CH_3

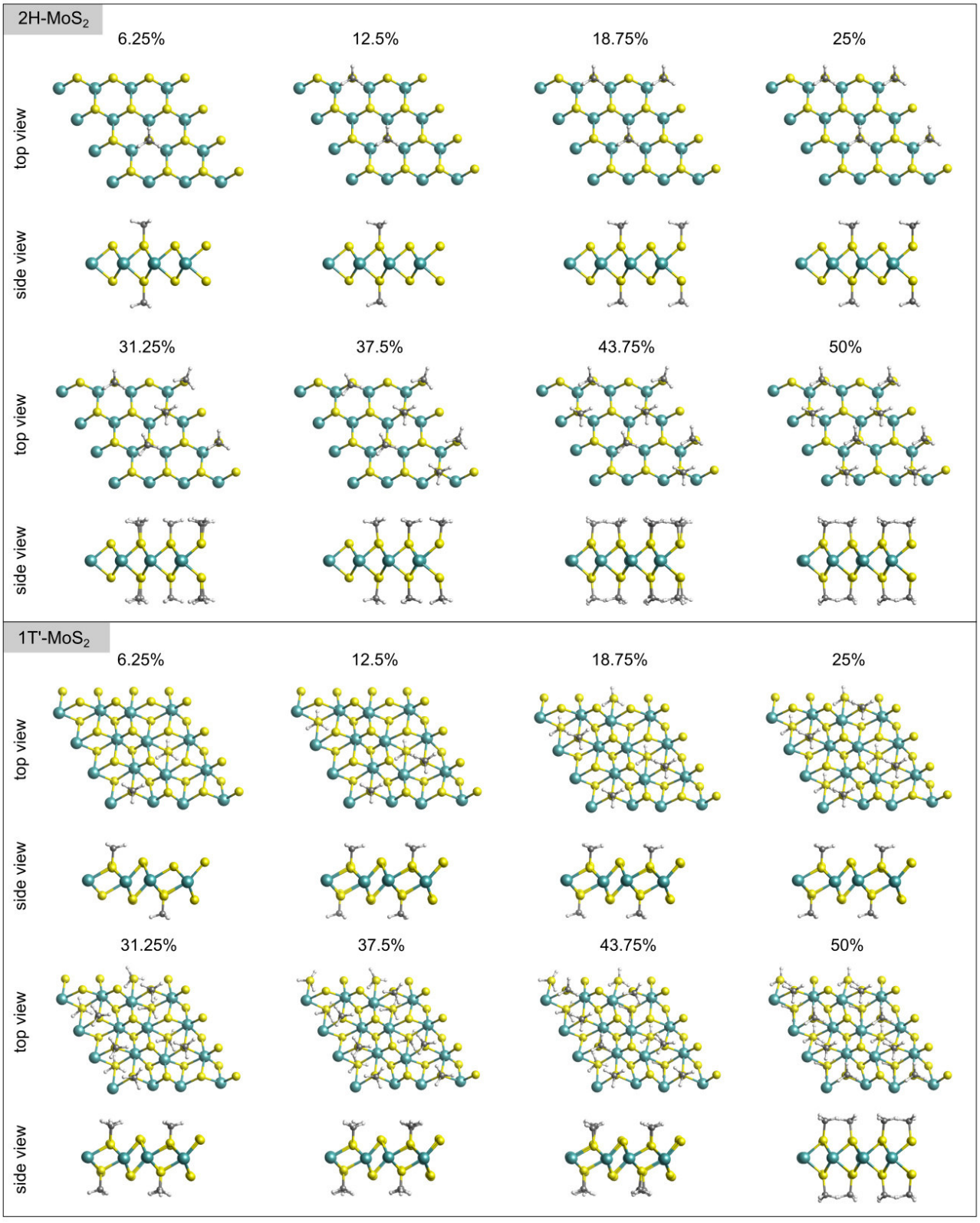
2H-MoS2
6.25%
12.5%
18.75%
25%
top view
side view
31.25%
37.5%
43.75%
50%
top view
side view
1T'-MoS2
6.25%
12.5%
18.75%
25%
top view
side view
31.25%
37.5%
43.75%
50%
top view
side view

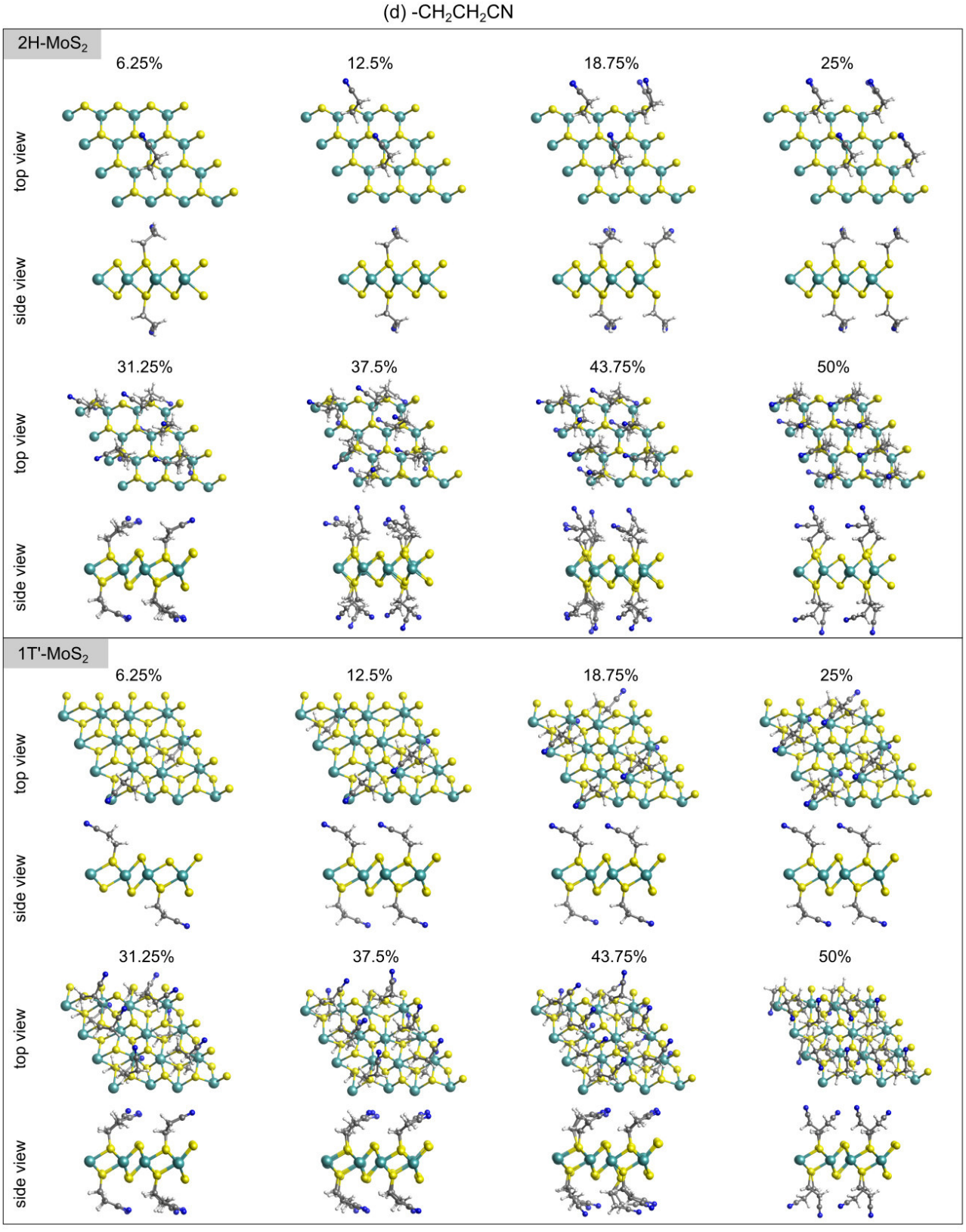
(d) -CH2CH2CN
2H-MoS2
6.25%
12.5%
18.75%
25%
top view
side view
31.25%
37.5%
43.75%
50%
top view
side view
1T'-MoS2
6.25%
12.5%
18.75%
25%
top view
side view
31.25%
37.5%
43.75%
50%
top view
side view

(e) -CH_2CH_2OH

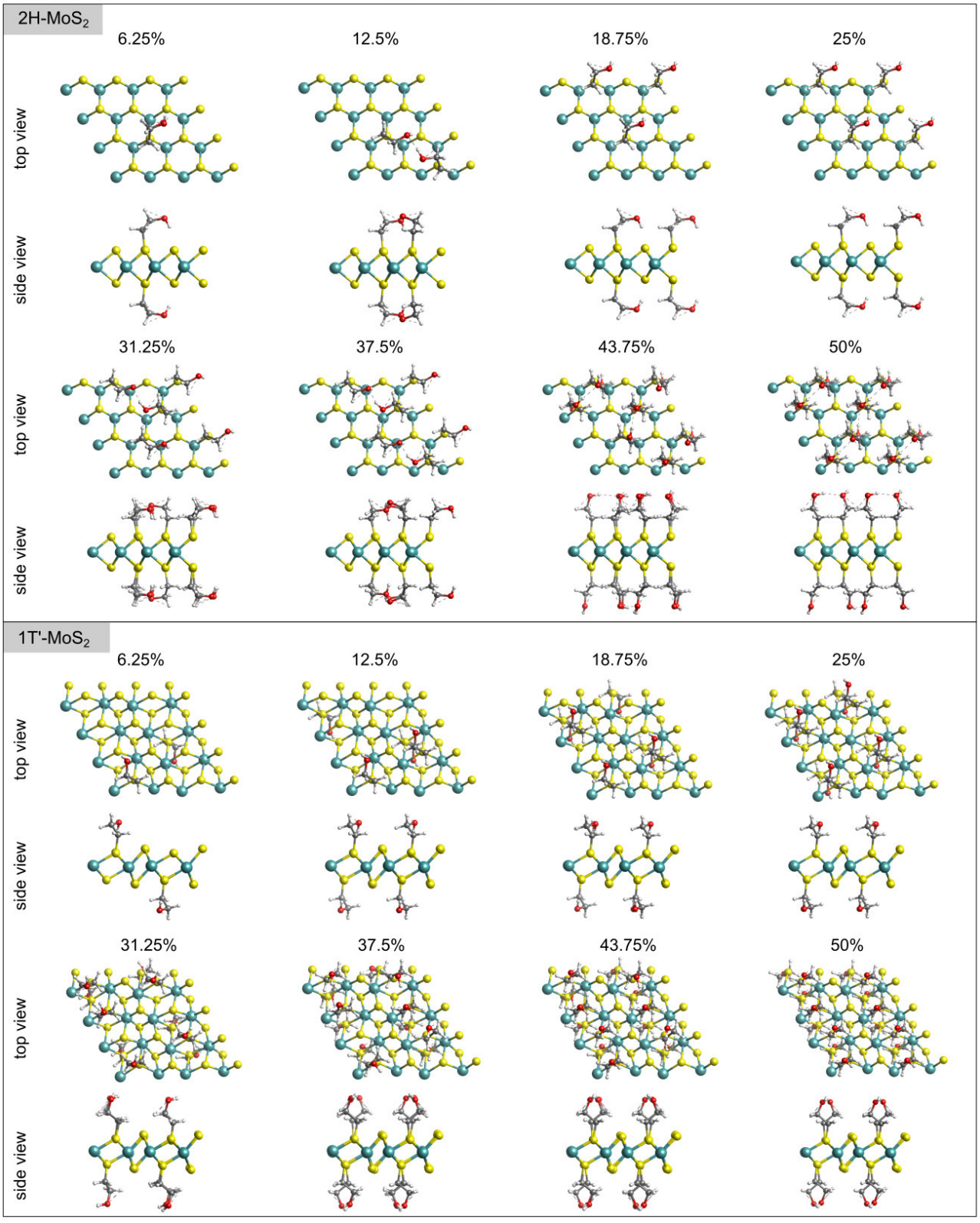
2H-MoS2
6.25%
12.5%
18.75%
25%
top view
side view
31.25%
37.5%
43.75%
50%
top view
side view
1T'-MoS2
6.25%
12.5%
18.75%
25%
top view
side view
31.25%
37.5%
43.75%
50%
top view
side view

(f) -Ph

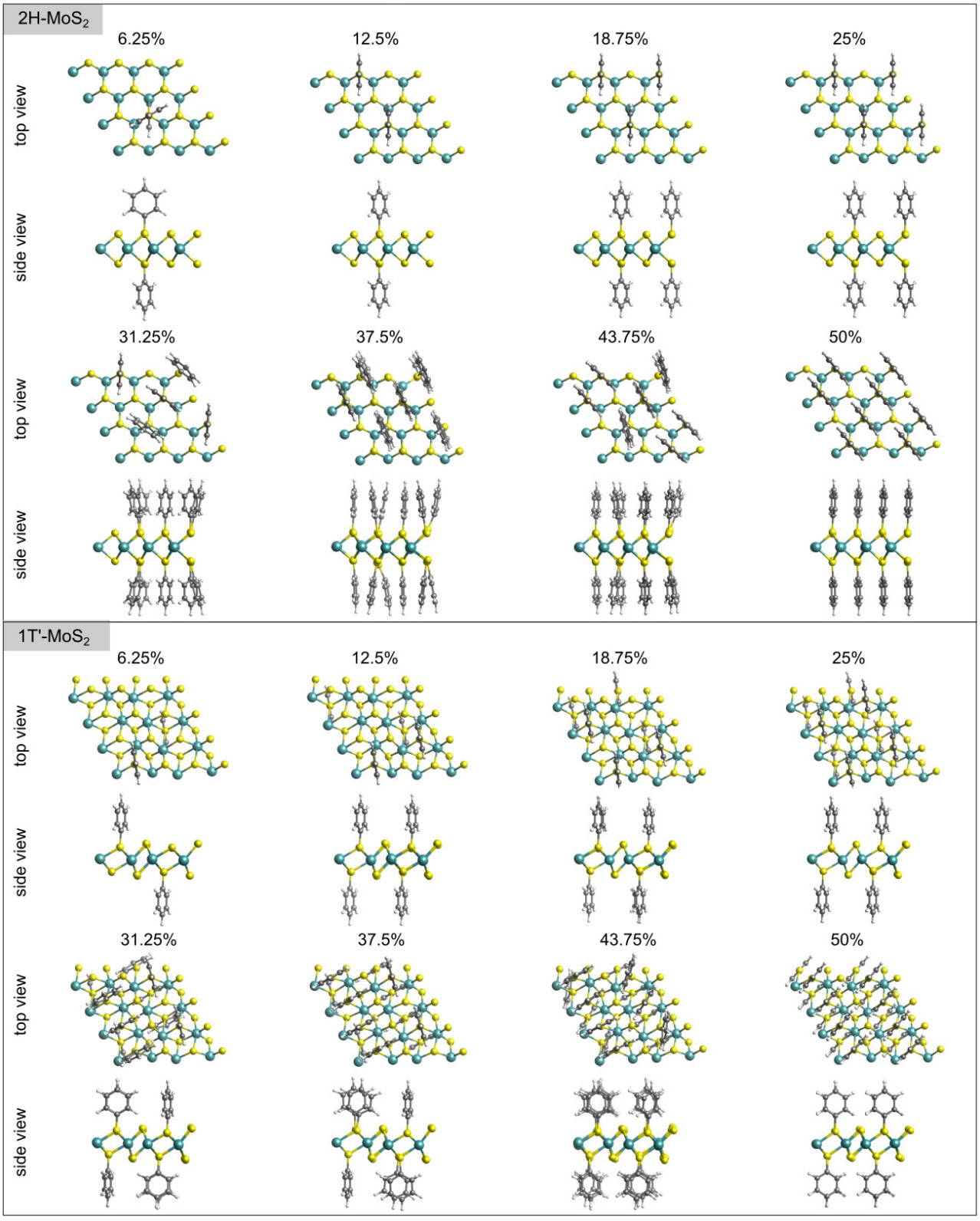
2H-MoS2
6.25%
12.5%
18.75%
25%
top view
side view
31.25%
37.5%
43.75%
50%
top view
side view
1T'-MoS2
6.25%
12.5%
18.75%
25%
top view
side view
31.25%
37.5%
43.75%
50%
top view
side view

(g) -$PhNO_2$

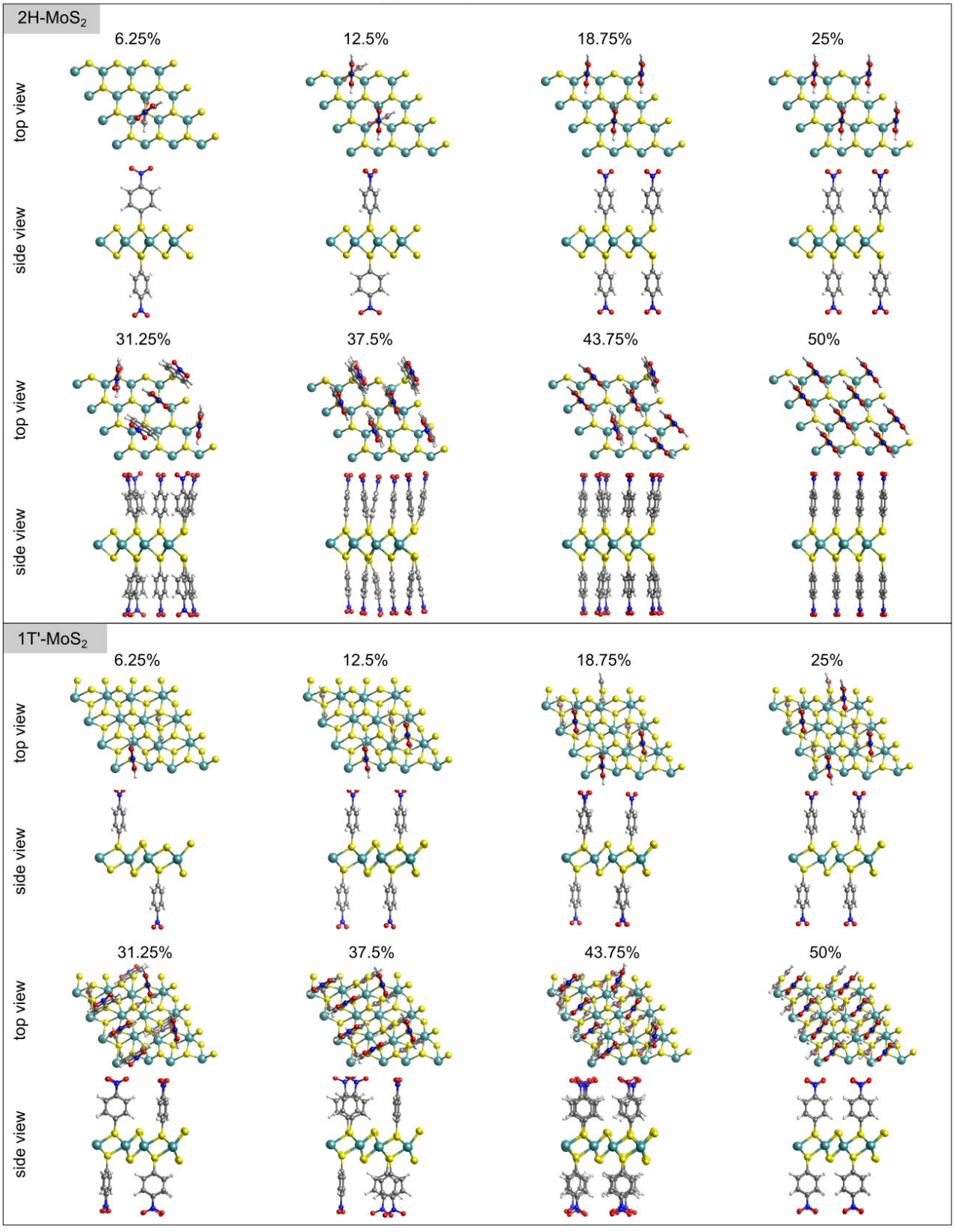
2H-MoS2
6.25%
12.5%
18.75%
25%
top view
side view
31.25%
37.5%
43.75%
50%
top view
side view
1T'-MoS2
6.25%
12.5%
18.75%
25%
top view
side view
31.25%
37.5%
43.75%
50%
top view
side view

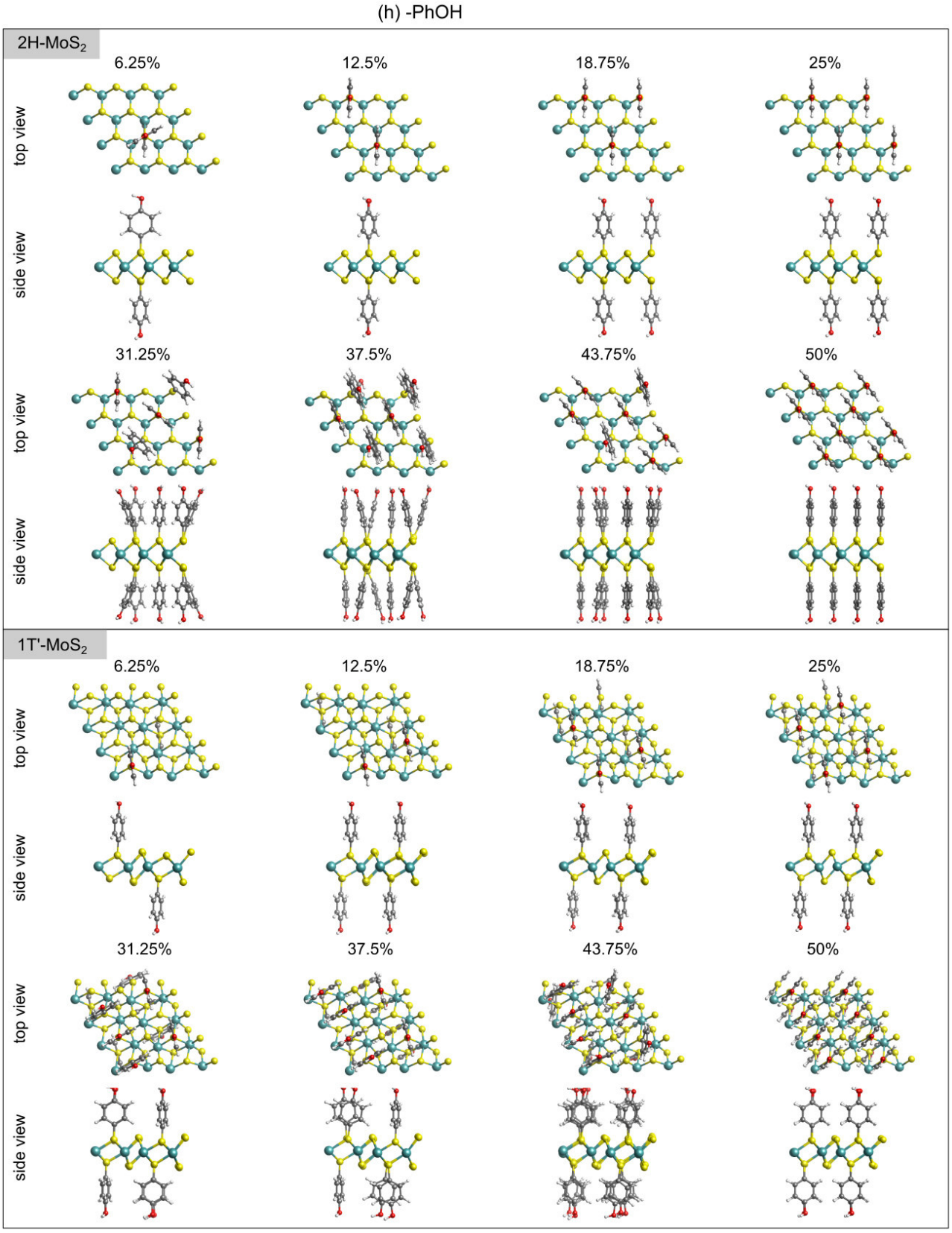
(h) -PhOH
2H-MoS2
6.25%
12.5%
18.75%
25%
top view
side view
31.25%
37.5%
43.75%
50%
top view
side view
1T'-MoS2
6.25%
12.5%
18.75%
25%
top view
side view
31.25%
37.5%
43.75%
50%
top view
side view

(i) m-F-CH_3

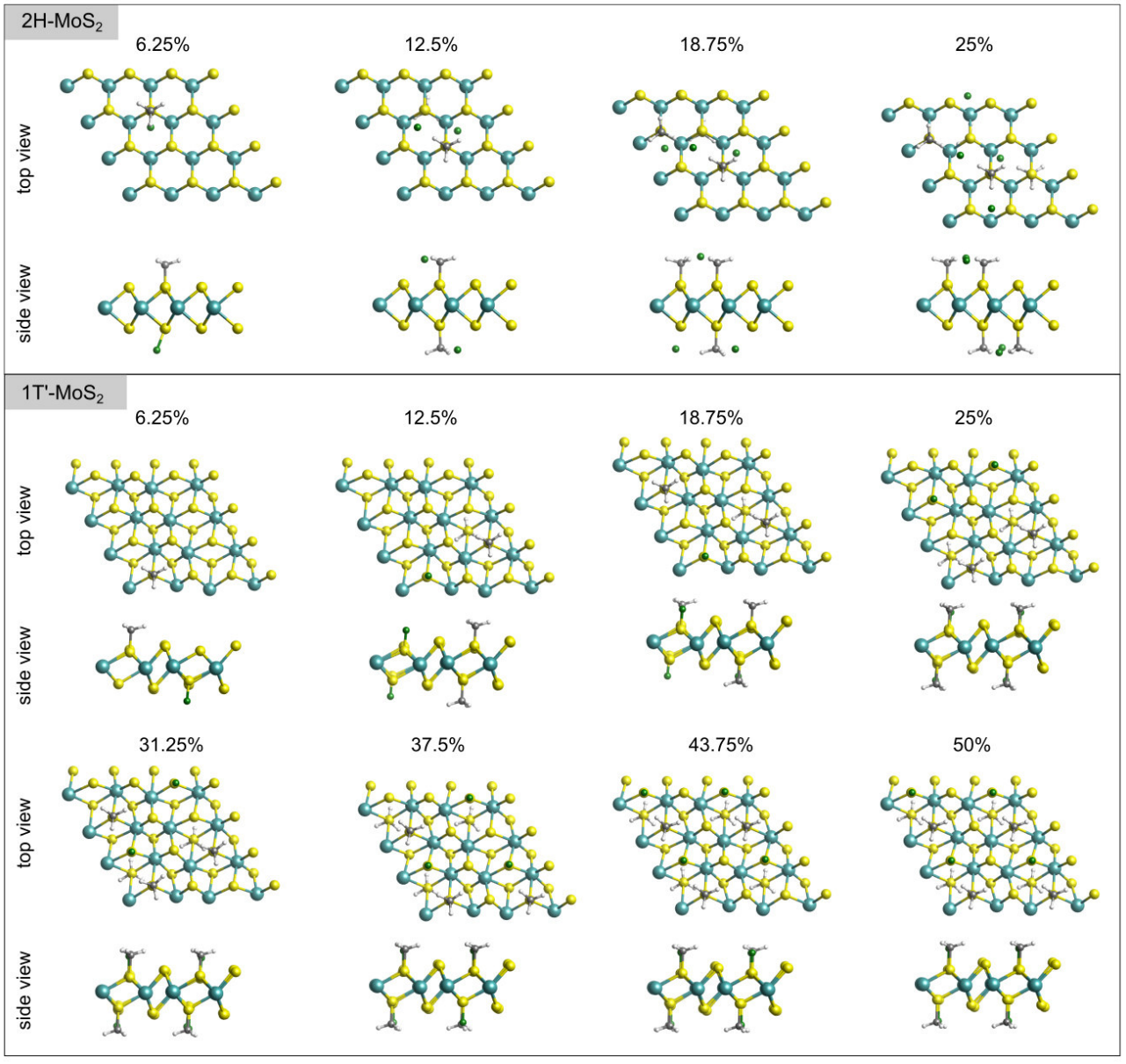
2H-MoS2
6.25%
12.5%
18.75%
25%
top view
side view
1T'-MoS2
6.25%
12.5%
18.75%
25%
top view
side view
31.25%
37.5%
43.75%
50%
top view
side view

(j) m-NH_2-CH_3

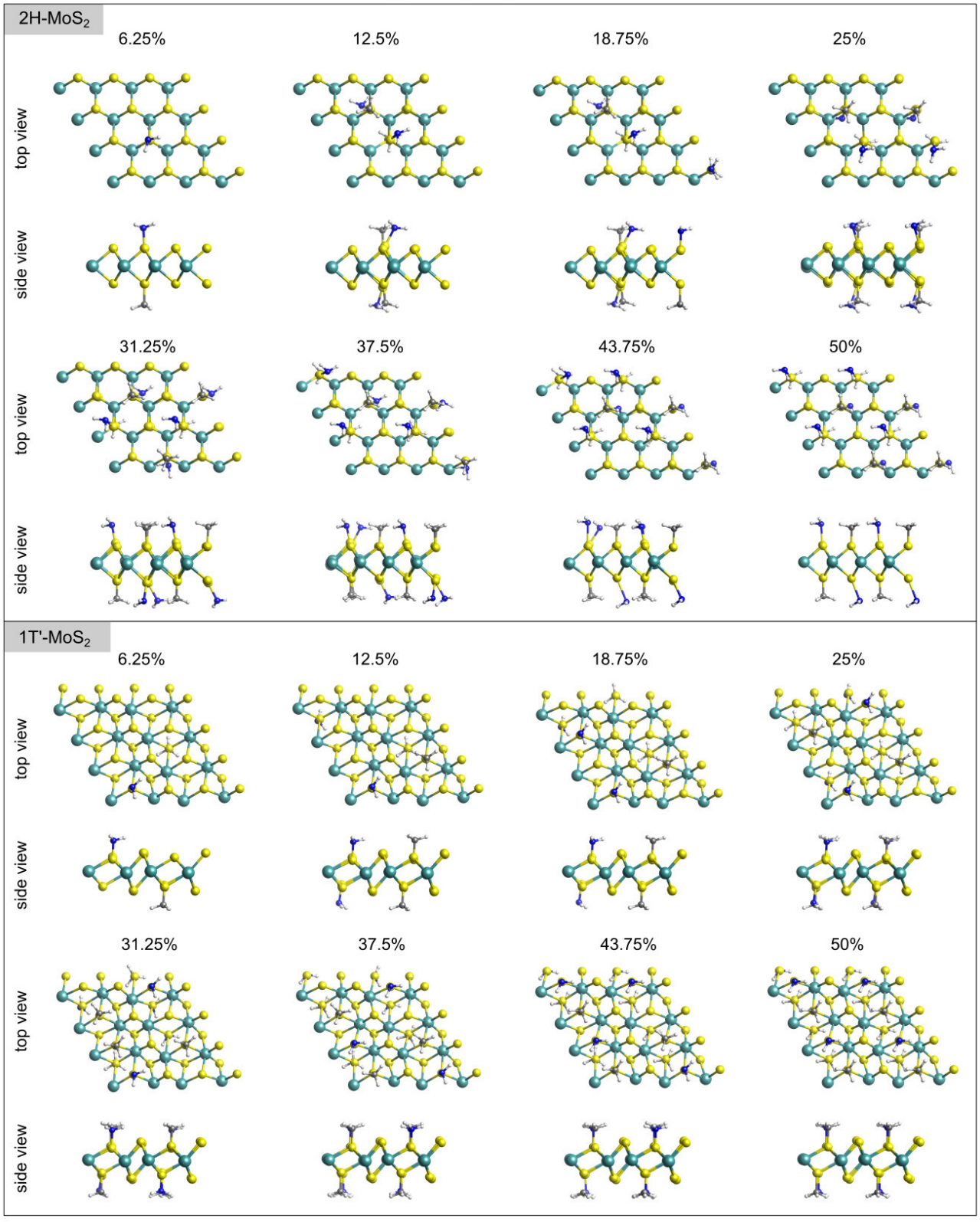
2H-MoS2
6.25%
12.5%
18.75%
25%
top view
side view
31.25%
37.5%
43.75%
50%
top view
side view
1T'-MoS2
6.25%
12.5%
18.75%
25%
top view
side view
31.25%
37.5%
43.75%
50%
top view
side view

(k) m-CH_3-Ph

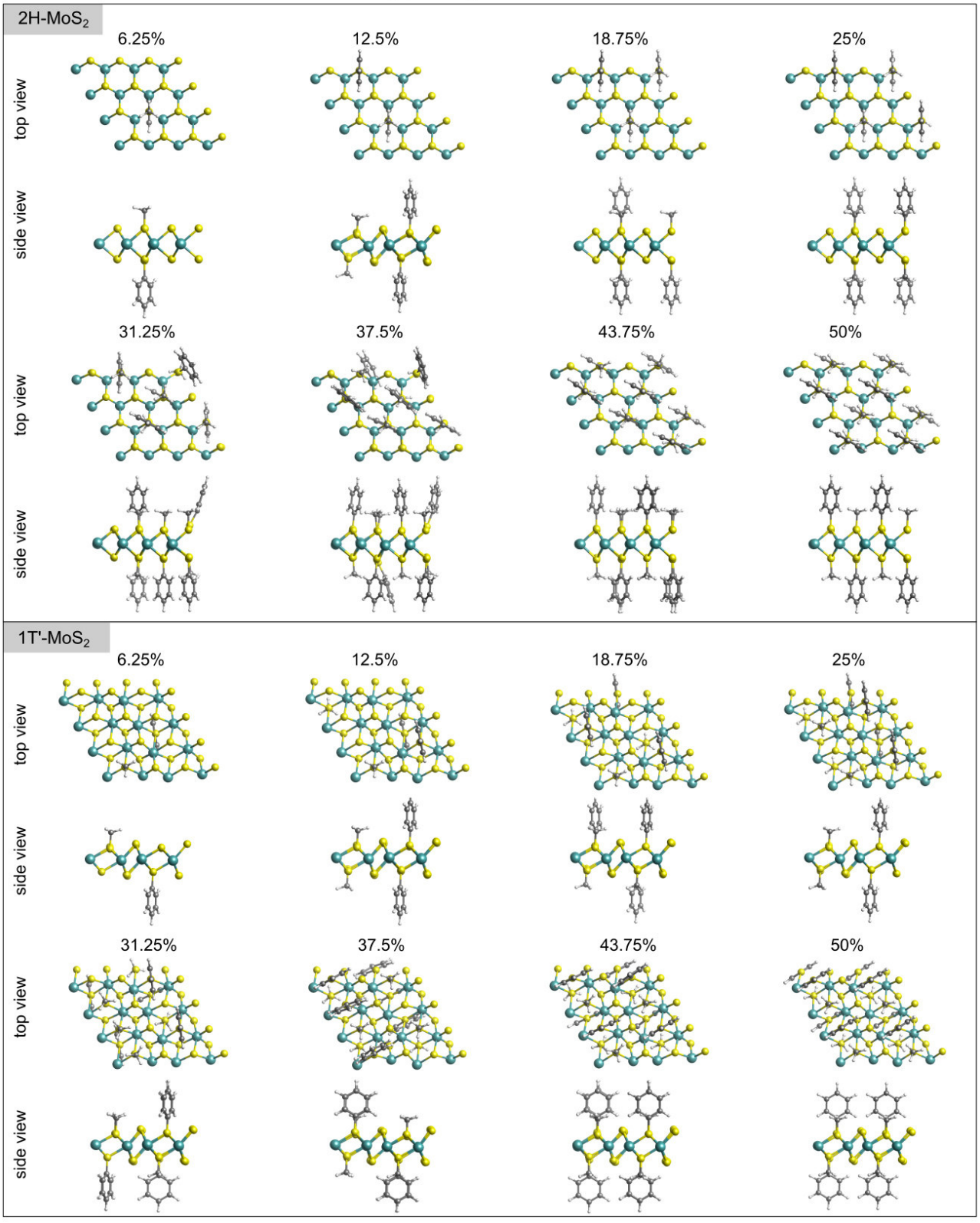
2H-MoS2
6.25%
12.5%
18.75%
25%
top view
side view
31.25%
37.5%
43.75%
50%
top view
side view
1T'-MoS2
6.25%
12.5%
18.75%
25%
top view
side view
31.25%
37.5%
43.75%
50%
top view
side view

(l) s-F-CH_3

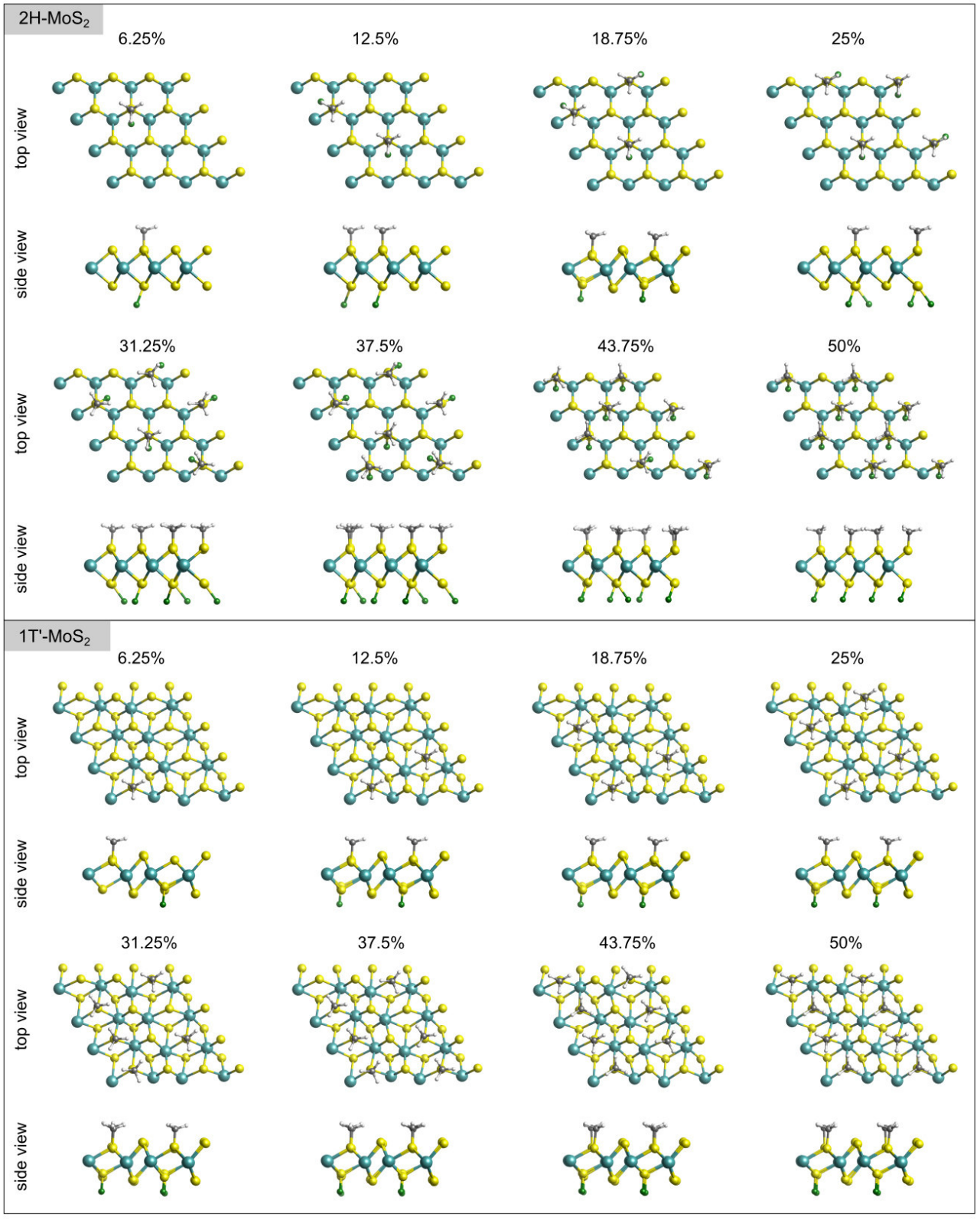
2H-MoS2
6.25%
12.5%
18.75%
25%
top view
side view
31.25%
37.5%
43.75%
50%
top view
side view
1T'-MoS2
6.25%
12.5%
18.75%
25%
top view
side view
31.25%
37.5%
43.75%
50%
top view
side view

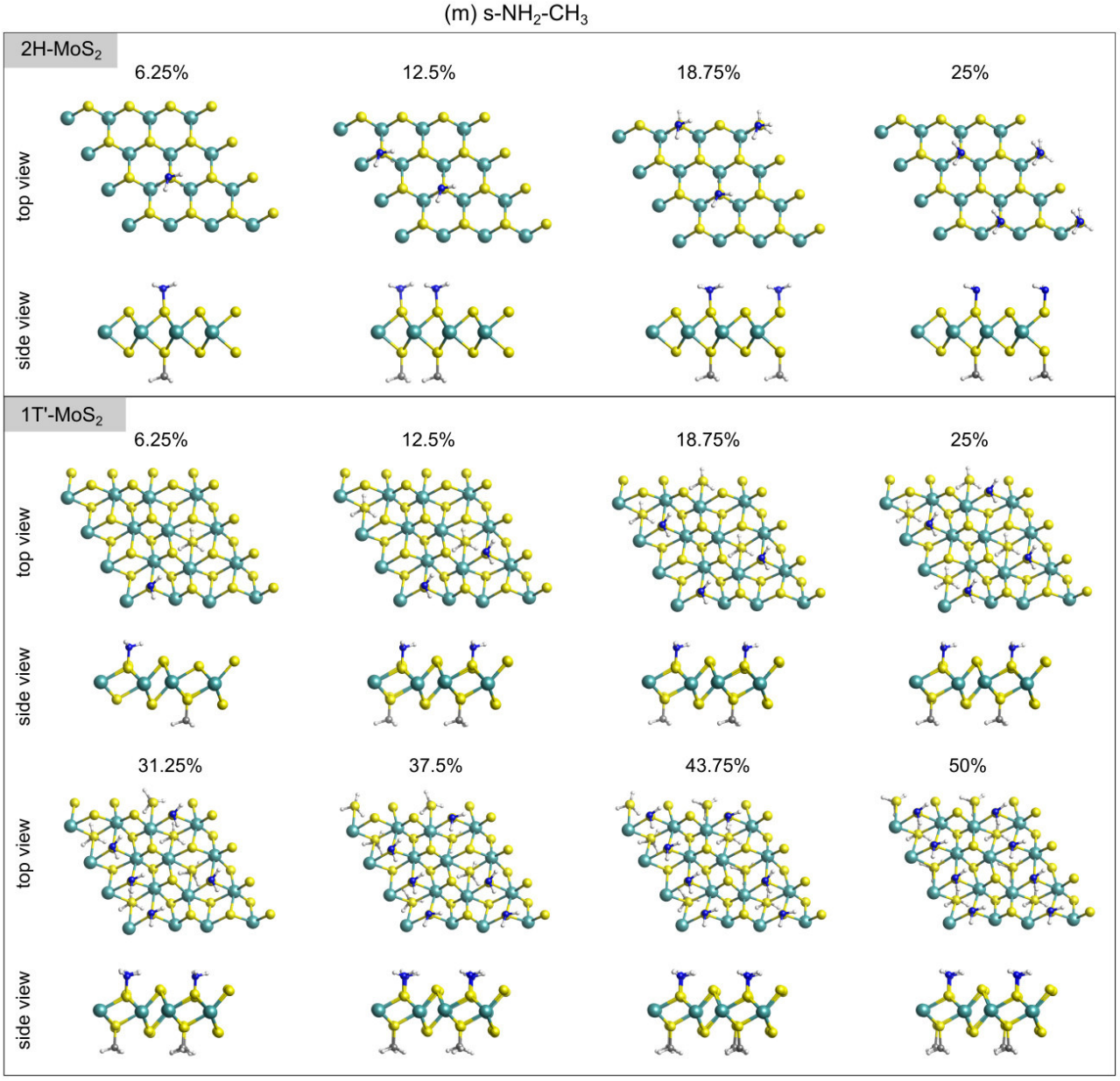
(m) s-NH2-CH3
2H-MoS2
6.25%
12.5%
18.75%
25%
top view
side view
1T'-MoS2
6.25%
12.5%
18.75%
25%
top view
side view
31.25%
37.5%
43.75%
50%
top view
side view

(n) s-CH_3-Ph

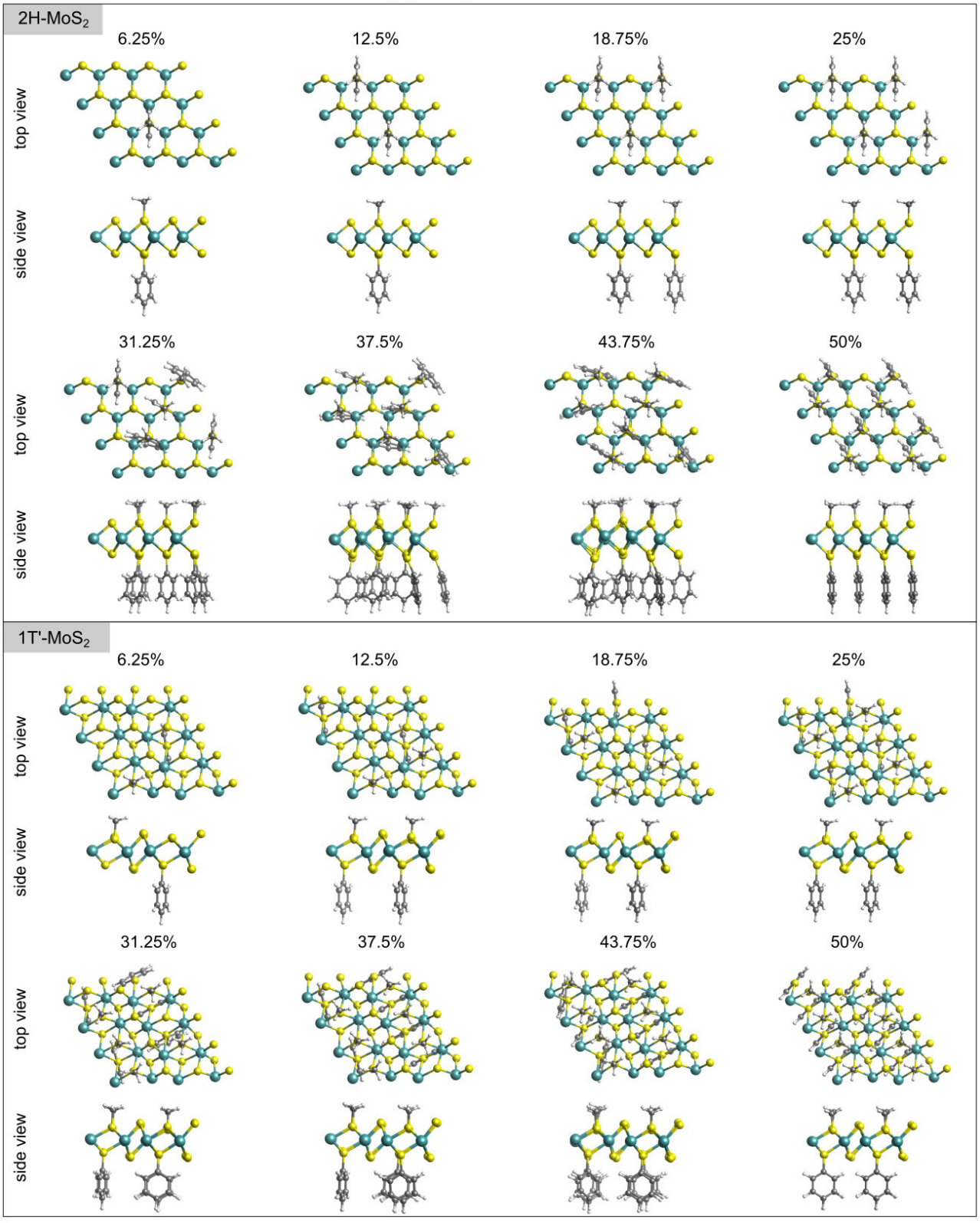
2H-MoS2
6.25%
12.5%
18.75%
25%
top view
side view
31.25%
37.5%
43.75%
50%
top view
side view
1T'-MoS2
6.25%
12.5%
18.75%
25%
top view
side view
31.25%
37.5%
43.75%
50%
top view
side view

Fig. S3: Average energy difference ΔE between functionalized 2H- and 1T'-MoS_2 as a function of the group coverage. Here $\Delta E = (E_{1T'} - E_{2H})/m$, where m is the number of MoS_2 units, $E_{1T'}$ and E_{2H} are the total enegry of functionalized 2H- and 1T'-MoS_2 for a given coverage, respectively. The positive ΔE indicates that functionalized 2H-MoS_2 is more stable, while the negative ΔE indicates that functionalized 1T'-MoS_2 is more stable.

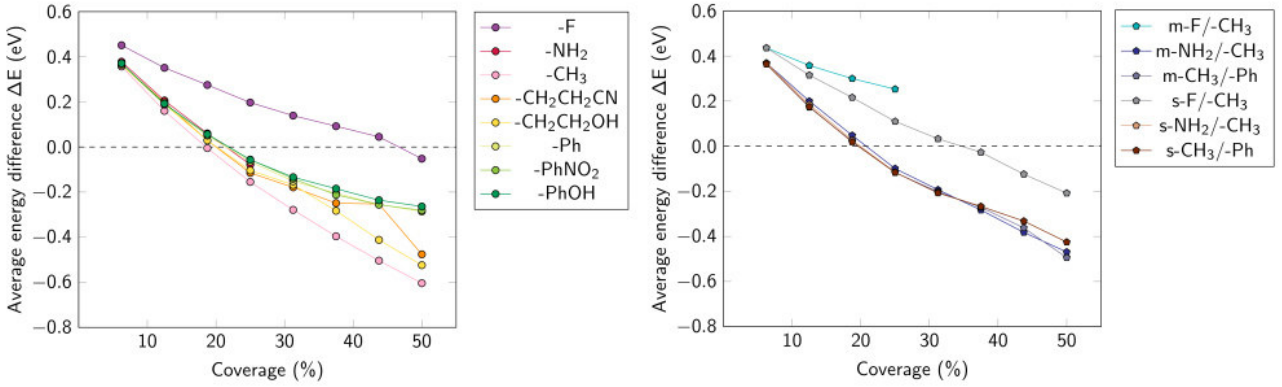

Fig. S4: Average Bader charge transfer ΔQ as a function of the group coverage with respect to the 2H- and 1T'-MoS_2 monolayers. Here $\Delta Q = \sum_i^N (Z_i - Q_i^{Bader})/n$, where N is the total number of atoms in the attached groups, Z_i is the number of electrons of atom i, Q_i^{Bader} is the Bader charge of atom i and n is the number of functional groups. A positive charge transfer value indicates electron flow from the substrate to the functional group.

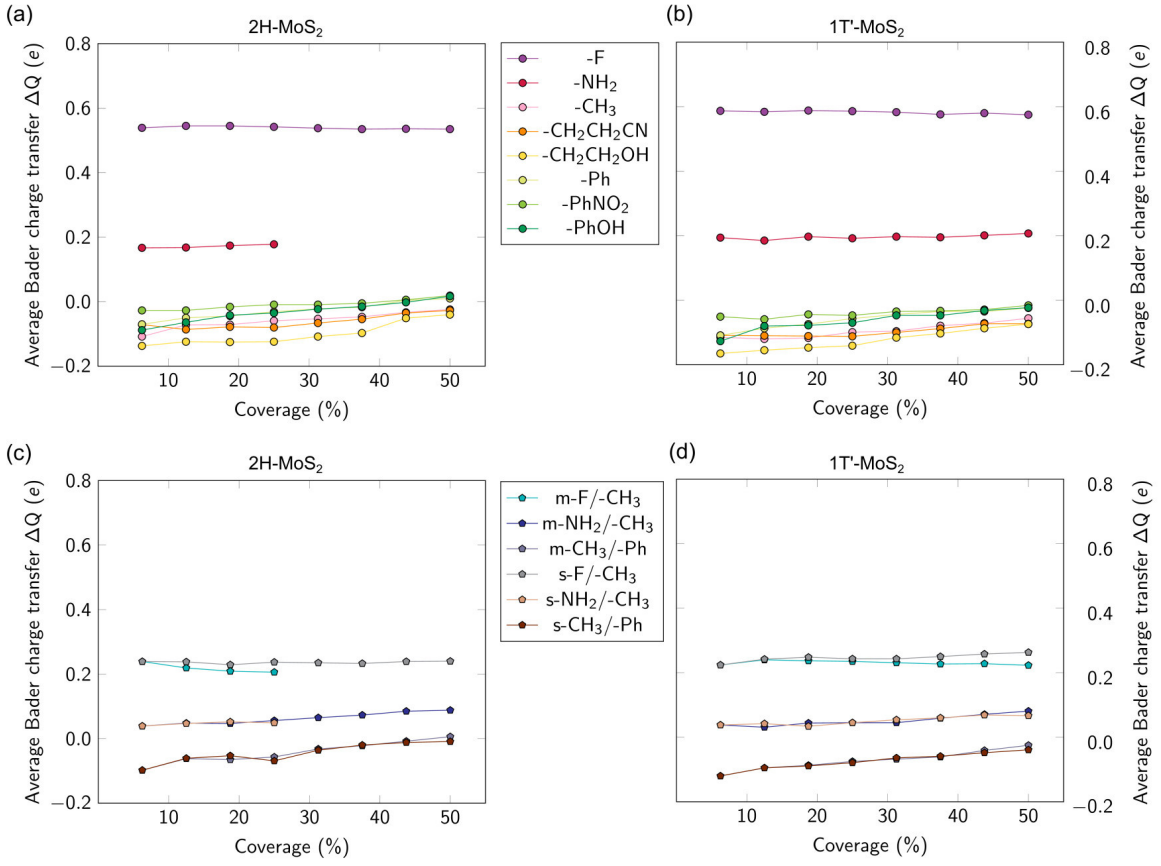

Fig. S5: DFT band gaps as a function of the group coverage with respect to the functionalized 2H-MoS_2 and 1T'-MoS_2 monolayers.

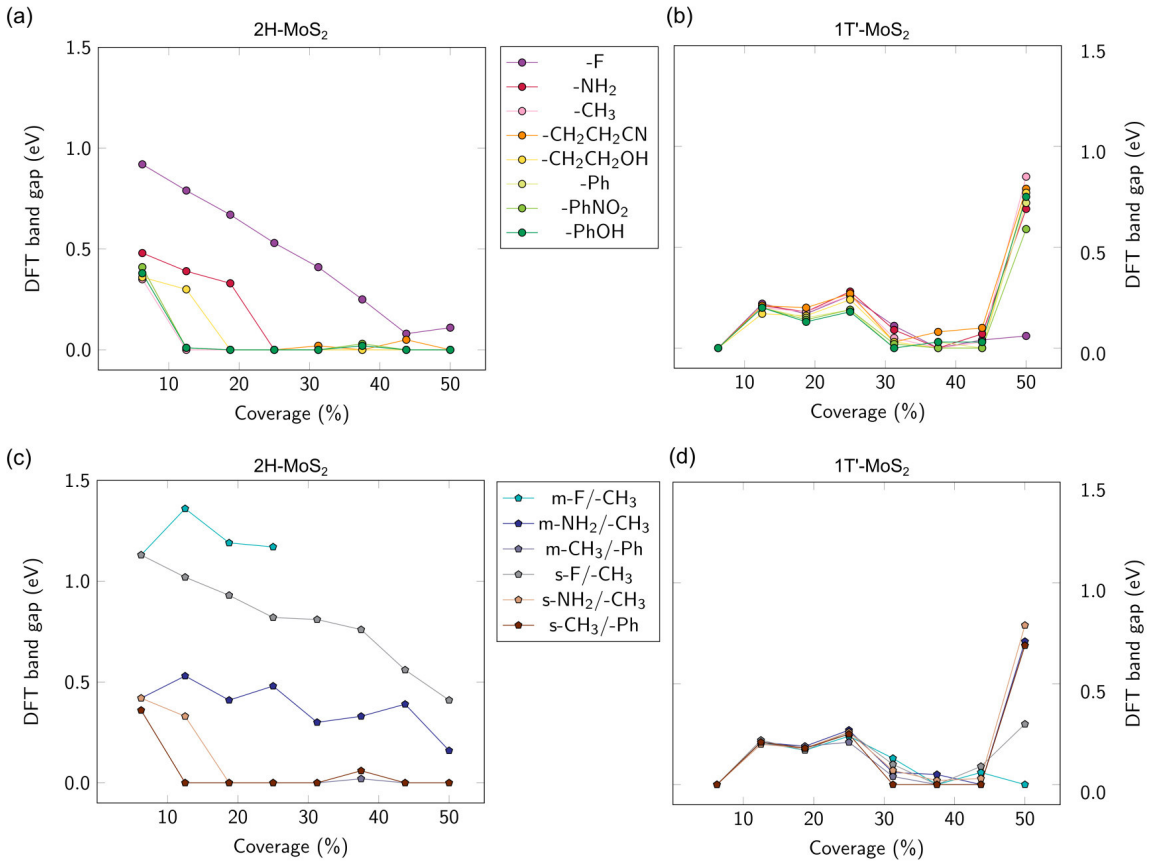

Fig. S6: Total density of states and the projected density of states for the functionalized (a) 2H-MoS_2 and (b) 1T'-MoS_2 calculated by PBE functional.

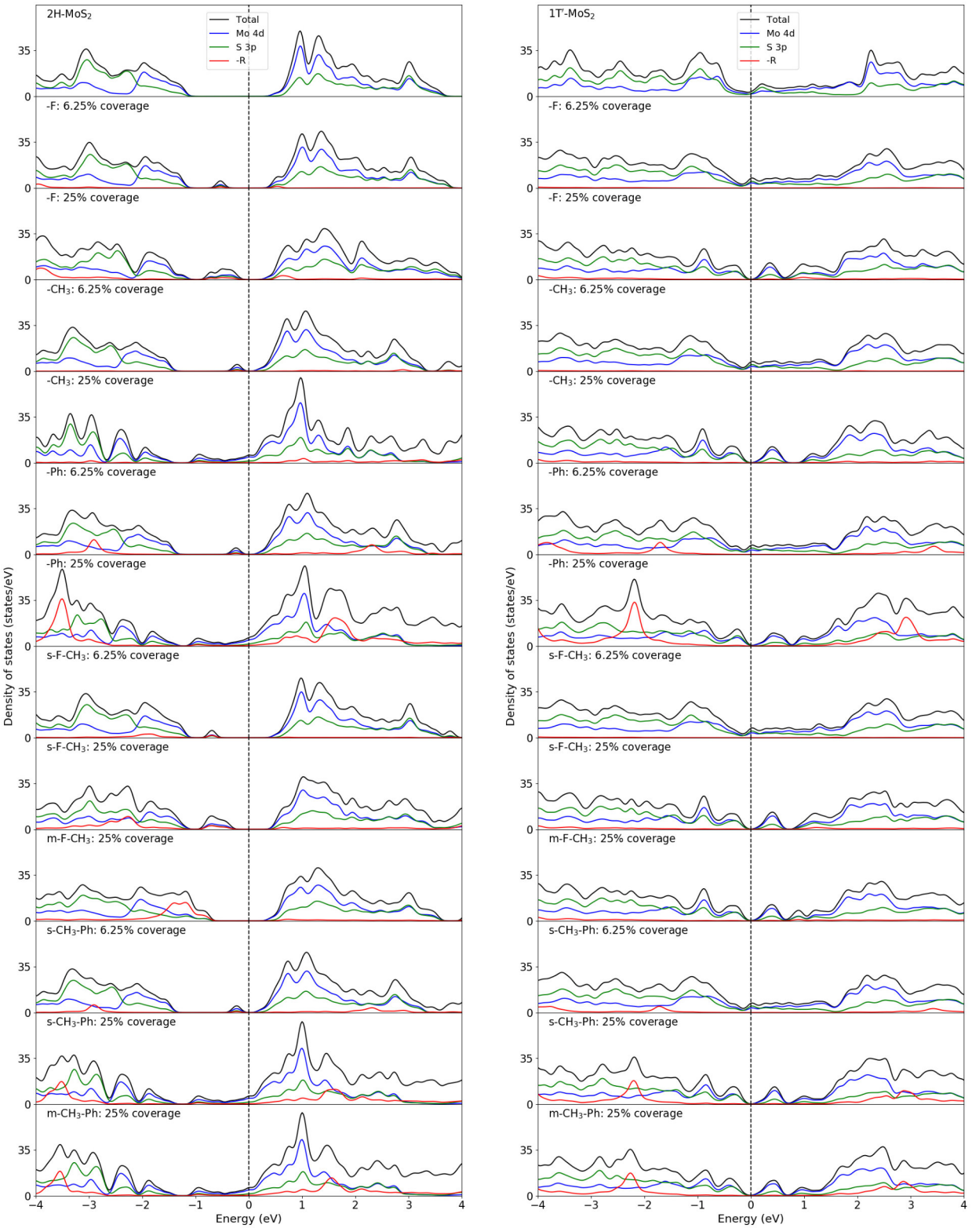

(a) 2H-MoS_2 (b) 1T'-MoS_2

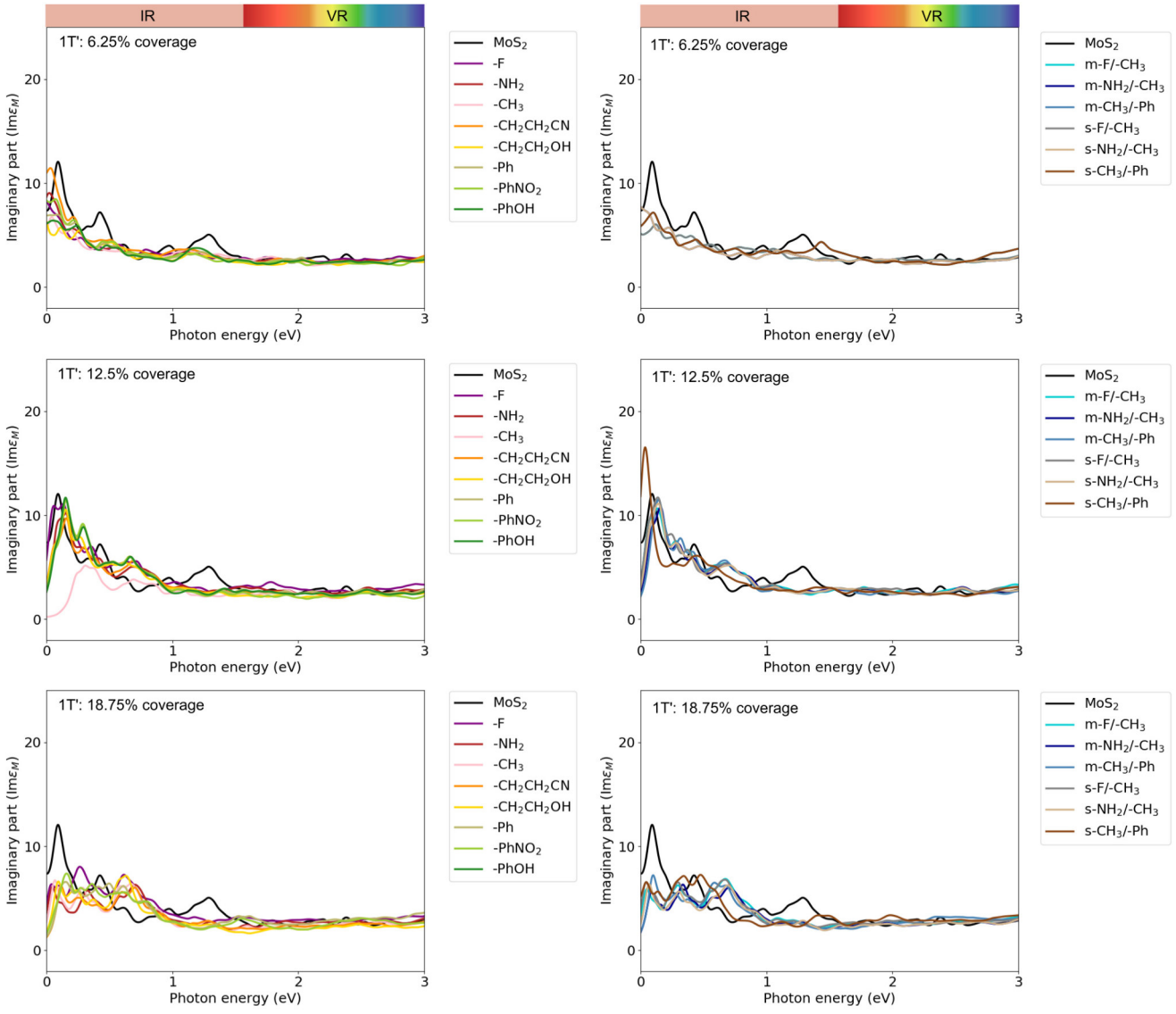

Fig. S7: Optical absorption spectra of the functionalized 1T'-MoS_2 monolayer.

Table S1: The optical band gap (E_{opt}) for the functionalized 2H-MoS_2 at 6.25% coverage. Energies are in eV.

	2H-MoS_2	-F	-NH_2	-CH_3	-CH_2CH_2CN	-CH_2CH_2OH
E_{opt}	1.84	1.14	0.55	0.37	0.49	0.37
E_{ext}	0.67	0.67	0.65	0.63	0.60	0.64
	-Ph	-$PhNO_2$	PhOH	m-F/-NH_2	m-NH_2/-CH_3	m-CH_3/-Ph
E_{opt}	0.37	0.43	0.37	1.49	0.48	0.17
E_{ext}	0.63	0.59	0.62	0.73	0.63	0.82
	s-F/-NH_2	s-NH_2/-CH_3	s-CH_3/-Ph			
E_{opt}	1.49	0.48	0.17			
E_{ext}	0.73	0.63	0.82			

[M4] **Toward a Comprehensive Understanding of Oxygen on MoS_2: From Reaction to Optical Properties.**

K. Wang and B. Paulus, *J. Phys. Chem. C.* **2021**, *125*, 19544–19550.

DOI: 10.1021/acs.jpcc.1c05473

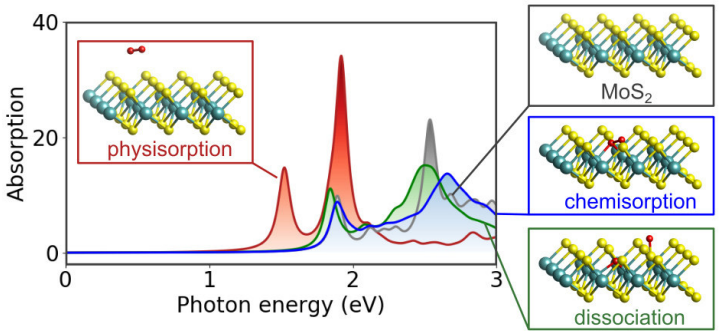

Graphical abstract of paper M4

Author contributions

The project was initially conceived by myself and Beate Paulus. All calculations contained in the manuscript were performed by myself. The manuscript was written by myself in collaboration with Beate Paulus. Liangliang Zhang and Jianliang Low helped in proofreading the manuscript.

[M5] **Tuning the binding energy of excitons in the MoS_2 monolayer by molecular functionalization and defective engineering.**

K. Wang and B. Paulus, *Phys. Chem. Chem. Phys.* **2020**, *22*, 11936–11942.
DOI: 10.1039/D0CP01239D

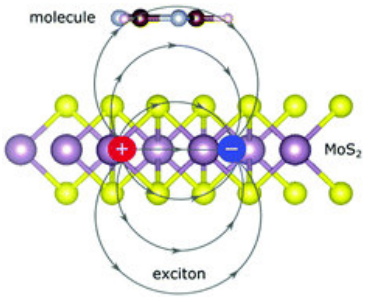

Graphical abstract of paper M5

Author contributions

The project was initially conceived by myself and Beate Paulus. All calculations contained in the manuscript were performed by myself. The manuscript was written by myself in collaboration with Beate Paulus. Liangliang Zhang helped in proofreading the manuscript.

4 Conclusions

In this thesis, we focused on tuning the structural, electronic and optical properties of graphene and TMDC by means of stacking (**paper M1**), covalent functionalization (**paper M2** and **paper M3**), and defect doping in combination with small molecules adsorption (**paper M4** and **paper M5**). In the following, I will summarise and discuss the results of each project in the order of the included papers and elucidate on the connections between them.

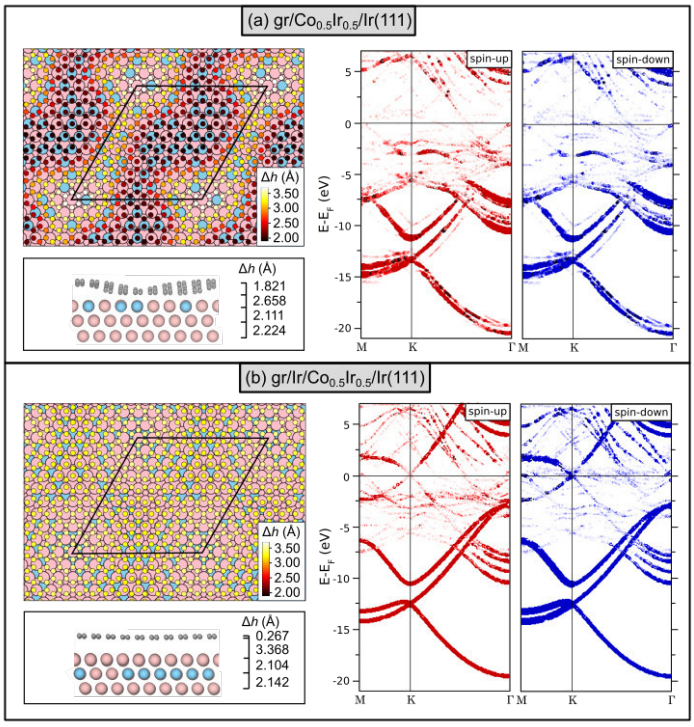

Figure 4.1: Structural models and band structures of (a) graphene/$Co_{0.5}Ir_{0.5}$/Ir(111) and (b) graphene/Ir/$Co_{0.5}Ir_{0.5}$/Ir(111). The colour scale indicates the heights measured from the first layer of the substrate. The black rhombus marks the unit cell of the considered system. Ir and Co atoms are shown in pink and blue, respectively.

Paper M1. In view of experimental technology, the most promising method for the preparation of the graphene layer was the synthesis of a graphene sheet on the metallic support via CVD. The intercalation of foreign atoms or molecules between a graphene sheet and its substrate often affected the properties of the considered interface. However, the study of intercalation of alloy in between graphene and substrate was still lacking.

Hence, in this project we explored how different compositions of surface and near-surface alloys (Co_xIr_{1-x}, $0<x<1$) influenced the moiré structure, graphene-metal charge transfer, band structure, and stability of a graphene layer on Ir(111) by DFT method, and further compared them with the experimental results. In this work, five different stoichiometric compositions of Co_xIr_{1-x} alloy were considered, i.e. x =0.00, 0.25, 0.50, 0.75 and 1.00. As shown in Figure 4.1, the surface alloy of Co_xIr_{1-x} on Ir(111) would remarkably enhance the corrugation of the graphene moiré superstructure, and this trend was strengthened with the increase of Co composition. This indicated the strong interaction between graphene and the surface alloy, which could be further proved by our charge density difference analysis. As a result, the Dirac cone of graphene as well as linear dispersion of p states was destroyed by the surface Co_xIr_{1-x} alloy, in particular at the high Co concentration. In contrast, the subsurface alloy of Co_xIr_{1-x} in Ir(111) would suppress the geometrical corrugation and this effect was rather insensitive to the x value. This was due to the rather weak interaction of graphene with the substrate since the subsurface Co-Ir alloy in Ir(111) under graphene blocked the interaction between graphene and the Ir surface layer. Thereby the graphene layer was more quasi freestanding and the Dirac cone was well preserved accompanied by weak p doping. Our analysis of stability suggested that at low Co concentration, the Co_xIr_{1-x} alloy preferred to exist on the subsurface underneath the gr/Ir interface bilayer to interact indirectly with the graphene layer; whereas at high Co concentration, Co_xIr_{1-x} alloy tended to segregate to the surface, thereby directly bonding with the graphene monolayer. This depended on the balance between the deformation of graphene and the interaction of graphene with the substrate. Our results, in particular the band structures were supported by intensive ARPES measurements, which demonstrated that, when graphene was lying on a Co monolayer on Ir(111), the Dirac cone vanished. The formation of subsurface Co-Ir alloy restored the presence of the Dirac cone at the Fermi level. The deeper insights into the interplay between graphene structure and different kinds of Co_xIr_{1-x} alloy from this study are expected to provide a useful guide for achieving precise layer controlled graphene growth and the design of graphene-based devices.

Paper M2. By utilizing plasma (such as CF_4 and SF_6) or exposing graphene to weak fluorination agents (such as XeF_2 and HF aqueous solution), fluorinated graphene could be generated efficiently.[96, 211] Furthermore, partially fluorinated graphene has also been synthesized.[96] Obviously, it is worthy of conducting a systematic investigation on fluorinated graphene, including the geometric, electronic and optical properties. Moreover, the effect of fluorinated coverages on the behaviors of conductance and optical absorption has not been explored in previous studies. Therefore, we intended to investigate the electronic and optical properties of partially fluorinated graphene with various fluorination coverages by the DFT-GW-BSE method. Our initial calculation suggested that the two-sided fluorinated configuration was much more stable than the one-sided ones and consequently this work mainly focused on the two-sided fluorinated graphene.

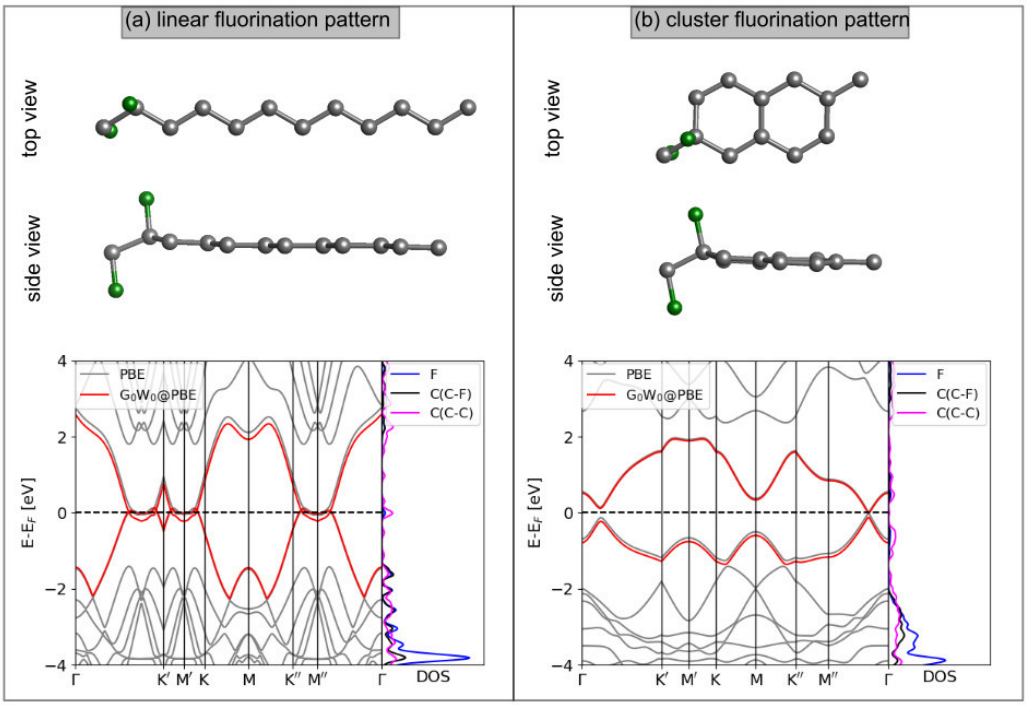

Figure 4.2: Structural models and band structures of (a) linear fluorination pattern and (b) cluster fluorination pattern at 16.7% coverage. C and F atoms are shown in grey and green, respectively.

Different graphene supercells, 6×1 and 3×2, were employed for two-sided fluorination, which corresponds to the linear fluorination pattern and cluster fluorination pattern, respectively (see Figure 4.2). Our stability analysis showed that at the low fluorinated coverage, the linear fluorination pattern was energetically more favorable; as the fluorinated coverage increased, the energy difference between the two patterns became smaller, indicating that both patterns may occur in the synthesis at a high coverage. For both fluorination patterns, an increase in the fluorination coverage yielded a general increase in the band gap value. In particular, at the 100% coverage, the band gap of the fluorinated graphene reached as large as 6.76 eV. The detailed study indicated that the band gap was determined by the fluorination coverage to a large extent, while the fluorination pattern had a strong impact on the characteristics of the bands and the electron mobilities along certain high symmetry paths. Concerning the optical absorption, the resulting spectra of linear fluorination pattern were sensitive toward the polarization directions of the electromagnetic field, as a linear fluorination pattern provided geometric possibilities for confined electrons; while the cluster fluorination pattern was rather robust in this regard, as confined electrons in one specific direction were not possible. From a theoretical point of view, the expected properties (e.g. the opening of the band gap) of fluorinated graphene can be fully realized when a required quantity of fluorine atoms is placed with the necessary concentration on the graphene plane. This is an experimentally challenging

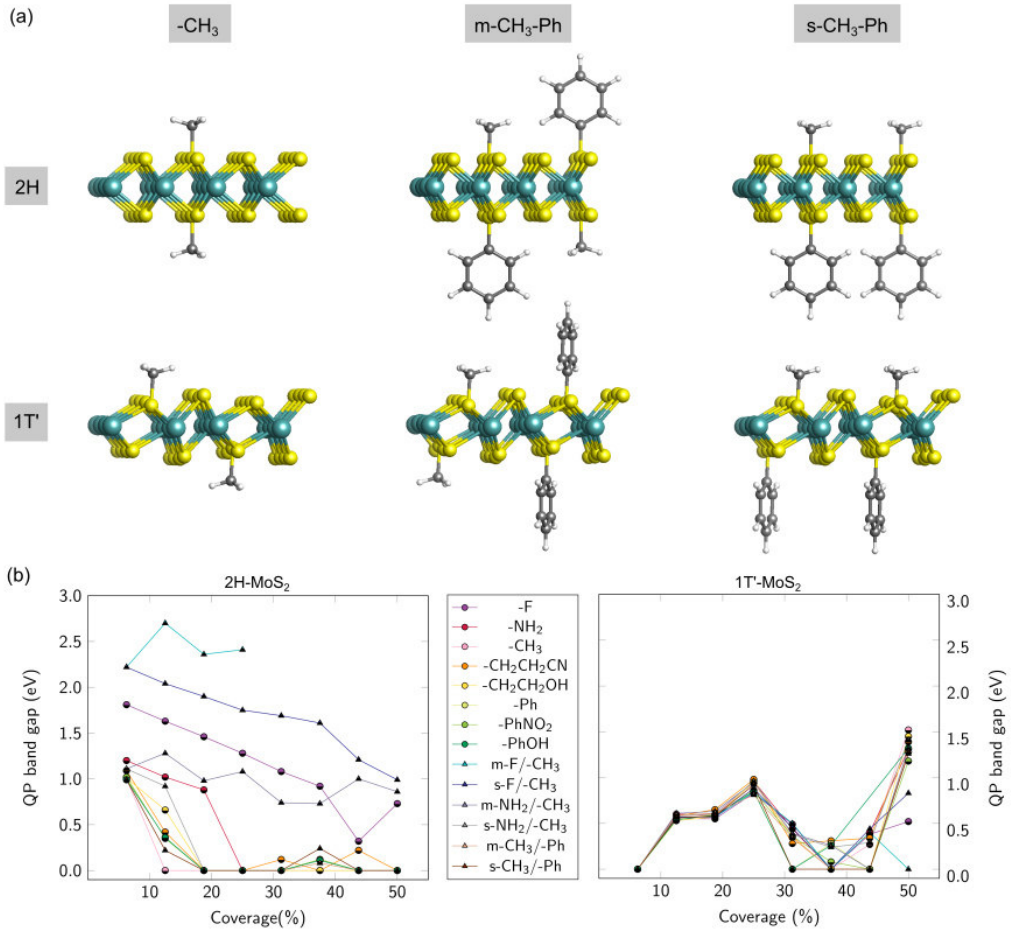

Figure 4.3: QP band gap as a functional of coverage of functionalized (a) 2H-MoS_2 and (b) 1T'-MoS_2.

task, which requires the use of nanoscale manipulations.

Paper M3. In addition to fluorinated graphene, experimental studies had demonstrated that the 2H- and 1T-MoS_2 could be covalently functionalized by various functional groups.[92, 95, 212, 213] Despite the large number of studies on the covalently functionalized MoS_2, no systematic study was carried out on monofunctionalization with large functional groups as well as bisfunctionalization. Therefore, in the present study, we performed first principle calculations to investigate the effect of monofunctionalization and bisfunctionalization at different coverages on the 2H- and 1T'-MoS_2. The functionalized T phase was not considered since this structure evolves to T' structure upon energy minimization. Non-aromatic derivatives (-F, -NH_2, -CH_3, -CH_2CH_2CN and -CH_2CH_2OH) and aromatic derivatives (-Ph, -$PhNO_2$ and PhOH) with varying electron donor and acceptor properties were used to monofunctionalize 2H- and 1T'-MoS_2. Furthermore, bisfunctionalization including mixed bisfunctionalization, where the different kinds of groups were mixed and bonded to both sides of the MoS_2 monolayer, and separated

bisfunctionalization, where the different kinds of groups were bonded respectively to different sides of the MoS_2 monolayer, were also considered in this study (see Figure 4.3(a)). We found that bisfunctionalization of 2H-MoS_2, such as with m-F-CH_3 and m-NH_2-CH_3, could promote the formation of intermolecular hydrogen bonds and therefore, improve the stability. For other cases, the average binding energy first reduced with the increase of coverage, which indicated that the functional group could act as an anchor, boosting further functionalization of 2H-MoS_2; when the functionalization coverage exceeded certain value, the computed trends for the binding energy increased as the coverage increased, suggesting that the high functionalization coverage was unfavorable due to the repulsion interaction between the organic groups. The direction of charge transfer between the adsorbate and substrate exhibited a strong dependence on the electron donating or withdrawing ability of functional groups. The functionalized 2H-MoS_2 displayed a semiconducting feature at 6.25% functionalized coverage; whereas the functionalized 1T'-MoS_2 was predicted to be metallic at the same coverage. As the coverage increased, the variation of band gaps of both 2H-and 1T'-Mo_2 showed an oscillatory behavior (see Figure 4.3(b)). Compared to the bare 2H-MoS_2, the optical adsorption for each group was red-shifted at 6.25% coverage; as the coverage increased to 18.75%, the overall optical absorbance remained shifting to the infrared region and the intensity of optical adsorption was enhanced remarkably, especially in the spectral range of 0-1 eV. The red-shift of optical absorption spectra concerning bare 2H-MoS_2 was attributed to a joint effect: (1) the reduced electronic band gap upon monofunctionaliation and bisfunctionaliation and (2) the variation of exciton binding energy. In the case of functionalized 1T'-MoS_2, we observed an obvious blue-shift of the optical spectrum and an increase in optical absorption as the coverage increased from 6.25% to 18.75%. This was related to the opening of the electronic band gap of 1T'-MoS_2 upon functionalizaion.

Paper M4. Oxygen (O_2) was one of the most important gas adsorbates because it was not only the second most abundant gas in the environment, but could significantly tune the properties of 2D materials, and thus was highly likely to affect the performance of devices in practical applications. Moreover, experimental studies found that the PL intensity of MoS_2 was greatly enhanced after O_2 treatment.[214–217] At present, the atomic configuration causing the optical enhancement is still controversial and two possible configurations have been proposed: (i) the physisorbed O_2, where the PL intensity changes instantaneously with changes in gas pressure;[214] (ii) the chemisorbed O_2, where the enhanced PL intensities of some locations in the sampling remain enhanced and stabilized after pumping process and laser irradiation. Hence, in this work, we explored the effect of different adsorption modes of O_2, including physisorption, chemisorption, and dissociation, on the electronic, optical, and excitonic properties of both pristine and defective MoS_2 monolayers. The defective MoS_2 was created by removing one S atom from a supercell since theoretical and experimental studies had proved that the sulfur (S) defects were the predominant point defect in 2D-MoS_2. [215]

The corresponding defect density is 6.2×10^{13} cm^{-2}, which is in the same magnitude of experimental density.[50, 218] By means of the climbing image nudge elastic band (CINEB) method, we investigated the minimum energy paths for O_2 chemisorption and dissociation on defective MoS_2 and further performed properties calculation for all the stable intermediate and final states. Our band structure calculations suggested that the chemisorption and dissociation of O_2 on the defective surface tended to passivate the S defect state and restore the band structure and optical absorption spectrum of pristine MoS_2 due to the isovalence between O^{2-} (or O_2^{2-}) and S^{2-}. Furthermore, the physisorption of O_2 on the defective and pristine MoS_2 could enhance the optical absorption peak and the excitonic binding energy. More specifically, the strengthened optical absorption observed from the experiment was related to the physisorption of O_2 on the MoS_2 monolayer. The work further explained the mechanism of the enhanced optical peaks upon O_2 adsorption.

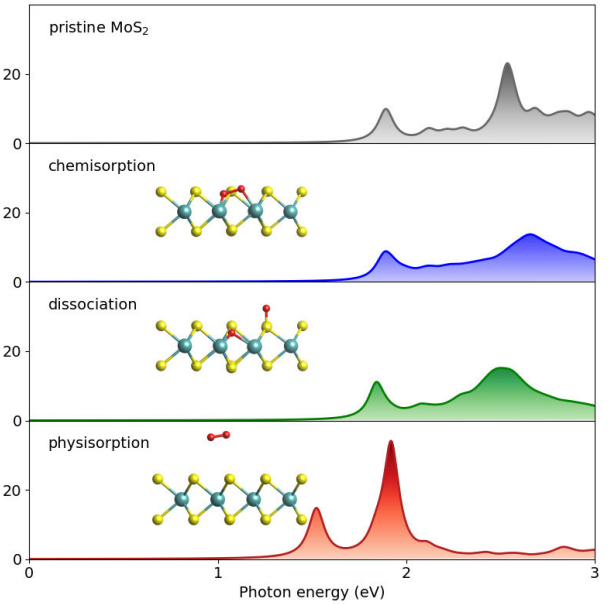

Figure 4.4: Optical absorption spectra of part systems considered in this work.

Paper M5. Besides O_2, the adsorption of other small molecules on MoS_2 also attracted much attention. For example, the MoS_2 field-effect transistor had been experimentally realized to detect NO[219]. Yet, the influences of NO on the optical and excitonic properties of MoS_2 had not been explored in previous study. Hence, studying the adsorption characteristics of NO molecule can facilitate its applications in reality. In this study, we systematically studied the electronic and optical properties of monolayer MoS_2 functionalized by NO and further extend the system to small aromatic molecule $C_3H_3N_3$. We mainly focused on the combining effect of molecular functionalization and defective engineering on the excitonic properties of MoS_2. Band structure calculations showed that the adsorption of NO introduced adsorption states into the band gap of both pristine and defective MoS_2, while the adsorption of $C_3H_3N_3$ had no significant effect on the band gap of the MoS_2 monolayer. Combining the band structure with the optical absorption spectrum, we found the hole–electron interaction of the exciton was weakened upon the NO adsorbed on the pristine surface due to the interaction between the excitonic dipole and the unpaired electron; while concerning the defective surface, the NO molecule was

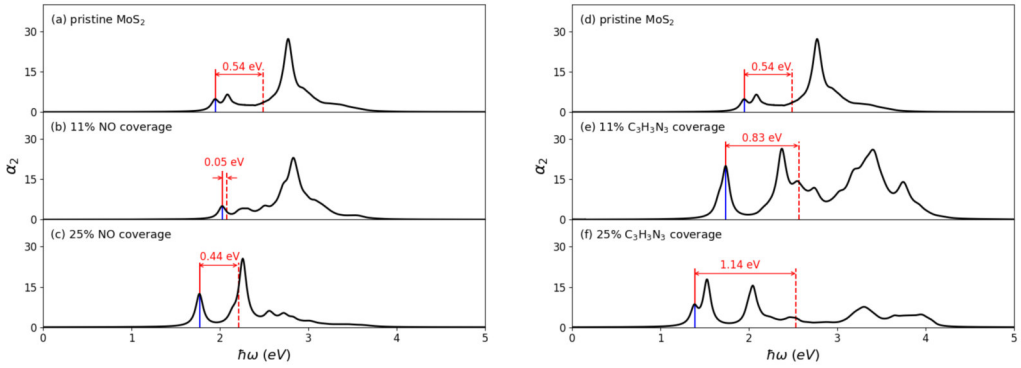

Figure 4.5: Optical absorption spectra (BSE) of NO (left) and $C_3H_3N_3$ (right) adsorbed on pristine MoS_2 monolayer with 11% and 25% molecular coverage. The blue vertical lines indicate the optical absorption intensity corresponding to the first absorption peak. Red dashed lines indicate the electronic band gap. Exciton binding energies are shown as well.

chemically bonded onto the S defect to tune the optical absorption and excitons of MoS_2. In addition, $C_3H_3N_3$ could dramatically strengthen the hole–electron interaction of the exciton for both pristine and defective surfaces via the interaction between the excitonic and the molecular dipole.

Overall, the purpose of this thesis was to explore the tunability of different functionalization methods on 2D materials. The results confirmed that the stacking was an effective method to tune the moiré superstructure and electronic properties of graphene, and indicated that the intercalation mechanism could be controlled by the concentration of alloy; the covalent functionalization was a direct method to control the properties of 2D as it bonded with the surface by chemical interaction and the modulation of electronic band gap and optical absorption exhibited a strong dependence on the functionalization coverage, which offered the prospect that if the coverage of covalent functionalization on the substrate is controlled, the band gap and optical adsorption can be artificially tuned; the defect on the MoS_2 acted as adsorption site for molecules, which provided more opportunity to change the properties of 2D materials by doping. Our theoretical investigations of the tunable electronic and optical properties of graphene and MoS_2 provide a guide for further experimental study and bring opportunities to build novel optoelectric devices from these synthesized 2D materials.

Bibliography

[1] C. Kumar, S. Das, S. Jit. In *2D Nanoscale Heterostructured Materials*, (Eds.: S. Jit, S. Das), Micro and Nano Technologies, Elsevier, **2020**, pp. 195–214.

[2] M. Zeng, Y. Xiao, J. Liu, K. Yang, L. Fu. *Chem. Rev.* **2018**, *118*, 6236–6296.

[3] L. M. Xie. *Nanoscale* **2015**, *7*, 18392–18401.

[4] K. S. Novoselov, A. K. Geim, S. V. Morozov, D. Jiang, Y. Zhang, S. V. Dubonos, I. V. Grigorieva, A. A. Firsov. *Science* **2004**, *306*, 666–669.

[5] H. Zhou, J. Zhu, Z. Liu, Z. Yan, X. Fan, J. Lin, G. Wang, Q. Yan, T. Yu, P. M. Ajayan, J. M. Tour. *Nano Res.* **2014**, *7*, 1232–1240.

[6] M. Ahmadi, O. Zabihi, S. Jeon, M. Yoonessi, A. Dasari, S. Ramakrishna, M. Naebe. *J. Mater. Chem. A* **2020**, *8*, 845–883.

[7] M. Naguib, V. N. Mochalin, M. W. Barsoum, Y. Gogotsi. *Adv. Mater.* **2014**, *26*, 992–1005.

[8] N. Mounet, M. Gibertini, P. Schwaller, D. Campi, A. Merkys, A. Marrazzo, T. Sohier, I. E. Castelli, A. Cepellotti, G. Pizzi, N. Marzari. *Nat. Nanotechnol.* **2018**, *13*, 246–252.

[9] S. Manzeli, D. Ovchinnikov, D. Pasquier, O. V. Yazyev, A. Kis. *Nat. Rev. Mater.* **2017**, *2*, 17033.

[10] C. Tan, X. Cao, X.-J. Wu, Q. He, J. Yang, X. Zhang, J. Chen, W. Zhao, S. Han, G.-H. Nam, M. Sindoro, H. Zhang. *Chem. Rev.* **2017**, *117*, 6225–6331.

[11] L. Liu, Y. P. Feng, Z. X. Shen. *Phys. Rev. B* **2003**, *68*, 104102.

[12] L.-D. Zhao, S.-H. Lo, Y. Zhang, H. Sun, G. Tan, C. Uher, C. Wolverton, V. P. Dravid, M. G. Kanatzidis. *Nature* **2014**, *508*, 373–377.

[13] R. Fei, A. Faghaninia, R. Soklaski, J.-A. Yan, C. Lo, L. Yang. *Nano Lett.* **2014**, *14*, 6393–6399.

[14] M.-J. Lee, J.-H. Ahn, J. Sung, H. Heo, S. Jeon, W. Lee, J. Song, K.-H. Hong, B. Choi, S.-H. Lee, M.-H. Jo. *Nat. Commun.* **2016**, *7*, 12011.

[15] N. Huo, G. Konstantatos. *Nat. Commun.* **2017**, *8*, 572.

[16] Y. Xu, J. Yuan, K. Zhang, Y. Hou, Q. Sun, Y. Yao, S. Li, Q. Bao, H. Zhang, Y. Zhang. *Adv. Funct. Mater.* **2017**, *27*, 1702211.

[17] P. Yang, Z. Zhang, M. Sun, F. Lin, T. Cheng, J. Shi, C. Xie, Y. Shi, S. Jiang, Y. Huan, P. Liu, F. Ding, C. Xiong, D. Xie, Y. Zhang. *ACS Nano* **2019**, *13*, 3649–3658.

[18] Y. Zhang, C.-K. Lim, Z. Dai, G. Yu, J. W. Haus, H. Zhang, P. N. Prasad. *Phys. Rep.* **2019**, *795*, 1–51.

[19] D. Deng, K. S. Novoselov, Q. Fu, N. Zheng, Z. Tian, X. Bao. *Nat. Nanotechnol.* **2016**, *11*, 218–230.

[20] B. Mendoza-Sánchez, Y. Gogotsi. *Adv. Mater.* **2016**, *28*, 6104–6135.

[21] H. C. Lee, W.-W. Liu, S.-P. Chai, A. R. Mohamed, A. Aziz, C.-S. Khe, N. M. S. Hidayah, U. Hashim. *RSC Adv.* **2017**, *7*, 15644–15693.

[22] M. Sang, J. Shin, K. Kim, K. J. Yu. *Nanomaterials* **2019**, *9*, 374.

[23] A. A. Balandin. *Nat. Mater.* **2011**, *10*, 569–581.

[24] S. Chen, A. L. Moore, W. Cai, J. W. Suk, J. An, C. Mishra, C. Amos, C. W. Magnuson, J. Kang, L. Shi, R. S. Ruoff. *ACS Nano* **2011**, *5*, 321–328.

[25] S. Chen, Q. Wu, C. Mishra, J. Kang, H. Zhang, K. Cho, W. Cai, A. A. Balandin, R. S. Ruoff. *Nat. Mater.* **2012**, *11*, 203–207.

[26] M. D. Stoller, S. Park, Y. Zhu, J. An, R. S. Ruoff. *Nano Lett.* **2008**, *8*, 3498–3502.

[27] C. Lee, X. Wei, J. Kysar, J. Hone. *Science* **2008**, *321*, 385–388.

[28] R. R. Nair, P. Blake, A. N. Grigorenko, K. S. Novoselov, T. J. Booth, T. Stauber, N. M. R. Peres, A. K. Geim. *Science* **2008**, *320*, 1308–1308.

[29] R. Kumar, G. Rajasekaran, A. Parashar. *Nanotechnology* **2016**, *27*, 085706.

[30] D. Wickramaratne, L. Weston, C. G. Van de Walle. *J. Phys. Chem. C* **2018**, *122*, 25524–25529.

[31] H. H. Huang, X. Fan, D. J. Singh, W. T. Zheng. *Nanoscale* **2020**, *12*, 1247–1268.

[32] K. F. Mak, C. Lee, J. Hone, J. Shan, T. F. Heinz. *Phys. Rev. Lett.* **2010**, *105*, 136805.

[33] A. Splendiani, L. Sun, Y. Zhang, T. Li, J. Kim, C.-Y. Chim, G. Galli, F. Wang. *Nano Lett.* **2010**, *10*, 1271–1275.

[34] H. R. Gutiérrez, N. Perea-López, A. L. Elías, A. Berkdemir, B. Wang, R. Lv, F. López-Urías, V. H. Crespi, H. Terrones, M. Terrones. *Nano Lett.* **2013**, *13*, 3447–3454.

[35] A. R. Klots, A. K. M. Newaz, B. Wang, D. Prasai, H. Krzyzanowska, D. Caudel, N. J. Ghimire, J.-Q. Yan, B. L. Ivanov, K. A. Velizhanin, A. Burger, D. G. Mandrus, N. H. Tolk, S. T. Pantelides, K. I. Bolotin. *Sci. Rep.* **2014**, *4*, 6608.

[36] B. Zhu, X. Chen, X. Cui. *Sci. Rep.* **2014**, *5*, 9218.

[37] Z. Ye, T. Cao, K. O'Brien, H. Zhu, X. Yin, Y. Wang, S. G. Louie, X. Zhang. *Nature* **2014**, *513*, 214–218.

[38] K. He, N. Kumar, L. Zhao, Z. Wang, K. F. Mak, H. Zhao, J. Shan. *Phys. Rev. Lett.* **2014**, *113*, 026803.

[39] D. Y. Qiu, F. H. da Jornada, S. G. Louie. *Phys. Rev. Lett.* **2013**, *111*, 216805.

[40] J. S. Ross, S. Wu, H. Yu, N. J. Ghimire, A. M. Jones, G. Aivazian, J.-Q. Yan, D. G. Mandrus, D. Xiao, W. Yao, X. Xu. *Nat. Commun.* **2013**, *4*, 1474.

[41] Z. Wu, Z. Ni. *Nanophotonics* **2017**, *6*, 1219–1237.

[42] S. Wang, A. Robertson, J. H. Warner. *Chem. Soc. Rev.* **2018**, *47*, 6764–6794.

[43] W. Zhou, X. Zou, S. Najmaei, Z. Liu, Y. Shi, J. Kong, J. Lou, P. M. Ajayan, B. I. Yakobson, J.-C. Idrobo. *Nano Lett.* **2013**, *13*, 2615–2622.

[44] D. Liu, Y. Guo, L. Fang, J. Robertson. *Appl. Phys. Lett.* **2013**, *103*, 183113.

[45] J.-Y. Noh, H. Kim, Y.-S. Kim. *Phys. Rev. B* **2014**, *89*, 205417.

[46] H.-P. Komsa, A. V. Krasheninnikov. *Phys. Rev. B* **2015**, *91*, 125304.

[47] B. Mortazavi, S. Ahzi. *Carbon* **2013**, *63*, 460–470.

[48] Y. Wei, J. Wu, H. Yin, X. Shi, R. Yang, M. Dresselhaus. *Nat. Mater.* **2012**, *11*, 759–763.

[49] G.-H. Lee, R. C. Cooper, S. J. An, S. Lee, A. van der Zande, N. Petrone, A. G. Hammerberg, C. Lee, B. Crawford, W. Oliver, J. W. Kysar, J. Hone. *Science* **2013**, *340*, 1073–1076.

[50] H. Qiu, T. Xu, Z. Wang, W. Ren, H. Nan, Z. Ni, Q. Chen, S. Yuan, F. Miao, F. Song, G. Long, Y. Shi, L. Sun, J. Wang, X. Wang. *Nat. Commun.* **2013**, *4*, 2642.

[51] J. Xie, X. Yang, Y. Xie. *Nanoscale* **2020**, *12*, 4283–4294.

[52] X. Yan, L. Zhuang, Z. Zhu, X. Yao. *Nanoscale* **2021**, *13*, 3327–3345.

[53] J. Azadmanjiri, P. Kumar, V. K. Srivastava, Z. Sofer. *ACS Appl. Nano Mater.* **2020**, *3*, 3116–3143.

[54] P. M. M. C. de Melo, Z. Zanolli, M. J. Verstraete. *Adv. Quantum Technol.* **2021**, *4*, 2000118.

[55] A. Ramasubramaniam, D. Naveh. *Phys. Rev. B* **2013**, *87*, 195201.

[56] R. Mishra, W. Zhou, S. J. Pennycook, S. T. Pantelides, J.-C. Idrobo. *Phys. Rev. B* **2013**, *88*, 144409.

[57] J. Jiang, T. Xu, J. Lu, L. Sun, Z. Ni. *Research* **2019**, *2019*.

[58] A. Di Bartolomeo. *Phys. Rep.* **2016**, *606*, 1–58.

[59] S. Gharibzadeh, I. M. Hossain, P. Fassl, B. A. Nejand, T. Abzieher, M. Schultes, E. Ahlswede, P. Jackson, M. Powalla, S. Schäfer, M. Rienäcker, T. Wietler, R. Peibst, U. Lemmer, B. S. Richards, U. W. Paetzold. *Adv. Funct. Mater.* **2020**, *30*, 1909919.

[60] J.-S. Chen, T. L. Doane, M. Li, H. Zang, M. M. Maye, M. Cotlet. *Part. Part. Syst. Charact.* **2018**, *35*, 1700310.

[61] L. D. N. Mouafo, F. Godel, L. Simon, Y. J. Dappe, W. Baaziz, U. N. Noumbé, E. Lorchat, M.-B. Martin, S. Berciaud, B. Doudin, O. Ersen, B. Dlubak, P. Seneor, J.-F. Dayen. *Adv. Funct. Mater.* **2021**, *31*, 2008255.

[62] Z. Lu, D. Liang, X. Ping, L. Xing, Z. Wang, L. Wu, P. Lu, L. Jiao. *Small* **2020**, *16*, 2004296.

[63] H. Lim, S. I. Yoon, G. Kim, A.-R. Jang, H. S. Shin. *Chem. Mater.* **2014**, *26*, 4891–4903.

[64] M.-Y. Li, C.-H. Chen, Y. Shi, L.-J. Li. *Mater. Today* **2016**, *19*, 322–335.

[65] C. R. Dean, A. F. Young, I. Meric, C. Lee, L. Wang, S. Sorgenfrei, K. Watanabe, T. Taniguchi, P. Kim, K. L. Shepard, J. Hone. *Nat. Nanotechnol.* **2010**, *5*, 722–726.

[66] T. Ando. *J. Phys. Soc. Japan* **2006**, *75*, 4716.

[67] J.-H. Chen, C. Jang, S. Xiao, M. Ishigami, M. S. Fuhrer. *Nat. Nanotechnol.* **2008**, *3*, 206–209.

[68] S. V. Morozov, K. S. Novoselov, M. I. Katsnelson, F. Schedin, D. C. Elias, J. A. Jaszczak, A. K. Geim. *Phys. Rev. Lett.* **2008**, *100*, 016602.

[69] W. Gannett, W. Regan, K. Watanabe, T. Taniguchi, M. F. Crommie, A. Zettl. *Appl. Phys. Lett.* **2011**, *98*, 242105.

[70] S. Bae, H. Kim, Y. Lee, X. Xu, J.-S. Park, Y. Zheng, J. Balakrishnan, T. Lei, H. R. Kim, Y. Song, Y.-J. Kim, K. S. Kim, B. Ozyilmaz, J.-H. Ahn, B. H. Hong, S. Iijima. *Nat. Nanotechnol.* **2010**, *5*, 574–578.

[71] J. Ryu, Y. Kim, D. Won, N. Kim, J. S. Park, E.-K. Lee, D. Cho, S.-P. Cho, S. J. Kim, G. H. Ryu, H.-A. Shin, Z. Lee, B. H. Hong, S. Cho. *ACS Nano* **2014**, *8*, 950–956.

[72] I. Pletikosi ć, M. Kralj, P. Pervan, R. Brako, J. Coraux, A. T. N'Diaye, C. Busse, T. Michely. *Phys. Rev. Lett.* **2009**, *102*, 056808.

[73] S. Gottardi, K. Müller, L. Bignardi, J. C. Moreno-López, T. A. Pham, O. Ivashenko, M. Yablonskikh, A. Barinov, J. Björk, P. Rudolf, M. Stöhr. *Nano Lett.* **2015**, *15*, 917–922.

[74] I. I. Klimovskikh, M. M. Otrokov, V. Y. Voroshnin, D. Sostina, L. Petaccia, G. Di Santo, S. Thakur, E. V. Chulkov, A. M. Shikin. *ACS Nano* **2017**, *11*, 368–374.

[75] D. Eom, D. Prezzi, K. T. Rim, H. Zhou, M. Lefenfeld, S. Xiao, C. Nuckolls, M. S. Hybertsen, T. F. Heinz, G. W. Flynn. *Nano Lett.* **2009**, *9*, 2844–2848.

[76] G. Bertoni, L. Calmels, A. Altibelli, V. Serin. *Phys. Rev. B* **2005**, *71*, 075402.

[77] S. Marchini, S. Günther, J. Wintterlin. *Phys. Rev. B* **2007**, *76*, 075429.

[78] Y. Gong, J. Lin, X. Wang, G. Shi, S. Lei, Z. Lin, X. Zou, G. Ye, R. Vajtai, B. I. Yakobson, H. Terrones, M. Terrones, B. K. Tay, J. Lou, S. T. Pantelides, Z. Liu, W. Zhou, P. M. Ajayan. *Nat. Mater.* **2014**, *13*, 1135–1142.

[79] H. Chen, X. Wen, J. Zhang, T. Wu, Y. Gong, X. Zhang, J. Yuan, C. Yi, J. Lou, P. M. Ajayan, W. Zhuang, G. Zhang, J. Zheng. *Nat. Commun.* **2016**, *7*, 12512.

[80] Y. Zhu, S. Murali, W. Cai, X. Li, J. W. Suk, J. R. Potts, R. S. Ruoff. *Adv. Mater.* **2010**, *22*, 3906–3924.

[81] X. Zhang, Y. Feng, P. Lv, Y. Shen, W. Feng. *Langmuir* **2010**, *26*, 18508–18511.

[82] R.-C. Wang, Y.-C. Chen, S.-J. Chen, Y.-M. Chang. *Carbon* **2014**, *70*, 215–223.

[83] E. Bekyarova, M. E. Itkis, P. Ramesh, C. Berger, M. Sprinkle, W. A. de Heer, R. C. Haddon. *J. Am. Chem. Soc.* **2009**, *131*, 1336–1337.

[84] J. M. Englert, C. Dotzer, G. Yang, M. Schmid, C. Papp, J. M. Gottfried, H.-P. Steinrück, E. Spiecker, A. Hirsch. *Nat. Chem.* **2011**, *3*, 279–286.

[85] L.-H. Liu, M. M. Lerner, M. Yan. *Nano Lett.* **2010**, *10*, 3754–3756.

[86] L.-H. Liu, M. Yan. *J. Mater. Chem.* **2011**, *21*, 3273–3276.

[87] H. Ismaili, D. Geng, A. X. Sun, T. T. Kantzas, M. S. Workentin. *Langmuir* **2011**, *27*, 13261–13268.

[88] D. M. Sim, M. Kim, S. Yim, M.-J. Choi, J. Choi, S. Yoo, Y. S. Jung. *ACS Nano* **2015**, *9*, 12115–12123.

[89] S. Presolski, M. Pumera. *Mater. Today* **2016**, *19*, 140–145.

[90] Q. Ding, K. J. Czech, Y. Zhao, J. Zhai, R. J. Hamers, J. C. Wright, S. Jin. *ACS Appl. Mater. Interfaces* **2017**, *9*, 12734–12742.

[91] S. Bertolazzi, S. Bonacchi, G. Nan, A. Pershin, D. Beljonne, P. Samorì. *Adv. Mater.* **2017**, *29*, 1606760.

[92] M. Vera-Hidalgo, E. Giovanelli, C. Navío, E. M. Pérez. *J. Am. Chem. Soc.* **2019**, *141*, 3767–3771.

[93] X. S. Chu, A. Yousaf, D. O. Li, A. A. Tang, A. Debnath, D. Ma, A. A. Green, E. J. G. Santos, Q. H. Wang. *Chem. Mater.* **2018**, *30*, 2112–2128.

[94] D. O. Li, X. S. Chu, Q. H. Wang. *Langmuir* **2019**, *35*, 5693–5701.

[95] D. Voiry, A. Goswami, R. Kappera, C. De Carvalho Castro e Silva, D. Kaplan, T. Fujita, M. Chen, T. Asefa, M. Chhowalla. *Nat. Chem.* **2014**, *7*, 45–49.

[96] J. T. Robinson, J. S. Burgess, C. E. Junkermeier, S. C. Badescu, T. L. Reinecke, F. K. Perkins, M. K. Zalalutdniov, J. W. Baldwin, J. C. Culbertson, P. E. Sheehan, E. S. Snow. *Nano Lett.* **2010**, *10*, 3001–3005.

[97] S. Karunakaran, S. Pandit, B. Basu, M. De. *J. Am. Chem. Soc.* **2018**, *140*, 12634–12644.

[98] Z. Zhang, H. Huang, X. Yang, L. Zang. *J. Phys. Chem. Lett.* **2011**, *2*, 2897–2905.

[99] J. M. P. Alaboson, Q. H. Wang, J. D. Emery, A. L. Lipson, M. J. Bedzyk, J. W. Elam, M. J. Pellin, M. C. Hersam. *ACS Nano* **2011**, *5*, 5223–5232.

[100] K. Yang, W. D. Xiao, Y. H. Jiang, H. G. Zhang, L. W. Liu, J. H. Mao, H. T. Zhou, S. X. Du, H.-J. Gao. *J. Phys. Chem. C* **2012**, *116*, 14052–14056.

[101] F. Schulz, R. Drost, S. K. Hämäläinen, P. Liljeroth. *ACS Nano* **2013**, *7*, 11121–11128.

[102] A. R. Brill, M. K. Kuntumalla, G. de Ruiter, E. Koren. *ACS Appl. Mater. Interfaces* **2020**, *12*, 33941–33949.

[103] X. Dong, Y. Shi, Y. Zhao, D. Chen, J. Ye, Y. Yao, F. Gao, Z. Ni, T. Yu, Z. Shen, Y. Huang, P. Chen, L.-J. Li. *Phys. Rev. Lett.* **2009**, *102*, 135501.

[104] S. M. Kozlov, F. Viñes, A. Görling. *Adv. Mater.* **2011**, *23*, 2638–2643.

[105] D. Sim, D. Liu, X. Dong, N. Xiao, S. Li, Y. Zhao, L.-J. Li, Q. Yan, H. H. Hng. *J. Phys. Chem. C* **2011**, *115*, 1780–1785.

[106] H. Yoo, K. Heo, M. H. R. Ansari, S. Cho. *Nanomaterials* **2021**, *11*, 832.

[107] Y. Li, C.-Y. Xu, P. Hu, L. Zhen. *ACS Nano* **2013**, *7*, 7795–7804.

[108] W. H. Lee, Y. D. Park. *Adv. Mater. Interfaces* **2018**, *5*, 1700316.

[109] D.-H. Kang, J. Shim, S. K. Jang, J. Jeon, M. H. Jeon, G. Y. Yeom, W.-S. Jung, Y. H. Jang, S. Lee, J.-H. Park. *ACS Nano* **2015**, *9*, 1099–1107.

[110] T. Chu, H. Ilatikhameneh, G. Klimeck, R. Rahman, Z. Chen. *Nano Lett.* **2015**, *15*, 8000–8007.

[111] A. Ramasubramaniam, D. Naveh, E. Towe. *Phys. Rev. B* **2011**, *84*, 205325.

[112] K. F. Mak, K. He, C. Lee, G. H. Lee, J. Hone, T. F. Heinz, J. Shan. *Nat. Mater.* **2012**, *12*, 207–211.

[113] S. Yang, Y. Chen, C. Jiang. *InfoMat* **2021**, *3*, 397–420.

[114] Y. Sun, K. Liu. *J. Appl. Phys.* **2019**, *125*, 082402.

[115] S. Manzeli, A. Allain, A. Ghadimi, A. Kis. *Nano Lett.* **2015**, *15*, 5330–5335.

[116] H. Li, A. W. Contryman, X. Qian, S. M. Ardakani, Y. Gong, X. Wang, J. M. Weisse, C. H. Lee, J. Zhao, P. M. Ajayan, J. Li, H. C. Manoharan, X. Zheng. *Nat. Commun.* **2015**, *6*, 7381.

[117] Y. Kuang, L. Lindsay, B. Huang. *Nano Lett.* **2015**, *15*, 6121–6127.

[118] E. Schrödinger. *Phys. Rev.* **1926**, *28*, 1049–1070.

[119] M. Born, R. Oppenheimer. *Ann. Phys.* **1927**, *389*, 457–484.

[120] W. Pauli. *Z. Phys.* **1925**, *31*, 765–783.

[121] J. C. Slater. *Phys. Rev.* **1929**, *34*, 1293–1322.

[122] C. C. J. Roothaan. *Rev. Mod. Phys.* **1951**, *23*, 69–89.

[123] C. Møller, M. S. Plesset. *Phys. Rev.* **1934**, *46*, 618–622.

[124] C. David Sherrill, H. F. Schaefer. Advances in Quantum Chemistry **1999**, *34*, (Eds.: P.-O. Löwdin, J. R. Sabin, M. C. Zerner, E. Brändas), 143–269.

[125] P. Hohenberg, W. Kohn. *Phys. Rev.* **1964**, *136*, B864–B871.

[126] W. Kohn, L. J. Sham. *Phys. Rev.* **1965**, *140*, A1133–A1138.

[127] M. Levy. *Proc. Nat. Acad. Sci. U.S.A.* **1979**, *76*, 6062–6065.

[128] P. A. M. Dirac. *Math. Proc. Cambridge Philos. Soc.* **1930**, *26*, 376–385.

[129] M. Gell-Mann, K. A. Brueckner. *Phys. Rev.* **1957**, *106*, 364–368.

[130] D. M. Ceperley, B. J. Alder. *Phys. Rev. Lett.* **1980**, *45*, 566–569.

[131] C. Lee, D. Vanderbilt, K. Laasonen, R. Car, M. Parrinello. *Phys. Rev. B* **1993**, *47*, 4863–4872.

[132] J. A. Wilson, A. D. Yoffe. *Adv. Phys.* **1969**, *18*, 193–335.

[133] J. P. Perdew, W. Yue. *Phys. Rev. B* **1986**, *33*, 8800–8802.

[134] J. P. Perdew, K. Burke, M. Ernzerhof. *Phys. Rev. Lett.* **1996**, *77*, 3865–3868.

[135] K. Burke, J. P. Perdew, Y. Wang. In *Electronic Density Functional Theory: Recent Progress and New Directions*, (Eds.: J. F. Dobson, G. Vignale, M. P. Das), Springer US, Boston, MA, **1998**, pp. 81–111.

[136] C. Lee, W. Yang, R. G. Parr. *Phys. Rev. B* **1988**, *37*, 785–789.

[137] J. P. Perdew. *Phys. Rev. B* **1986**, *33*, 8822–8824.

[138] V. N. Staroverov, G. E. Scuseria, J. Tao, J. P. Perdew. *Phys. Rev. B* **2004**, *69*, 075102.

[139] Y. Zhang, W. Yang. *Phys. Rev. Lett.* **1998**, *80*, 890–890.

[140] M. Filatov, W. Thiel. *Phys. Rev. A* **1998**, *57*, 189–199.

[141] T. Van Voorhis, G. E. Scuseria. *J. Chem. Phys.* **1998**, *109*, 400–410.

[142] M. Ernzerhof, G. E. Scuseria. *J. Chem. Phys.* **1999**, *111*, 911–915.

[143] J. P. Perdew, M. Ernzerhof, K. Burke. *J. Chem. Phys.* **1996**, *105*, 9982–9985.

[144] C. Adamo, V. Barone. *J. Chem. Phys.* **1999**, *110*, 6158–6170.

[145] R. J.-M. Pellenq, D. Nicholson. *Mol. Phys.* **1998**, *95*, 549–570.

[146] S. Grimme. *J. Comput. Chem.* **2004**, *25*, 1463–1473.

[147] S. Grimme. *J. Comput. Chem.* **2006**, *27*, 1787–1799.

[148] S. Grimme, J. Antony, S. Ehrlich, H. Krieg. *J. Chem. Phys.* **2010**, *132*, 154104.

[149] J. R. Reimers, M. J. Ford, L. Goerigk. *Mol. Simul.* **2016**, *42*, 494–510.

[150] M. Dion, H. Rydberg, E. Schröder, D. C. Langreth, B. I. Lundqvist. *Phys. Rev. Lett.* **2004**, *92*, 246401.

[151] K. Lee, É. D. Murray, L. Kong, B. I. Lundqvist, D. C. Langreth. *Phys. Rev. B* **2010**, *82*, 081101.

[152] A. Puzder, M. Dion, D. C. Langreth. *J. Chem. Phys.* **2006**, *124*, 164105.

[153] K. Berland, V. R. Cooper, K. Lee, E. Schröder, T. Thonhauser, P. Hyldgaard, B. I. Lundqvist. *Rep. Prog. Phys.* **2015**, *78*, 066501.

[154] K. Berland, P. Hyldgaard. *Phys. Rev. B* **2014**, *89*, 035412.

[155] J. Harl, G. Kresse. *Phys. Rev. B* **2008**, *77*, 045136.

[156] A. Grüneis, M. Marsman, J. Harl, L. Schimka, G. Kresse. *J. Chem. Phys.* **2009**, *131*, 154115.

[157] T. Koopmans. *Physica* **1934**, *1*, 104–113.

[158] J. P. Perdew, M. Levy. *Phys. Rev. Lett.* **1983**, *51*, 1884–1887.

[159] L. J. Sham, M. Schlüter. *Phys. Rev. Lett.* **1983**, *51*, 1888–1891.

[160] L. J. Sham, M. Schlüter. *Phys. Rev. B* **1985**, *32*, 3883–3889.

[161] M. Kuisma, J. Ojanen, J. Enkovaara, T. T. Rantala. *Phys. Rev. B* **2010**, *82*, 115106.

[162] O. V. Gritsenko, R. V. Leeuwen, E. J. Baerends. *Int. J. Quantum Chem.* **1997**, *61*, 231–243.

[163] F. Hüser, T. Olsen, K. S. Thygesen. *Phys. Rev. B* **2013**, *87*, 235132.

[164] S. H., M. Strange, M. Pandey, T. Deilmann, P. S. Schmidt, N. F. Hinsche, M. N. Gjerding, D. Torelli, P. M. Larsen, A. C. Riis-Jensen, J. Gath, K. W. Jacobsen, J. J. Mortensen, T. Olsen, K. S. Thygesen. *2D Mater.* **2018**, *5*, 042002.

[165] J. Yan, K. W. Jacobsen, K. S. Thygesen. *Phys. Rev. B* **2012**, *86*, 045208.

[166] A. Patra, S. Jana, P. Samal, F. Tran, L. Kalantari, J. Doumont, P. Blaha. *J. Phys. Chem. C* **2021**, *125*, 11206–11215.

[167] M. Shishkin, G. Kresse. *Phys. Rev. B* **2007**, *75*, 235102.

[168] G. Cassabois, P. Valvin, B. Gil. *Nat. Photonics* **2016**, *10*, 262–266.

[169] M. Akhtar, G. Anderson, R. Zhao, A. Alruqi, J. Mroczkowska, G. Sumanasekera, J. Jasinski. *npj 2D Mater. Appl.* **2017**, *1*, 5.

[170] G. Stefanucci, R. van Leeuwen. *Nonequilibrium Many-Body Theory of Quantum Systems: A Modern Introduction*, Cambridge University Press, **2013**.

[171] R. D. Mattuck. *A Guide to Feynman Diagrams in the Many-body Problem*, Dover Publications, **1992**.

[172] H. Lehmann. *Il Nuovo Cimento* **1954**, *11*, 342–357.

[173] L. Hedin. *Phys. Rev.* **1965**, *139*, A796–A823.

[174] X. Blase, I. Duchemin, D. Jacquemin, P.-F. Loos. *J. Phys. Chem. Lett.* **2020**, *11*, 7371–7382.

[175] R. Kubo. *J. Phys. Soc. Japan* **1957**, *12*, 570–586.

[176] H. Kuzmany. In *Solid-State Spectroscopy: An Introduction*, Springer Berlin Heidelberg, Berlin, Heidelberg, **1998**, pp. 101–120.

[177] F. A. Rasmussen. *PhD thesis* **2016**.

[178] E. E. Salpeter, H. A. Bethe. *Phys. Rev.* **1951**, *84*, 1232–1242.

[179] G. Onida, L. Reining, A. Rubio. *Rev. Mod. Phys.* **2002**, *74*, 601–659.

[180] M. C. Payne, M. P. Teter, D. C. Allan, T. A. Arias, J. D. Joannopoulos. *Rev. Mod. Phys.* **1992**, *64*, 1045–1097.

[181] A. W. Götz. In *Electronic Structure Calculations on Graphics Processing Units*, John Wiley Sons, Ltd, **2016**, Chapter 3, pp. 39–66.

[182] J. C. Slater. *Phys. Rev.* **1937**, *51*, 846–851.

[183] D. D. Koelling, G. O. Arbman. *J. Phys. F: Met. Phys.* **1975**, *5*, 2041–2054.

[184] G. K. H. Madsen, P. Blaha, K. Schwarz, E. Sjöstedt, L. Nordström. *Phys. Rev. B* **2001**, *64*, 195134.

[185] K. Schwarz, P. Blaha, G. K. H. Madsen. *Comput. Phys. Commun.* **2002**, *147*, 71–76.

[186] D. Golze, M. Dvorak, P. Rinke. *Front. Chem.* **2019**, *7*, 377.

[187] J. C. Phillips. *Phys. Rev.* **1958**, *112*, 685–695.

[188] J. D. Weeks, S. A. Rice. *J. Chem. Phys.* **1968**, *49*, 2741–2755.

[189] P. E. Blöchl. *Phys. Rev. B* **1994**, *50*, 17953–17979.

[190] C. A. Rozzi, D. Varsano, A. Marini, E. K. U. Gross, A. Rubio. *Phys. Rev. B* **2006**, *73*, 205119.

[191] F. Hüser, T. Olsen, K. S. Thygesen. *Phys. Rev. B* **2013**, *88*, 245309.

[192] F. A. Rasmussen, P. S. Schmidt, K. T. Winther, K. S. Thygesen. *Phys. Rev. B* **2016**, *94*, 155406.

[193] C. Zhang, H. Wang, W. Chan, C. Manolatou, F. Rana. *Phys. Rev. B* **2014**, *89*, 205436.

[194] C. Vorwerk, B. Aurich, C. Cocchi, C. Draxl. *Electronic Structure* **2019**, *1*, 037001.

[195] S. Latini. *PhD thesis* **2016**.

[196] J. B. Goodenough. *Phys. Rev.* **1968**, *171*, 466–479.

[197] J. Knoester, V. M. Agranovich. In *Electronic Excitations in Organic Nanostructures*, Thin Films and Nanostructures, Academic Press, **2003**, pp. 1–96.

[198] Z. Jiang, Z. Liu, Y. Li, W. Duan. *Phys. Rev. Lett.* **2017**, *118*, 266401.

[199] M. Feierabend. *PhD thesis* **2018**.

[200] X. Zheng, X. Zhang. In *Advances in Condensed-Matter and Materials Physics - Rudimentary Research to Topical Technology*, **2020**.

[201] K. Wang, B. Huang, M. Tian, F. Ceballos, M.-W. Lin, M. Mahjouri-Samani, A. Boulesbaa, A. A. Puretzky, C. M. Rouleau, M. Yoon, H. Zhao, K. Xiao, G. Duscher, D. B. Geohegan. *ACS Nano* **2016**, *10*, 6612–6622.

[202] L. Li, W. Zheng, C. Ma, H. Zhao, F. Jiang, Y. Ouyang, B. Zheng, X. Fu, P. Fan, M. Zheng, Y. Li, Y. Xiao, W. Cao, Y. Jiang, X. Zhu, X. Zhuang, A. Pan. *Nano Lett.* **2020**, *20*, 3361–3368.

[203] F. Ceballos, M. Z. Bellus, H.-Y. Chiu, H. Zhao. *ACS Nano* **2014**, *8*, 12717–12724.

[204] D. H. Luong, H. S. Lee, G. P. Neupane, S. Roy, G. Ghimire, J. H. Lee, Q. A. Vu, Y. H. Lee. *Adv. Mater.* **2017**, *29*, 1701512.

[205] H. Heo, J. H. Sung, S. Cha, B.-G. Jang, J.-Y. Kim, G. Jin, D. Lee, J.-H. Ahn, M.-J. Lee, J. H. Shim, H. Choi, M.-H. Jo. *Nat. Commun.* **2015**, *6*, 7372.

[206] S. Tongay, W. Fan, J. Kang, J. Park, U. Koldemir, J. Suh, D. S. Narang, K. Liu, J. Ji, J. Li, R. Sinclair, J. Wu. *Nano Lett.* **2014**, *14*, 3185–3190.

[207] M.-H. Chiu, M.-Y. Li, W. Zhang, W.-T. Hsu, W.-H. Chang, M. Terrones, H. Terrones, L.-J. Li. *ACS Nano* **2014**, *8*, 9649–9656.

[208] Y. Liu, H. Fang, A. Rasmita, Y. Zhou, J. Li, T. Yu, Q. Xiong, N. Zheludev, J. Liu, W. Gao. *Sci. Adv.* **2019**, *5*, eaav4506.

[209] Y. Jiang, S. Chen, W. Zheng, B. Zheng, A. Pan. *Light Sci. Appl.* **2021**, *10*, 72.

[210] M. Baranowski, A. Surrente, L. Klopotowski, J. M. Urban, N. Zhang, D. K. Maude, K. Wiwatowski, S. Mackowski, Y. C. Kung, D. Dumcenco, A. Kis, P. Plochocka. *Nano Lett.* **2017**, *17*, 6360–6365.

[211] C. Struzzi, M. Scardamaglia, N. Reckinger, H. Sezen, M. Amati, L. Gregoratti, J.-F. Colomer, C. Ewels, R. Snyders, C. Bittencourt. *Phys. Chem. Chem. Phys.* **2017**, *19*, 31418–31428.

[212] S. S. Chou, M. De, J. Kim, S. Byun, C. Dykstra, J. Yu, J. Huang, V. P. Dravid. *J. Am. Chem. Soc.* **2013**, *135*, 4584–4587.

[213] C. Backes, N. C. Berner, X. Chen, P. Lafargue, P. LaPlace, M. Freeley, G. S. Duesberg, J. N. Coleman, A. R. McDonald. *Angew. Chem. Int. Ed.* **2015**, *54*, 2638–2642.

[214] S. Tongay, J. Zhou, C. Ataca, J. Liu, J. S. Kang, T. S. Matthews, L. You, J. Li, J. C. Grossman, J. Wu. *Nano Lett.* **2013**, *13*, 2831–2836.

[215] H. Nan, Z. Wang, W. Wang, Z. Liang, Y. Lu, Q. Chen, D. He, P. Tan, F. Miao, X. Wang, J. Wang, Z. Ni. *ACS Nano* **2014**, *8*, 5738–5745.

[216] P. K. Gogoi, Z. Hu, Q. Wang, A. Carvalho, D. Schmidt, X. Yin, Y.-H. Chang, L.-J. Li, C. H. Sow, A. H. C. Neto, M. B. H. Breese, A. Rusydi, A. T. S. Wee. *Phys. Rev. Lett.* **2017**, *119*, 077402.

[217] H. Ardekani, R. Younts, Y. Yu, L. Cao, K. Gundogdu. *ACS Appl. Mater. Interfaces* **2019**, *11*, 38240–38246.

[218] J. Hong, Z. Hu, M. Probert, L. Kun, D. Lv, X. Yang, L. Gu, N. Mao, Q. Feng, L. Xie, J. Zhang, D. Wu, Z. Zhang, C. Jin, W. Ji, X. Zhang, J. Yuan, Z. Zhang. *Nat. Commun.* **2015**, *6*, 6293.

[219] H. Li, Z. Yin, Q. He, H. Li, X. Huang, G. Lu, D. Fam, A. Tok, Q. Zhang, H. Zhang. *Small* **2012**, *8*, 63–67.

Acknowledgments

This thesis was prepared at Institut für Chemie und Biochemie, Freie Universität Berlin between October 2017 and January 2022 under the supervision of Professor Dr. Beate Paulus. I am grateful to many people who have helped me during this time.

First of all, I would like to express my deep and sincere gratitude to my esteemed supervisor Professor Dr. Beate Paulus for offering me the golden opportunity to conduct my Ph.D. research in her group. Her motivation, vision, endless energy and broad knowledge have deeply impressed me. I really appreciate the superb atmosphere and freedom for scientific research generously offered by her. Her warmly encouragement and endless support have greatly promoted my research.

I would also like to thank Dr. Elena Voloshina for her wiliness to be my second supervisor and her generous support and help throughout my Ph.D. study. I learned a lot from her.

I would like to acknowledge Thomas Grohmann, Gernot Füchsel, Christian Stemmle and Kai Töpfer for their help and harmonious working atmosphere as well as the fun in and outside the office.

My special thanks also goes to my correction team: Liangliang Zhang, Jennifer Anders, Jiajun Dai, Jingjing Shao. According to their suggestions, this thesis was polished and improved in both language and logicality.

I would like to thank Lukas Eugen Marsoner Steinkasserer for guiding me to fit into the group at the beginning of my Ph.D.

A huge thanks goes to all former and present co-workers in research group of Paulus. It is my great honor to work with these talented and motivated young researchers. These include Dirk Andrae, Chunmei Liu, Stefan Mattsson, Liangyin Kuo, Qian Zhang, Jianliang Low, Tilen Lindic, Jan Felix Witte, Frederik Bader and Lawrence Conrad.

I would like to take this opportunity to express my heartfelt gratitude to my parents and family for their continuous supports and encouragement.

Most of all, I thank my husband Liangliang Zhang for his company and love. It is you that led me out of the loneliness when I was lost in my mind.